

# Spectroscopic and theoretical studies of small molecules.

FERGUSON, A.M.

1986

*The author of this thesis retains the right to be identified as such on any occasion in which content from this thesis is referenced or re-used. The licence under which this thesis is distributed applies to the text and any original images only – re-use of any third-party content must still be cleared with the original copyright holder.*

SPECTROSCOPIC AND THEORETICAL STUDIES OF SMALL  
MOLECULES

ALLAN M FERGUSON

A thesis submitted for the  
Council for National Academic Awards  
degree of Doctor of Philosophy.

ROBERT GORDON'S INSTITUTE OF TECHNOLOGY

(Collaborating Establishment: Aberdeen University)

December 1986

## PREFACE

This thesis is a record of research carried out by the author in both the School of Chemistry, Robert Gordon's Institute of Technology and in the Department of Chemistry, Aberdeen University between October 1983 and December 1986. It has not previously been submitted for any degree and is believed to be wholly original except where due reference is made.

I am particularly indebted to my supervisory team - Drs. J. Harper and K. Tonge (R.G.I.T.), and Dr. J. L. Duncan (A.U.) for their excellent guidance and constant encouragement throughout.

I should like to thank R.G.I.T. Computer Services Unit staff for allocation of substantial computing time and space, which my research demanded.

I am grateful to Prof. D. C. McKean for use of facilities at A.U., to Dr. A. R. Morrisson for quality infrared spectra and to Dr. I. Torto for helpful advice.

I wish also to extend my appreciation to my fellow research colleagues at R.G.I.T. for encouragement and useful discussions.

I should like to thank the Science and Engineering Research Council for the provision of a research studentship.

Finally I wish to acknowledge the untiring support and encouragement of my parents and family during my education, and accordingly dedicate this thesis to them.

	ART		
	KEP		

## ABSTRACT

### SPECTROSCOPIC AND THEORETICAL STUDIES OF SMALL MOLECULES

Allan M Ferguson

This thesis is concerned with two contrasting molecules - ketene ( $\text{H}_2\text{CCO}$ ) and methylene chloride ( $\text{CH}_2\text{Cl}_2$ ). High resolution ( $\sim 0.05\text{cm}^{-1}$ ) infrared studies of ketene were carried out and complete analyses performed to the  $A_1$  species vibrations  $\nu_1 - \nu_4$ , allowing the determination of revised vibrational frequencies and rotational parameters. Perturbations found to be present in all bands were elucidated and identified with the aid of  $\text{H}_2\text{C}^{13}\text{CO}$ ,  $\text{H}_2^{13}\text{CCO}$  and  $\text{D}_2\text{CCO}$  isotopic species. Approximate analyses on these species also permitted the determination of revised  $\text{D}_2\text{CCO}$   $A_1$  vibrational frequencies and  $^{13}\text{C}$  frequency shifts. Preliminary analyses were also performed to the two  $B_1$  species vibrations,  $\nu_5$  and  $\nu_6$ , and two of the three  $B_2$  vibrations,  $\nu_7$  and  $\nu_8$  in order to determine precise  $^{13}\text{C}$  frequency shifts for use in force field calculations.

Subsequent empirical harmonic force field studies for ketene were carried out and 16 out of 19 force constants were determined. Owing to inaccuracies in a large number of the  $A_1$  vibrational frequencies and shifts arising through perturbations, the corresponding force constants were poorly

defined. Complementary and supplementary ab initio force field studies were also carried out. The well-defined empirical constants were found to be in excellent numerical agreement with their corresponding ab initio values. For the inadequately described empirical  $\text{CH}_2$  symmetric stretch interaction constants, the ab initio values were preferred, and were included in what is considered to be the best compromise force field for ketene, in the absence of accurate unperturbed data.

Empirical force field studies of methylene chloride suffered none of the set-backs encountered for ketene and thus a complete set of accurate force constants was determined. Complementary ab initio force field studies were carried out and found to be in good overall agreement with those of the empirical studies.

## CONTENTS

	<u>Page No.</u>
1. VIBRATION - ROTATION THEORY, HARMONIC FORCE FIELD AND AB INITIO FORCE FIELD	1
1.1 Vibration - Rotation Spectra of Asymmetric Top Molecules	2
1.1.1 Factorisation of Molecular Kinetic Energy	2
1.1.2 Vibration - Rotation Hamiltonian	3
1.1.3 Solutions to the Vibrational Hamiltonian	4
1.1.4 Rotational Hamiltonian and Eigenvalues	5
1.1.5 Vibrational and Rotational Selection Rules and Band Structure of Asymmetric Top Molecules	10
(a) Vibrational Selection Rules	10

	<u>Page</u> <u>No.</u>
(b) Rotational Selection Rules	10
(c) Band Structures	13
1.1.6 Perturbations	15
1.2 Empirical Harmonic Force Field	18
1.2.1 Vibrational Kinetic Energy	18
1.2.2 Vibrational Potential Energy	21
1.2.3 Secular Determinant for Vibrations	22
1.2.4 Selection of Internal Coordinates	23
1.2.5 Sources of Information	24
(a) Frequency Data	24
(b) Coriolis Coupling Constants	27
(c) Centrifugal Distortion Constants	27

1.2.6	Force Constant Calculations	27
	(a) Non Linearity	29
	(b) Singularity	29
	(c) Multiple Solutions	30
1.3	Ab Initio Force Field	31
1.3.1	Introduction	31
1.3.2	Ab Initio Molecular Orbital Methods	32
1.3.3	Orbital Representation	35
1.3.4	Selection of Theoretical Model and Basis Functions	38
1.3.5	Molecular Energy Differentiation	40
1.3.5.1	The Force Method	41
1.3.5.2	Evaluation of Force Constants	42

	<u>Page No.</u>
1.3.5.3 Theoretical Equilibrium Configuration	43
1.3.6 Selection of Reference Geometry	45
2. HIGH RESOLUTION INFRARED STUDIES OF KETENE	47
2.1 Introduction	47
2.2 Experimental Procedure	49
(a) Synthesis of ketene	49
(b) Spectra	50
2.3 Method of Analysis of Rotational Structure	50
(a) A-type	50
(b) B and C-type	52
2.4 Results and Discussion of Individual Band Analyses	53

(a) $\nu_1$ , CH <sub>2</sub> symmetric stretch, 3070cm <sup>-1</sup>	53
(b) $\nu_2$ , CCO asymmetric stretch, 2152cm <sup>-1</sup>	62
(c) $\nu_3$ , CH <sub>2</sub> deformation, 1387cm <sup>-1</sup>	68
(d) $\nu_4$ , CCO symmetric stretch, 1116cm <sup>-1</sup>	77
(e) $2\nu_5$ , CCO deformation overtone, 1189cm <sup>-1</sup>	85
(f) $2\nu_6$ , CH <sub>2</sub> wagging overtone, 1060cm <sup>-1</sup>	87
(g) $2\nu_8$ , CH <sub>2</sub> rocking overtone, 1952cm <sup>-1</sup>	90
(h) $\nu_7$ , CH <sub>2</sub> asymmetric stretch, 3165cm <sup>-1</sup>	92
(i) $\nu_8$ , CH <sub>2</sub> rocking, 978cm <sup>-1</sup>	96
(j) $\nu_5$ , CCO deformation, 587cm <sup>-1</sup> and $\nu_6$ wagging, 528cm <sup>-1</sup>	102

2.5	Conclusions	107
3.	AB INITIO AND EMPIRICAL FORCE FIELD STUDIES OF KETENE	113
3.1	Introduction	113
3.2	Symmetry Coordinates	115
3.3	Ab Initio Geometry and Force Field Studies of Ketene	119
3.3.1	Hardware and Software	119
3.3.2	Selection of the Basis Functions	120
3.3.3	Ab Initio Studies of the Equilibrium Geometry of Ketene	123
3.3.4	Ab Initio Force Field Studies of Ketene	129

	<u>Page</u> <u>No.</u>
3.4 Empirical Harmonic Force Field of Ketene	141
3.4.1 Experimental Data and their Assessment	141
(a) Vibration Frequencies	141
(b) Coriolis Interaction Constants	142
(c) Quartic Distortion Constants	144
3.4.2 Anharmonic Corrections	145
3.4.3 Uncertainties allowed in Data	147
3.4.4 Force Constant Calculations	148
3.4.5 Joint Empirical and Ab Initio Calculations	154
3.4.6 Effect of Molecular Structure on Force Constant Calculations	157

	<u>Page</u> <u>No.</u>
3.5 Scaled Ab Initio Force Constants	158
3.6 Spectroscopic Data For Isotopic Ketenes	164
(a) Frequency Data	164
(b) Quartic Distortion Constants	167
(c) Coriolis Constants	167
4. EMPIRICAL AND AB INITIO STUDIES OF METHYLENE CHLORIDE	171
4.1 Introduction	171
4.2 Symmetry Coordinates	172
4.3 Empirical Force Field Studies	174
4.3.1 Assimilated Experimental Data	174
4.3.2 Anharmonicity Corrections and allowed Uncertainties	175

4.3.3	Force Constant Calculations	176
4.4	Ab Initio Studies of Methylene Chloride	180
4.4.1	Basis Sets	181
4.4.2	Equilibrium Geometry Predictions for Methylene Chloride	183
4.4.3	Ab Initio Force Field Studies of Methylene Chloride	184
4.4.4	Scaled Ab Initio Force Field	187
4.5	Calculated Spectroscopic Parameters	190
4.6	Joint Empirical/Ab Initio GHFF for Methylene Chloride	197
	REFERENCES	199

## CHAPTER 1

### VIBRATION - ROTATION THEORY, HARMONIC FORCE FIELD AND AB INITIO FORCE FIELD

The theoretical background to this thesis will be outlined in this first chapter. It is divided into three sections each dealing with distinct topics.

In the first section, a concise description of relevant vibration - rotation theory is given, in which quantitative expressions for molecular vibrational and rotational energies are introduced. These are then used to describe the observed structure of high resolution infrared bands of gas phase asymmetric top molecules.

The second section gives a brief account of the theoretical background to harmonic force constant calculations, in which expressions relating vibrational energies to force constants are derived. Various aspects relevant to the application of the harmonic force constant calculations are also considered.

In the final introductory section, an ab initio quantum

mechanical approach to obtaining molecular force constants is described. The section begins with a concise summary of relevant underlying quantum mechanical theory and then details various aspects relevant to the determination of ab initio force constants.

More detailed accounts of these topics can be found in several texts and review articles (1-12).

## 1.1 VIBRATION-ROTATION SPECTRA OF ASYMMETRIC TOP MOLECULES

### 1.1.1 FACTORISATION OF MOLECULAR KINETIC ENERGY

An understanding of molecular motions can be developed by regarding a molecule as consisting of a number of atomic nuclei, held together in a well defined configuration, by a potential generated by its constituent electrons. In terms of this model, the molecular kinetic energy  $T$ , can be expressed as the sum of the kinetic energies of constituent atoms, which factorises as follows:-

$$T = T(\text{translation}) + T(\text{rotation}) + T(\text{vibration}) \\ + T(\text{vibration-rotation}) \quad 1.1$$

It can be seen from equation 1.1 that whilst the translational energy can be considered separately, the vibrational and rotational terms are not completely

separable. This is a consequence of the last term  $T(\text{vibration-rotation})$ , which arises from the interaction of vibrational and rotational motions.

### 1.1.2 VIBRATION - ROTATION HAMILTONIAN

Vibrational and rotational energies are calculable in terms of quantum mechanics, where the energy levels are the eigenvalues of the appropriate Schrödinger equation:

$$\hat{H}_{V,R}\Psi = E_{V,R}\Psi \quad 1.2$$

The  $\hat{H}_{V,R}$  term of equation 1.2 is the quantum mechanical Hamiltonian of the system and can be derived from the classical vibrational and rotational kinetic energies (13,14) of equation 1.1, which are expressed in terms of linear and angular momenta. In addition, the vibration - rotation Hamiltonian also contains the potential energy. By defining a set of internal coordinates called normal coordinates to describe vibrational motion, the Hamiltonian potential and kinetic terms are diagonalised. Normal coordinates define a set of mutually independent normal vibrations, in each of which the nuclei oscillate in simple harmonic motion about their equilibrium positions.

After simplification (15), through introduction of a number of approximations,  $\hat{H}_{V,R}$  is given in its simplest form as the sum of independent vibrational and rotational Hamiltonians and can be solved in terms of the Schrödinger

equation. The solutions to these will now be discussed separately.

### 1.1.3 SOLUTIONS TO THE VIBRATIONAL HAMILTONIAN

Assuming that the vibrational motion can be regarded as a simple harmonic motion, then the vibrational potential energy can be expressed as

$$V(Q_r) = \frac{1}{2} \lambda_r Q_r^2 \quad 1.3$$

where  $\lambda_r$  is the force constant associated with normal coordinate  $Q_r$ . The eigenvalues for a harmonic oscillator are given by

$$E_{v_r}/hc = \omega_r (v_r + 1/2) \quad (v_r = 0, 1, 2, \dots) \quad 1.4$$

where  $v_r$  is the vibrational quantum number and  $\omega_r$  is the frequency of vibration, expressed in terms of wavenumbers ( $\text{cm}^{-1}$ ) and is defined as

$$\omega_r = \frac{1}{2\pi c} (\lambda_r)^{1/2} \quad 1.5$$

In practice however, this model is too approximate since vibrations of nuclei are never strictly harmonic - the stretching of the oscillator is not perfectly elastic and so the vibrations are anharmonic. Harmonic vibrational energies are corrected in terms of perturbation theory

(16-18), which gives the following energy expression:

$$E_v/hc = \sum_r (v_r + 1/2) \omega_r + \sum_r \sum_{s \geq r} (v_r + 1/2)(v_s + 1/2) x_{rs} - \dots \quad 1.6$$

where the  $x_{rs}$  are anharmonicity constants.

#### 1.1.4 ROTATIONAL HAMILTONIAN AND EIGENVALUES

In dealing with the solutions to the rotational Hamiltonian of a molecular system, it is advantageous to classify the molecule in terms of moments of inertia. These are defined with respect to the three "principal" inertial axes of the molecule, x, y and z.

The current studies are concerned with vibration - rotation spectra of asymmetric top molecules, for which  $I_x \neq I_y \neq I_z$ . Clearly, the extent of asymmetry is dependent on the actual values of  $I_x$ ,  $I_y$  and  $I_z$ . For "slightly asymmetric" molecules, such as ketene ( $H_2CCO$ ), the arrangement of rotational energy levels would not be expected to differ too much from that of a symmetric rotor. It is therefore instructive to commence discussion of rotational models by firstly considering the symmetric rotor model, since the asymmetric rotor Hamiltonian can be organised to take advantage of any near-symmetric top character present in the molecule. This facilitates the determination of quantitative expressions for the rotational levels of asymmetric rotors.

In the case of a symmetric rotor, where  $I_x = I_y \neq I_z$ , the resulting rotational energies or eigenvalues are given (in  $\text{cm}^{-1}$  units) by

$$E_{(J,k)} = \frac{h}{8\pi^2 c} \left\{ \frac{1}{I_x} J(J+1) + \left[ \frac{1}{I_z} - \frac{1}{I_x} \right] k^2 \right\} \quad 1.7$$

where  $J$  is the total angular momentum quantum number which can have values of 0, 1, 2, 3, ... and  $k$  is a quantum number which represents the projection of the total angular momentum on the internal  $z$  axis i.e. it governs the axial angular momentum. Its value is such that  $-J \leq k \leq J$ .

In spectroscopy, it is more usual to label the inertial axes as  $a$ ,  $b$  and  $c$  such that  $I_a \leq I_b \leq I_c$  (19). In terms of this convention, the following rotational constants are defined:

$$A = h/8\pi^2 c I_a \quad B = h/8\pi^2 c I_b \quad C = h/8\pi^2 c I_c$$

This gives rise to two possibilities for symmetric rotors. For a prolate symmetric rotor, where  $I_a < I_b = I_c$ , equation 1.7 becomes

$$E_{(J,K)} = BJ(J+1) + (A - B)K^2 \quad 1.8$$

For an oblate symmetric rotor where  $I_a = I_b < I_c$ , the rotational energies are described by

$$E_{(J,K)} = BJ(J+1) + (C - B)K^2 \quad 1.9$$

In expressions 1.8 and 1.9,  $K$  is the modulus of  $k$  of equation 1.7. This implies that energy levels with  $K > 0$  are doubly degenerate.

For asymmetric rotors, unlike symmetric rotors, the component of the total angular momentum is not rigorously quantised; therefore, no definitive quantum number other than  $J$  is available to characterise the rotational energy states, and no simple analytical expression, such as 1.7, is available for the energy levels.

This problem can be overcome however, by rearranging the asymmetric rotor Hamiltonian to be expressed in terms of a symmetric rotor basis and an asymmetry parameter which is defined in terms of the molecular rotational constants. The Wang asymmetry parameter (20), can assume a value between 0, which represents the prolate symmetric rotor limit, and -1 for the oblate symmetric rotor limit, in the  $I^R$  representation (19). By using symmetric (+) and antisymmetric (-) linear combinations of degenerate symmetric top functions (the Wang basis), the rotational Hamiltonian factorises into four symmetry blocks for each value of  $J$  ( $J \geq 2$ ), giving four sets of energy levels on diagonalisation. These are labelled  $E^+$ ,  $E^-$ ,  $O^+$  and  $O^-$ , where  $E$  and  $O$  refer to the parity of  $K$ , and + and - refer to the Wang basis functions.

The arrangement of the resulting asymmetric rotor rotational energy levels is such that for a given value of  $J$ , high  $K$  levels approximate more and more closely to the

limiting symmetric rotor approximation, and  $K^+$  and  $K^-$  levels for the same value of  $K$  become degenerate.

The asymmetric rotor energy levels are usually designated by  $J_{K_a K_c}$ , where  $K_a$  and  $K_c$  apply to the limiting prolate and oblate symmetric rotors respectively. Figure 1.1 illustrates the correlation for some of the lower levels of an asymmetric rotor, where it can be seen that for given values of  $J$ , energy levels increase as  $K_a$  goes from 0 to  $J$  and  $K_c$  goes from  $J$  to 0.

The above rotational energy expressions for symmetric and asymmetric rotors are derived in terms of a rigid rotor. These are not, however sufficient to describe adequately high resolution vibration - rotation spectra. In real molecules, the effect of rotation on the molecule is to cause small changes in the structure parameters from their equilibrium values as a result of centrifugal forces on the atoms. In an analogous fashion to anharmonicity corrections for the harmonic oscillator, this can be corrected for by application of perturbation theory (13,21). For asymmetric top molecules, the effect can be expressed, in the first approximation by five quartic centrifugal distortion coefficients  $\Delta_J$ ,  $\Delta_{JK}$ ,  $\Delta_K$ ,  $\delta_J$  and  $\delta_K$  (22,23), which can be introduced into the diagonalisation procedure outlined above.

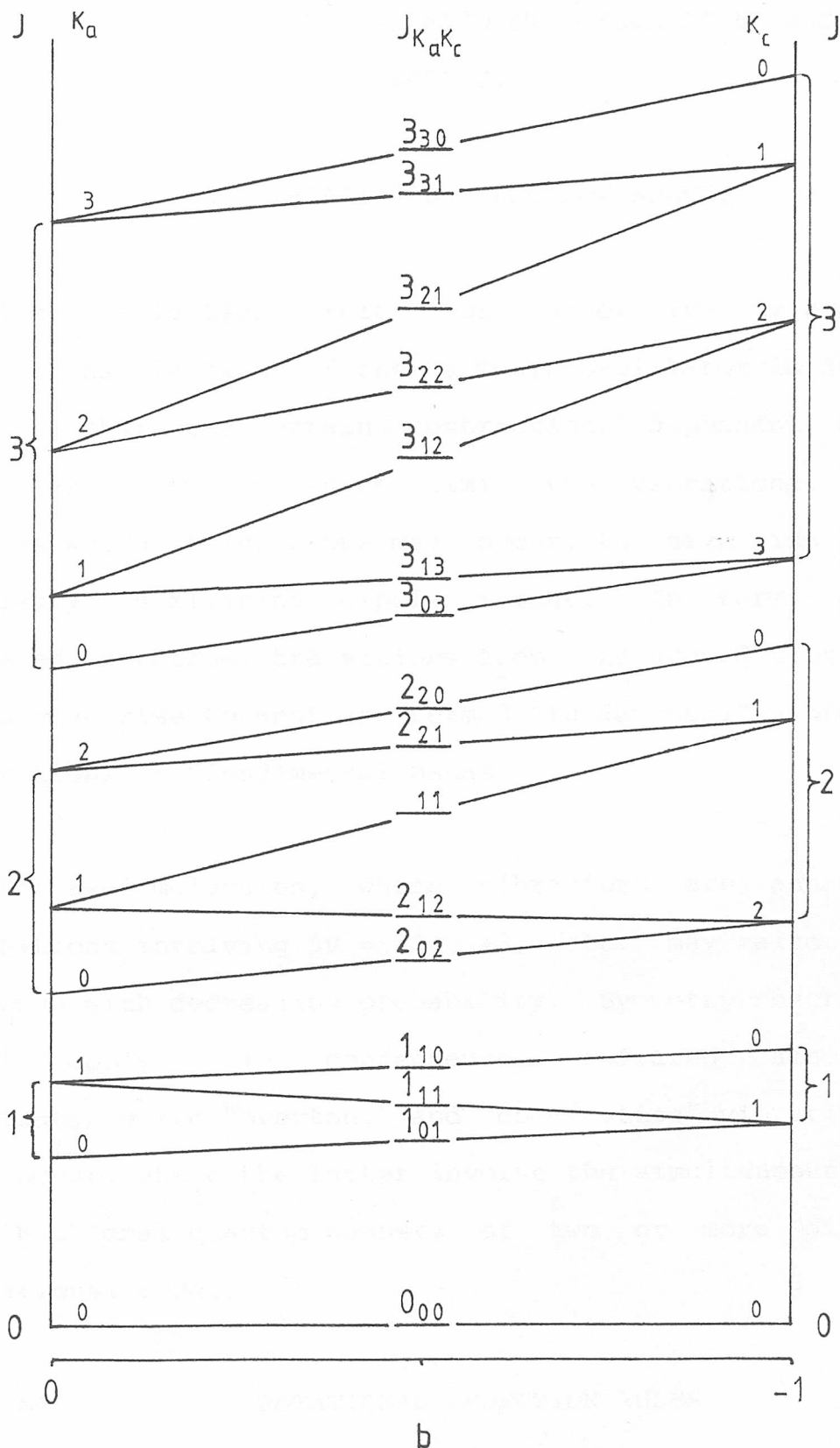


Figure 1.1. Correlation diagram illustrating the energy level pattern for asymmetric rotors.  $b$  is the Wang asymmetry parameter in the  $I^R$  representation.

1.1.5 VIBRATIONAL AND ROTATIONAL SELECTION  
RULES AND BAND STRUCTURE OF ASYMMETRIC  
TOP MOLECULES.

(a) VIBRATIONAL SELECTION RULES.

The selection rule for absorptive vibrational transitions, in terms of the harmonic oscillator is  $\Delta v = +1$ . However, there are certain restrictions dependent on the molecular symmetry which limit the vibrational states between which transitions may occur, to give rise to the necessary oscillating dipole moment. In terms of the infrared spectrum, transitions from the ground vibrational state give rise to what are termed "fundamental" vibrational absorptions or "fundamental bands".

For real molecules, where vibrations are anharmonic, transitions involving  $\Delta v = +2, +3, \text{ etc.}$  may also occur, although with decreasing probability. Symmetry restrictions still apply. In consequence, infrared absorptions attributable to "overtone" and "combination" vibrations can also occur, where the latter involve the simultaneous change in vibrational quantum numbers of two or more different vibrational modes.

(b) ROTATIONAL SELECTION RULES

For fundamentals, the rotational selection rules governing the associated rotational transitions depend on

the nature of the vibration - in particular, the direction of the oscillating dipole moment. If only asymmetric top molecules of sufficient symmetry are considered, then infrared vibration - rotation bands are classified as type-A, type-B or type-C, corresponding to the direction of the oscillating dipole being parallel to the a, b or c inertial axis respectively.

The associated rotational selection rules are summarised in table 1.1. The way in which the selection rules of table 1.1 dictate the associated asymmetry split  $K_a^+$  and  $K_a^-$  transitions for the three band types is schematically represented in figure 1.2. This diagram, in conjunction with figure 1.1 is of assistance in understanding the band structures and in the assignment of transitions to the observed spectrum.

---

Table 1.1. Rotational selection rules for the most intense transitions in the infrared bands of asymmetric top molecules.

---

Ground rotational state		J	$K_a$	$K_c$
Type-A	$K_a = 0$	$\pm 1$	0	$\pm 1$
	$K_a \neq 0$	$0, \pm 1$	0	$\pm 1$
Type-B	$K_a > 0$	$0, \pm 1$	$\pm 1$	$\pm 1$
Type-C	$K_c = 0$	$\pm 1$	$\pm 1$	0
	$K_c \neq 0$	$0, \pm 1$	$\pm 1$	0

---

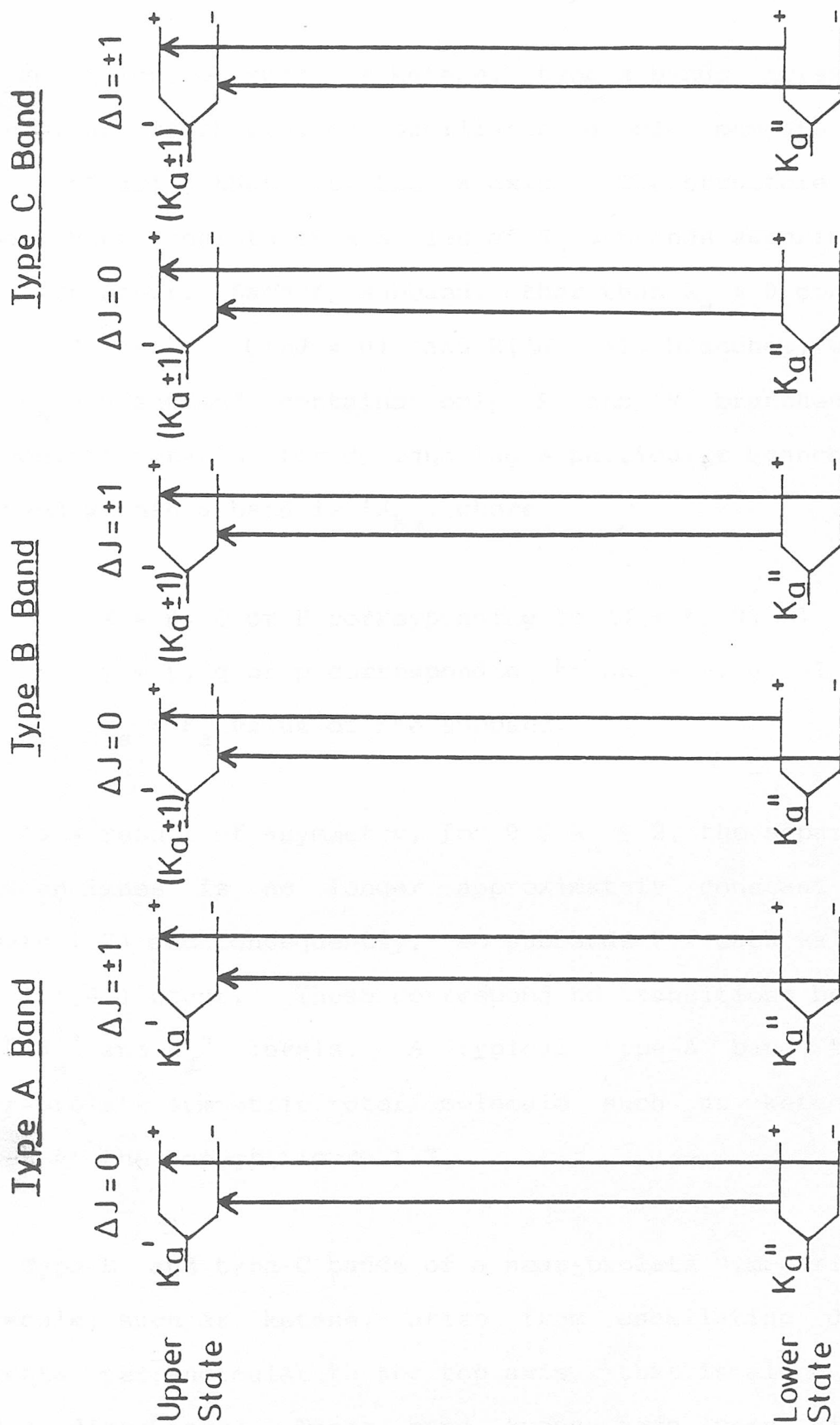


Figure 1.2. Transitions involving the asymmetry split rotational levels for type-A, -B and -C bands.

For molecules such as ketene, type-A bands arise from vibrations which produce oscillating dipole moments along the 'top' axis, that is, the a axis. The structure of a type-A band consists of a series of  $K_a$  subbands superimposed on each other. Each  $K_a$  subband, other than  $K_a = 0$  consists of  $P(\Delta J = -1)$ ,  $Q(\Delta J = 0)$  and  $R(\Delta J = +1)$  branches, whilst the  $K_a = 0$  subband contains only P and R branches. A convenient notation for designating a particular branch of a subband within a band is  ${}^Y X_{K_a}$ , where

$X = R, Q$  or  $P$  corresponding to  $\Delta J = 1, 0, -1$

$y = r, q$  or  $p$  corresponding to  $\Delta K_a = 1, 0, -1$

$K_a = K_a$  value of the subband.

As a result of asymmetry, for  $0 \leq K_a \leq 2$ , the separation between lines is no longer approximately constant (see figure 1.2) and consequently, two subbands for each value of  $K_a$  ( $> 0$ ) occur. These correspond to transitions between both  $K_a^+$  and  $K_a^-$  levels. A typical type-A band for a near-prolate symmetric rotor molecule such as ketene is given at the top of figure 1.3.

Type-B and type-C bands of a near-prolate symmetric top molecule, such as ketene, arise from oscillating dipole moments perpendicular to the top axis, that is along the b and c directions. These band types have very similar structures for  $K_a > 2$ , but differ in the region of the band

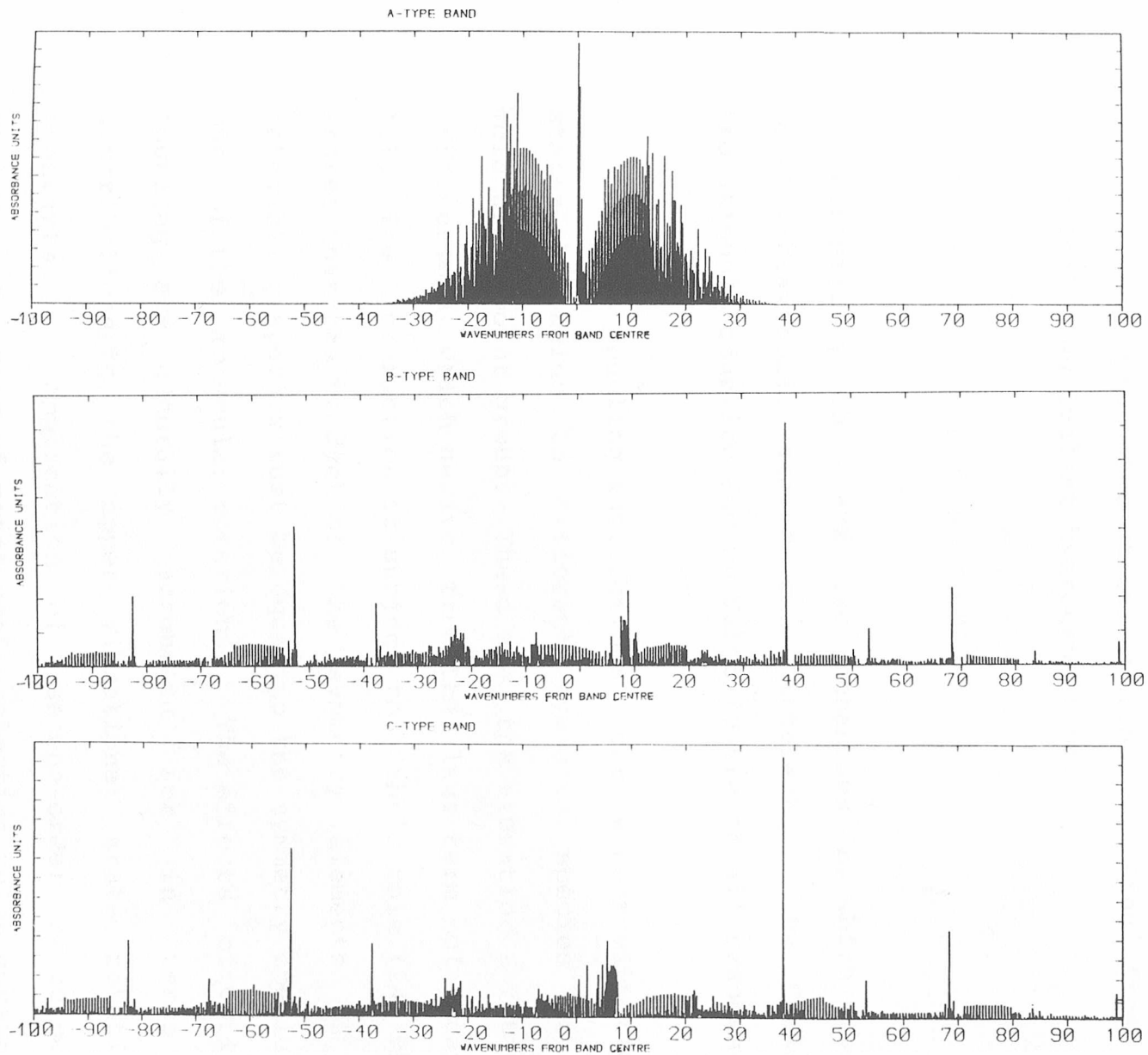


Figure 1.3. Type-A, -B and -C bands for a ketene-like near prolate symmetric top molecule ( $\Delta A = -0.02$ ,  $\Delta B = -0.0002$ ,  $\Delta C = -0.0003\text{cm}^{-1}$ ).

centre - the  ${}^rQ_0$  and  ${}^pQ_1$  branches characteristically degrade away from and towards the band centre in type-B and type-C bands respectively. Type-B and type-C bands of the type found in ketene may also be found in figure 1.3, where it can be seen that even  $K_a$  subbands are at one third of the intensity of odd  $K_a$  subbands. This is attributable to nuclear spin statistical weights arising from the symmetrically equivalent hydrogen atoms.

#### 1.1.6 PERTURBATIONS

Essentially, there are two mechanisms by which two or more vibrational states can interact - by Coriolis (rotational) coupling and by Fermi (vibrational) resonance.

Coriolis coupling interactions occur between vibrational states belonging to different symmetry species of the molecular point group. These are the vibration - rotation interactions which derive from the last term of equation 1.1. The interaction is subject to Jahn's rule (24) which states that the product of the symmetry elements of the interacting species must be equal to the symmetry species of one of the molecular rotations. The effects of Coriolis coupling are generally accounted for in terms of contributions to the upper vibrational state rotational constants by application of second-order perturbation theory. A number of rotational selection rules govern the possible interactions. These are given in table 1.2 together with the contributions to  $\Delta X$ , which is defined as

$(X' - X'')$ , where  $X = A, B$  or  $C$  rotational constants and ' and '' represent the upper and ground vibrational states respectively.

Differences in the relevant energy level separations  $\Delta$  can lead to significant variation in the values of  $\Delta X$  throughout a band. When the interacting levels are sufficiently close, the interactions must be treated explicitly in order to fit the observed effects.

In addition to these selection rules of table 1.2, weak asymmetry allowed Coriolis interactions are also possible between levels differing by a further 2 units in  $K_a$  (25) and would be expected to give rise to localised perturbations, affecting a limited number of transitions only.

Table 1.2. Coriolis selection rules and second order resonance contributions to the rotational constants of asymmetric top molecules.

Rotn. Axis	$\Delta J$	$\Delta K_a$	$\Delta K_c$	Interacting levels	Second Order Resonance Contribution to $\Delta X$
$R_a = R_z$	0	0	$\pm 1$	$E^+ \leftrightarrow E^-$ $O^+ \leftrightarrow O^-$	$\Delta A = 4(A\zeta^a)^2/\Delta$
$R_b = R_x$	0	$\pm 1$	1	$E^+ \leftrightarrow O^+$ $E^- \leftrightarrow O^-$	$\Delta B = 4(B\zeta^b)^2/\Delta$
$R_c = R_y$	0	$\pm 1$	0	$E^+ \leftrightarrow O^-$ $E^- \leftrightarrow O^+$	$\Delta C = 4(C\zeta^c)^2/\Delta$

Anharmonic or Fermi resonance interactions occur between vibrational states of the same symmetry species, in which interactions occur between rotational levels with the same value of  $J_{KaKc}$  (i.e.  $E^+ \leftrightarrow E^+$ ,  $E^- \leftrightarrow E^-$ ,  $O^+ \leftrightarrow O^+$  and  $O^- \leftrightarrow O^-$ ). These arise through the existence of cubic and higher (anharmonic) terms in the expansion of the molecular potential energy in terms of the normal coordinates, in addition to the purely harmonic terms of equation 1.3.

Where only two levels are in Fermi resonance, the perturbed energies of the states are given by

$$E_{\pm} = 1/2 (E_m^{\circ} + E_n^{\circ}) \pm 1/2 (d_o^2 + 4W_{mn}^2)^{1/2} \quad 1.10$$

where  $E_m^{\circ}$  and  $E_n^{\circ}$  are the unperturbed energies;

$$d_o = E_m^{\circ} - E_n^{\circ}$$

and  $W_{mn}$  is the Fermi resonance interaction parameter.

Interactions involving more than two interacting levels are more complex and require full matrix diagonalisation.

In terms of the rotational constants of the interacting vibrations, the perturbation is manifested as a degree of mixing of the unperturbed constants. In the event of exact degeneracy of the two states, a fifty - fifty mixture occurs.

From section 1.1.3, it can be seen that molecular normal vibrations and harmonic vibration frequencies are described in terms of a set of harmonic force constants or a force field. The determination of these force constants will now be considered.

## 1.2.1

## VIBRATIONAL KINETIC ENERGY

It has previously been stated in section 1.1.1 that the total molecular kinetic energy  $T$ , can be expressed as a sum of the kinetic energies of  $N$  constituent atoms. This premiss also forms the basis for the determination of the empirical harmonic force field.

The  $N$  atomic kinetic energies can be defined in terms of atomic masses and the time derivatives of the  $3N$  Cartesian displacement coordinates. According to classical mechanics, this can be expressed as a matrix product:

$$2T = \dot{\mathbf{X}}^+ \mathbf{M} \dot{\mathbf{X}} \quad 1.11$$

$\dot{\mathbf{X}}$  is a single column matrix whose elements are the time derivatives of the  $3N$  displacement coordinates and  $\mathbf{M}$  is a diagonal matrix of the nuclear masses, each of which appear three times.

As established in section 1.1, for the treatment of

vibrations, it is advantageous to introduce a set of internal coordinates to describe the relevant motions of the nuclei, defined such that they are independent of the translational and rotational motions. These are defined in terms of the Cartesian displacements  $X$  of the nuclei and the overall molecular geometry, such that,

$$S = BX \tag{1.12}$$

where  $B_{ir}^x = (\delta S_i / \delta x_r)_{XS, \dots}$  and is readily calculable.

Clearly, for non-linear molecules,  $B$  will have  $3N-6$  rows and  $3N$  columns and by attaching a further 6 rows, a square matrix may be constructed. The attached  $6 \times 3N$  matrix designated  $B_o$  contains six orthogonal coordinates which relate to the translational and rotational motions and are usually referred to as "external" coordinates. Hence equation 1.12 becomes:-

$$\begin{bmatrix} S \\ \hline S_o \end{bmatrix} = \begin{bmatrix} B \\ \hline B_o \end{bmatrix} \begin{bmatrix} X \end{bmatrix} \tag{1.13}$$

Since the matrix partitioned into  $B$  and  $B_o$  is square then it will, in general have an inverse consisting of  $A$  and  $A_o$  for which the following must be true:-

$$\begin{bmatrix} X \end{bmatrix} = \begin{bmatrix} A \\ \hline A_o \end{bmatrix} \begin{bmatrix} S \\ \hline S_o \end{bmatrix} \tag{1.14}$$

Hence X can be substituted for in equation 1.11 to give

$$2T = \dot{S}^+ A^+ M A \dot{S} + \dot{S}^+ A^+ M A \underset{O}{\dot{S}}_O + \dot{S}^+ A^+ M A \dot{S} + \dot{S}^+ A^+ M A \underset{O}{\dot{S}}_O \quad 1.15$$

Of these four terms, the second and third are zero, the first relates to internal molecular vibration, and the last to the molecular translational and rotational motions. Once the molecular axis system is associated with the translating - rotating molecule, such that the Eckart conditions (26) are obeyed, the purely vibrational kinetic energy is given by the first term of 1.15,

$$2T = \dot{S}^+ A^+ M A \dot{S} = \dot{S}^+ G^{-1} \dot{S} \quad 1.16$$

where  $G^{-1}$  is the (symmetric) kinetic energy matrix in terms of the defined coordinates S. This expression assumes that the vibrations are harmonic.

The purely vibrational kinetic energy defined in the above equations involves evaluation of the A matrix, which is difficult. The matrix G however, is easy to calculate, being given by

$$G = B M^{-1} B^+ \quad 1.17$$

where B is the matrix inverse to A, and is defined by 1.12. (Being rectangular, neither A nor B can be inverted directly.) It is this G matrix which is required for the

force constant calculations.

### 1.2.2 VIBRATIONAL POTENTIAL ENERGY

The total potential energy of a molecule is a function of the internal coordinates only and is thus dependent on vibrational motions only. If the molecule is in its equilibrium configuration, then the total potential energy  $V$  is defined as

$$\begin{aligned}
 V = & \frac{1}{2}(\delta^2 V / \delta S_1^2)_0 \cdot S_1^2 + \frac{1}{2}(\delta^2 V / \delta S_2^2)_0 \cdot S_2^2 + \dots \\
 & + (\delta^2 V / \delta S_1 \delta S_2)_0 \cdot S_1 S_2 + (\delta^2 V / \delta S_2 \delta S_3)_0 \cdot S_2 S_3 + \dots
 \end{aligned}
 \tag{1.19}$$

in which the quadratic force constants are defined as

$$\begin{aligned}
 F_{11} &= (\delta^2 V / \delta S_1^2)_0, & F_{22} &= (\delta^2 V / \delta S_2^2)_0, \text{ etc.} \\
 \text{and} & & & \\
 F_{12} &= (\delta^2 V / \delta S_1 \delta S_2)_0, & F_{23} &= (\delta^2 V / \delta S_2 \delta S_3)_0, \text{ etc.}
 \end{aligned}
 \tag{1.20}$$

The vibrational potential energy equation 1.19 can be expressed simply in terms of the force constant matrix  $F$ , and the internal coordinate matrix  $S$  in an analogous fashion to that for the kinetic energy:

$$2V = S^+ F S \tag{1.21}$$

The classical equations of motion can be expressed in terms of internal coordinates and have the form

$$(\delta V / \delta S_i) + d/dt.(\delta T / \delta \dot{S}_i) = 0 \quad 1.22$$

Expansion of equations 1.16 and 1.21 for kinetic and potential energies respectively followed by insertion into equation 1.22 gives rise to the following expression for non-linear molecules,

$$\sum_{i \geq j=1}^{3N-6} (F_{ij}) S_j + \sum_{i \geq j=1}^{3N-6} (G_{ij}^{-1}) \ddot{S}_j = 0 \quad 1.23$$

where  $F_{ij}$  and  $G_{ij}$  represent elements of the matrices,  $F$  and  $G$ . In solving the classical equations for non-linear molecules, internal coordinates of the following form are sought

$$S_i = A_i \cdot \cos(\lambda^{1/2} t + e) \quad 1.24$$

where  $A_i$  is the amplitude of vibration,  $e$  is the phase angle and  $\lambda = 4\pi^2 c^2 \omega^2$ , in which  $\omega$  is the harmonic frequency (in  $\text{cm}^{-1}$ ) of a normal vibration. This form of solution requires that

$$\ddot{S}_i = -\lambda S_i \quad 1.25$$

Substituting for  $\ddot{S}_i$ , then for  $S_i$  in equation 1.23 followed by division by  $\cos(\lambda^{1/2} t + e)$  gives a series of amplitude equations:

$$\sum_{i \leq j=1}^{3N-6} (F_{ij} - G_{ij}^{-1}) A_j = 0 \quad 1.26$$

These amplitude equations simultaneously hold if the determinant of the coefficients is equal to zero. This can be expressed briefly in terms of a secular equation:

$$|F - \lambda G^{-1}| = 0 \quad 1.27$$

Equation 1.27 is usually converted into two other, entirely equivalent forms, which are more convenient. This is done by either pre- or post-multiplying by the G matrix to give

$$|GF - \lambda E| = 0 \quad 1.28$$

and

$$|FG - \lambda E| = 0 \quad 1.29$$

where E is the unit matrix. Solutions of the above determinantal equation allows the calculation of force constants from a knowledge of the normal vibrational frequencies, atomic masses and geometrical parameters. Collectively, these force constants are referred to as a force field, and when obtained in this fashion may be designated as an empirical harmonic force field.

#### 1.2.4 SELECTION OF INTERNAL COORDINATES

An important step towards the determination of the empirical harmonic force field is the selection of the

internal coordinates. It is customary to define these as linear combinations of valence coordinates involving bond stretching, angle deformation and torsion according to the symmetry properties of the molecule. Where possible, they are chosen to approximate to the expected normal coordinates of the molecule. These steps ensure the factorisation of the secular determinant into symmetry blocks with dominant diagonal valence force constants.

Care must be taken in the definitions whenever the interbond angles around an atom exceed the number of independent deformations, as redundancy will occur. This leads to indeterminacies in the associated valence force constants. In many cases, the problem of redundancies can be avoided mathematically by defining coordinates that avoid the redundancy. The indeterminacies remain, however.

#### 1.2.5 SOURCES OF INFORMATION

##### (a) Frequency data

Frequency data constitute the most abundant source of information available for force field determination through equations 1.28 and 1.29.

For a molecule which has  $n$  normal modes of vibration, there are  $n(n + 1)/2$  independent force constants. Hence,  $n$  frequency data for a single isotopic species of a molecule are insufficient to determine the full valence force field.

The number of frequency data may be increased by use of frequency data from isotopically substituted molecules. The usual H, D data are generally not of great discriminatory value in the calculation. Chalmers and McKean (27) have demonstrated that the uncertainty in a small frequency shift, accurately measured and corrected for anharmonicity (see below), is very much smaller than the cumulative uncertainties in the two independently treated frequencies, and can be of great value in the calculation.

The force field of a molecule may not, however, be determinable from frequency data alone. This is because often the frequencies are almost insensitive to certain force constants, but is aggravated by other factors.

Firstly, force field calculations are performed in terms of the harmonic oscillator approximation, whilst vibrational frequencies are anharmonic. Hence corrections have to be made. For most polyatomic molecules, only approximate corrections for anharmonicity can be made. These are usually based on the equations of Dennison's rule for diatomic molecules:

$$\omega_i = \nu_i / (1 - x_i) \quad 1.30$$

and

$$x_i^* = x_i \nu_i^* / \nu_i \quad 1.31$$

where  $\omega_i$  is the harmonic frequency,

$\nu_i$  is the anharmonic frequency,

$x_i$  is the anharmonicity constant and

\* refers to isotopically substituted species.

Secondly, many observed vibrational frequencies are appreciably affected by Fermi resonance interactions which should be corrected for. However, this is often not possible. Thus reduced reliability is placed on such data by effecting an attendant increase in the associated vibrational uncertainties.

Thirdly, for force field calculations, gas-phase data should ideally be used, where the molecules are considered to be mutually non-interacting. Condensation to the liquid or crystal phase may cause quite large shifts in vibrational frequency, though these are less severe for small frequency shifts. Data accumulated from different phases, if used, usually leads to reduced sensitivity.

In addition to vibrational frequencies, other parameters, particularly centrifugal distortion constants and Coriolis coupling constants can be determined from infrared and microwave studies. The former depend on the compliance (inverse force) constants (21), whilst the latter depend on the relative atomic displacements in the vibrations concerned (18), hence on the precise forms of the normal vibrations.

(b) Coriolis Coupling Constants

Approximate Coriolis coupling constants are obtained by dividing experimentally determined values of  $(X\zeta_{r,s}^X)$  by the rotational constant  $X$  ( $X = A, B, \text{ or } C$ ). However, precise evaluation of the Coriolis coupling constants is difficult since the vibrational dependence of  $(X\zeta_{r,s}^X)$  is not a readily observed quantity (18). In addition, for strict comparison with calculated force constant values, it is the hypothetical equilibrium constants which are required. Nevertheless, experimentally determined constants are still of considerable assistance in the force field determination, particularly in calculating interaction force constants and in discriminating between alternative mathematical solutions (see section 1.2.6).

(c) Centrifugal Distortion Constants

Infrared and microwave analyses allow the determination of ground state centrifugal distortion constants. Again, in order to be compatible with the force field calculation, these constants should be equilibrium values. However, the differences are generally small, although these may lead to problems.

1.2.6 FORCE CONSTANT CALCULATIONS

Most methods are based on an iterative computational procedure. Initially, this involves inputting the atomic

internal valence displacement coordinates, usually represented as symmetry coordinates, where the vibrations are classified according to their symmetry. Also input are the atomic masses and their cartesian coordinates, the latter being calculated from a predetermined molecular geometry. In terms of equations 1.12 and 1.17, these quantities permit the determination of the G matrix and moments of inertia for any isotopic species, the latter being necessary for calculation of centrifugal distortion constants.

Next, for each isotope, the atomic masses and complete set of frequencies are input. Coriolis coupling constants and centrifugal distortion constants are also included when available. Individual frequencies, Coriolis constants and distortion constants have associated uncertainties which are also input. From these, relative weightings of the data can be calculated.

Values for the observed data ( $\omega$ 's,  $\Delta\omega$ 's,  $\zeta$ 's and distortion constants) are then calculated from a set of trial force constants, which are often chosen to be those determined from earlier work.

The associated Jacobian matrix J, which consists of the following terms

$$(\delta\omega/\delta F), (\delta[\Delta\omega]/\delta F), (\delta\zeta/\delta F) \text{ and } (\delta D/\delta F),$$

is also calculated for the initial estimate force constants. These are used to calculate the first order

corrections to the trial force constants to minimise the difference between observed and calculated data according to the following expression

$$\delta F = (J^+ W J)^{-1} J^+ W e \quad 1.32$$

where  $W$  is the weighting matrix and  $e$  is the observed minus calculated error vector. This process is repeated using the revised set of force constants until the correction,  $\delta F$  becomes sufficiently small.

Several mathematical problems may arise using this procedure.

(a) Non linearity.

This can occur if the initial force matrix estimate is a poor one. It can cause the refinement to oscillate wildly and can even result in divergence instead of convergence. The most common solution to the problem is to damp the corrections to the force constants by a predetermined factor.

(b) Singularity.

If the matrix  $(J^+ W J)$  is nearly singular, large rounding errors may result from taking its inverse, causing large

errors in the calculated correction  $\delta F$ . This problem may occur when insufficient experimental data are available to define the force constants. Apart, obviously, from introducing more experimental data into the refinement, the problem can also be solved by constraining those force constants which are least sensitive to the data to fixed values.

(c) Multiple solutions.

The possibility that more than one solution to the force field can satisfactorily reproduce all the available data has been discussed in detail by McKean and Duncan (28). Many of the solutions may, however, be physically unreasonable and can be immediately discounted. Those which cannot be overlooked at this stage may only be distinguishable by introduction of additional experimental data. Distortion constants and Coriolis constants have been demonstrated to discriminate between alternative force field solutions in most cases.

For the purpose of discussion in this section, vibrations of a molecule can be regarded as taking place on a multidimensional potential surface. When displacements around a reference geometry are small, the potential energy can be expanded as a power series. The coefficients arising from the expansion are the energy derivatives with respect to the nuclear displacement coordinates. The negative of the first derivatives are referred to as "forces" or "gradients", whilst the second derivatives are usually designated as (harmonic) "force constants". The latter relate to molecular bonding properties and the main interest here lies in their determination.

A set of molecular force constants, or force field, can be determined empirically from a knowledge of molecular geometry and spectroscopic parameters. This approach has been dealt with in the previous section. However, for all but a few small molecules, there are difficulties in accumulating sufficient experimental data to calculate all the force constants.

An alternative approach is to derive these force constants (and molecular properties in general) from fundamental principles through ab initio quantum mechanical calculations. This is a completely independent route to

obtaining molecular force fields and is both supplementary and complementary to empirical harmonic force field studies.

Prior to dealing specifically with ab initio force constant evaluation however, a brief description of underlying theoretical models upon which their determination is based will be given.

### 1.3.2 AB INITIO MOLECULAR ORBITAL METHODS

In theoretical chemistry, a central objective has long been to derive quantitative molecular property expressions from the underlying interaction between constituent nuclei and electrons. Molecular properties can in general, be related to fundamental principles through quantum mechanics, in which the distribution and motion of the electrons and nuclei is governed by a wavefunction. This wavefunction is obtained from the well-known Schrödinger equation.

The term "ab initio" implies that the molecular orbital (MO) treatments are rigorous and do not involve parameterisation. Apart from exceptionally simple systems however, there are too many degrees of freedom to permit exact solutions and this necessitates the introduction of approximations.

A pre-requisite assumption is generally made with regard to the separability of the vibrational and electronic wavefunctions, in accordance with the Born-Oppenheimer

approximation (29). This allows electronic properties to be dealt with at fixed molecular geometries.

The simplest molecular orbital approximation methods are of the Hartree-Fock (HF) type, in which solutions to the electronic Schrödinger equation are found by a self-consistent field (SCF) method. In the HF method, an  $n$  electron wavefunction  $\Psi$ , is approximated as a single determinant according to the following expression:

$$\Psi = (n!)^{-1/2} \det | \chi_1 \chi_2 \dots \chi_n | \quad 1.33$$

The  $\chi_i$  term is a one-electron function, known as a spinorbital, which describes the distribution of a single electron. Each  $\chi_i$  is a function of four coordinates - one spin coordinate ( $s$ ) and three cartesian coordinates for the electron ( $x$ ,  $y$  and  $z$ ). In addition, each spinorbital  $\chi_i$  is further approximated as a linear combination of basis functions (30)  $\omega_m$

$$\chi_i(s, x, y, z) = \sum_m^N C_{mi} \omega_m \quad 1.34$$

The basis functions are normally spatial functions, (multiplied by a spin factor), which are centred at the nuclear position and depend principally on the nature of the nucleus and not the chemical environment. If the basis functions  $\omega_m$  are approximated to the atomic orbitals for the constituent atoms, then equation 1.34 is normally described as a linear combination of atomic orbitals (LCAO). Basis

functions will be considered in more detail in section 1.3.3.

It is also required to fix the unknown expansion coefficients  $C_{mi}$  of 1.34 to specify the HF wavefunction completely. These are determined by the variational method such that the expectation energy,

$$E = \int \Psi^* \hat{H} \Psi \, dr \quad 1.35$$

is as low as possible (within boundary restrictions). The energy  $E$ , obtained from equation 1.33 represents the closest approximation to the exact Schrödinger energy within the restriction of the single determinant wavefunction and infinite basis set approximation in the HF method.

HF energies are typically in error by about 1%. A large part of this error is attributable to the treatment of electronic interactions: the HF SCF wavefunction takes interactions into account only in average way. A more correct description would include the mixing of instantaneous electron correlation or electronic configurations. This is most commonly achieved by carrying out post-SCF calculations known as "configuration interaction" (CI) calculations, which involves swapping electrons between orbitals (usually taken to be the SCF MO's) to produce different electronic states. Symmetry restrictions limit the number of states which need to be considered since only those of the same symmetry as the

ground (reference) state contribute to the wavefunction. Nevertheless, even for small molecular systems there may still be a very large number of contributory electronic states and calculations soon become out of hand. The number of states considered is therefore usually limited to the two or three most important ones. For closed shell molecules, for example, only the ground and two excited states are most commonly used to define the wavefunction.

### 1.3.3 ORBITAL REPRESENTATION

The spatial part of the basis functions  $\omega_m$  of equation 1.32 in single centre (atomic) calculations are most conveniently represented as Slater type atomic orbitals (STO) (31), which have simple exponential terms of the form,

$$\theta = \exp(-\zeta r) \quad 1.36$$

These STO are good approximations to true atomic orbitals. However, in multicentre (molecular) systems integration in equation 1.35 is mathematically difficult to achieve if STO functions are used. Consequently, calculations are computationally difficult, particularly for larger molecular systems.

Alternatively, gaussian functions can be used (32). Indeed, nearly all modern ab initio MO calculations use gaussian basis functions. These have exponential parts of the form

$$\theta = \exp(-\gamma r^2)$$

1.37

and can be integrated much more readily. Although gaussian functions give an inferior description of atomic orbitals, especially for small values of  $r$ , a linear combination of gaussians can be used to represent a STO function:-

$$\exp(-\zeta r) \rightarrow \sum_k^K d_{ik} \exp(-\gamma_{ik} r^2) \quad 1.38$$

Such linear combinations may be referred to as "contracted gaussian functions" when the coefficients  $d_{ik}$  are fixed in proportion to each other. The larger the number of gaussians used, the closer the approximation to the STO. Detailed studies indicate that three gaussians per STO (i.e. STO-3G) are sufficient to reproduce the results from an STO (33).

These STO-nG are the smallest type of basis and are referred to as a "minimal basis" since only one basis function is used to represent each orbital. Thus, hydrogen for example, would have only one 1s function, whilst carbon would have 5 functions (1s, 2s, 2p<sub>x</sub>, 2p<sub>y</sub> and 2p<sub>z</sub>). Although minimal basis sets of the STO-nG type are computationally inexpensive, they are deficient in that the same size of basis function is used for all chemical environments.

Increased flexibility can be achieved by doubling the number of basis functions in the valence shell. Such basis

may be described as "split-valence" and a number of these have been developed for first and second row elements (34-40). The 3-21G basis (37,39) is computationally the most inexpensive. For first row elements, this basis set consists of 3-gaussian core functions, 2-gaussian functions for the inner valence region and a single (uncontracted) gaussian for the outer valence region. Thus a 3-21G basis set for carbon for example, would contain a core (1s) function, 2s and 2p inner valence functions and also 2s and 2p outer valence functions, giving a total of 9 basis functions. Other split-valence basis sets of this type differ only in the number of gaussian functions used to represent each orbital.

In addition to doubling the number of valence functions, the number of core functions can also be doubled. Such basis sets are referred to as "double-zeta" basis sets since there are two exponential (zeta) functions per atomic orbital. Further improvements in the description of the orbitals may be achieved by using three basis functions per orbital, which defines a "triple-zeta" basis set.

Generally, basis functions are energy-optimised in terms of atomic orbital functions. For molecular systems, the molecular orbitals may differ significantly from their atomic orbital equivalents, particularly in the valence shell. These differences can be accounted for by scaling the atomic orbital function exponent  $\zeta_i(\text{atom})$  according to equation 1.39

$$\zeta_i(\text{molecule}) = \alpha^{3/2} \zeta_i(\text{atom}) \quad 1.39$$

where  $\alpha$  is a scaling factor. The scaling factors are generally determined from a set of "standard" molecules and have been found to depart significantly from unity for hydrogen functions. For larger centres, the effects of molecular environment are less pronounced and are reflected in scaling factors closer to unity.

Better quality wavefunctions can be generated by supplementing basis sets with higher angular momentum terms known as "polarisation" functions. The first row 6-31G\* basis set as defined by Hariharan and Pople (41,42), for example, consists of a 6-31G split-valence set (35) plus a set of 6 second order uncontracted gaussian functions (which incorporate the complete set of atomic d functions). A more extensive basis set is the 6-31G\*\* (41,42), which also contains a set of p-type polarisation functions on each hydrogen. Large basis sets such as the 6-31G\*\* are very flexible and begin to approach the HF limit which is a limiting model for a HF wavefunction.

#### 1.3.4 SELECTION OF THEORETICAL MODEL AND BASIS SETS

There are a considerable number of ab initio routines both published and being developed. They range from simple HF models to highly sophisticated packages incorporating CI and more sophisticated corrections. The selection of a

particular routine is determined by two key factors:

(1) The host system. This is of prime importance since the type of computer system will dictate the feasibilities of the calculations. Specifically, limitations on computer time and space and its overall efficiency must be taken into consideration.

(2) The type of calculations to be performed. Obviously, an investigator will choose an appropriate ab initio model specific to his research interests, but he will also have to consider the accuracies required. Generally, as the degree of complexity of the ab initio package increases, so too does the sophistication of the calculations. This leads to better quality results but is offset by a corresponding increase in computational expense.

There are a very large number of basis sets in the literature and their production is also an on-going process. Selection of the basis functions for a particular calculation requires careful prior consideration. The adopted ab initio package can largely dictate and reduce the number of available basis functions. The choice however, may still be large. An investigator has therefore to choose a basis set which represents a compromise in terms of complexity of calculation and amount of computing effort in a similar fashion to that for the selection of an ab initio package. Larger basis sets naturally take longer to evaluate. (The computing time rises approximately as the

fourth power of the number of basis functions (43).) An understanding of the relative merits of different sets of functions must be ascertained in advance so that an appropriate basis set is selected for a particular task. Furthermore, the investigator must exercise caution when interpreting ab initio results since inherent trends and anomalous values may be attributable to the basis set and not to some physical process. For example, there is a tendency for HF bondlengths to be considerably less than experimental equivalents. Whilst it could be inferred that the experimental bondlengths are in error, it is more likely that the HF bondlengths are too short owing to deficiencies associated with the HF model.

#### 1.3.5 MOLECULAR ENERGY DIFFERENTIATION

Ab initio force constants  $F_{ij}$ , can be determined by double differentiation of the total ab initio molecular energy with respect to a set of nuclear coordinates  $q_i$  ( $i=1,2,\dots,n$ ) and  $q_j$  ( $j=1,2,\dots,n$ ), in the equilibrium configuration according to the following expression:

$$F_{ij} = (\delta^2 E / \delta q_i \delta q_j)_0 \quad 1.40$$

There are three methods by which the differentiation of the molecular energy can be accomplished:

- (a) Twice numerically,
- (b) Twice analytically
- and (c) First analytically and then numerically.

Method (a) had been originally adopted for force constant evaluation. This method requires the detailed calculation of a potential surface in terms of  $q_i$  and  $q_j$ , which necessitates a considerable amount of computing effort. In addition, method (a) leads to significant numerical inaccuracies, particularly beyond the first derivative (44).

For method (b) calculation of the double differential is performed in terms of variational parameters (44). In MO-SCF calculations, these parameters are generally difficult to obtain. In fact, they can be determined numerically by carrying out a series of calculations with different nuclear coordinates. Similarly to method (a) though, this requires a considerable degree of computing.

The third method, advocated by Pulay (45) and called the "force method" is generally accepted as the most economical and practical route to obtaining ab initio force constants. Furthermore, it makes possible an efficient iteration procedure to determine equilibrium nuclear configurations. This force method shall now be considered in more detail.

#### 1.3.5.1 THE FORCE METHOD

The key feature of the force method is the calculation of the first (analytical) derivative  $f_i$ , referred to as the gradient or force, in terms of nuclear coordinate  $q_i$  ( $i=1,2,\dots,n$ ) such that,

$$f_i = -(\delta E / \delta q_i) \quad 1.41$$

The variational parameters are determined so that they minimise the total energy. For the first derivative however, it is not necessary to know how the variational parameters change with the nuclear coordinates in computing the gradients. This is in contrast to method (b) where the variational parameters for the second derivative need to be obtained.

The gradients are best calculated in terms of cartesian coordinates. In subsequent calculation of the equilibrium geometry and force constants however, gradients in internal coordinates are more advantageous. Thus transformation of the two sets must be carried out in terms of the B matrix and using the relations given in section 1.2.1.

#### 1.3.5.2 EVALUATION OF FORCE CONSTANTS

To determine the ab initio quadratic force constants  $F_{ij}$ , the gradients  $f_i$  and  $f_j$ , must be differentiated numerically, in terms of the internal coordinates  $q_i$  and  $q_j$  (36). This may be done by applying distortions  $\Delta_i$  along respective internal coordinates and then calculating  $F_{ij}$  according to the following,

$$\begin{aligned} F_{ij} &= [f_j(\text{ref}) - f_j(\Delta_i)] / \Delta_i \\ &= [f_i(\text{ref}) - f_i(\Delta_j)] / \Delta_j \end{aligned} \quad 1.42$$

These equations can be referred to as "one-sided displacement" equations, which include the inherent assumption that cubic terms can be neglected. This is a reasonable assumption provided that the displacements are chosen to be very small. However, the effects of cubic anharmonicity can be eliminated completely, and hence more reliable force constant values obtained, if the gradient is evaluated for two displacements (i.e.  $\pm\Delta_i$ , etc.) along each coordinate. In addition to similar quadratic force constant expressions, i.e.,

$$\begin{aligned} F_{ij} &= [f_j(-\Delta_i) - f_j(+\Delta_i)] / 2\Delta_i \\ &= [f_i(-\Delta_j) - f_i(+\Delta_j)] / 2\Delta_j \end{aligned} \quad 1.43$$

the "two-sided distortion" scheme allows the calculation of dominant diagonal and semi-diagonal cubic force constants  $F_{iij}$  from the following expression:

$$F_{iij} = [2f_j(\text{ref}) - f_j(+\Delta_i) - f_j(-\Delta_i)] / \Delta_i^2 \quad 1.44$$

### 1.3.5.3 THEORETICAL EQUILIBRIUM CONFIGURATION

The theoretical potential surface for a molecule defined in terms of internal coordinates, will in general have a global energy minimum which constitutes its equilibrium nuclear configuration.

If an approximate force constant matrix is known and the surface is approximately quadratic, then a linear

convergence method called the "force relaxation method" (45) can be used to determine the equilibrium configuration. In this method, an initial estimate of the internal coordinates is calculated, usually from experimental geometry parameters. An SCF calculation is then performed at the point on the potential surface corresponding to the initial (experimental) geometry. The gradients  $f_i$  are then evaluated in terms of equation 1.41. From a knowledge of these gradients, a better estimation of the theoretical internal coordinate vector  $Q_{i+1}$  and hence theoretical equilibrium can be obtained from the following expression:

$$Q_{i+1} = Q_i + \Delta Q_i = Q_i + F_o^{-1} f_i \quad 1.45$$

where  $F_o$  is the estimated force constant matrix. If  $F_o$  is equal to its true value and the potential surface is quadratic, then convergence on equilibrium can theoretically be achieved in one step. In practice however, this is not usually the case. Nevertheless, the final equilibrium configuration is usually reached after only a few iterations. It should be noted however, that in the linear convergent relaxation method the force constant matrix only determines the rate of convergence.

An extension to the relaxation method to include force constant matrix corrections can result in more rapid attainment of equilibrium.

Adoption of a theoretical nuclear configuration as a

reference geometry in order to calculate ab initio force constant may not be automatic. The choice of reference geometry will be dealt with in the following section.

### 1.3.6 SELECTION OF REFERENCE GEOMETRY

Selection of the reference geometry requires careful consideration prior to performing ab initio force constant calculations. Bond stretching force constants, in particular are very sensitive to the reference geometry (43).

If calculations are carried out using a theoretically determined geometry then force constant evaluation is performed relative to a minimum on the theoretical potential energy curve.

Alternatively, if the experimental geometry is used to calculate ab initio force constants, then this is equivalent to adding an empirical linear term to the theoretical potential function, shifting the position of the minimum to the experimental value. The introduction of these empirical elements can easily be justified (43) since the HF model is unable to calculate accurately the core-core repulsion interaction term. This leads to erroneous HF interatomic distances. This discrepancy is larger than errors resulting from adoption of  $r_o$ ,  $r_z$  or other experimental geometry parameters which represent deviations from equilibrium.

Use of an experimental geometry in ab initio calculations however, can affect quadratic and higher force constants. Specifically, addition of linear geometric corrections, when curvilinear valence coordinates are used can produce pseudo-quadratic and higher terms.

A systematic approach to empirically corrected theoretical geometries has been outlined by Blom et al. (46) and advocated by Pulay et al. (36). Their method is to apply empirical corrections to the theoretical geometries for a given basis set. The corrections have been established for small molecules and for the most part apply to bond lengths only.

## CHAPTER 2

### HIGH RESOLUTION INFRARED STUDIES OF KETENE

#### 2.1 INTRODUCTION

The molecule ketene ( $\text{H}_2^{12}\text{C}^{12}\text{C}^{16}\text{O}$ ) is classified as an asymmetric rotor belonging to the  $\text{C}_{2v}$  point group. If the molecular axis convention recommended by Mulliken and Herzberg is adopted ( $xyz \sim cba$ ), then the nine fundamental vibrations factorize such that the totally symmetric vibrations  $\nu_1 - \nu_4$  belong to the  $\text{A}_1$  species, the out-of-plane vibrations  $\nu_5$  and  $\nu_6$  to the  $\text{B}_1$  species, and the in-plane vibrations  $\nu_7 - \nu_9$  to the  $\text{B}_2$  species. This numbering follows the convention used in publications over the past 15 years, but differs from that used in earlier work where the  $\text{B}_1$  and  $\text{B}_2$  labels are interchanged, with a consequent renumbering of  $\nu_5 - \nu_9$ .

Infrared studies of ketene date back to 1937 (47), although it was not until post-1950 that rotational structure in gas phase spectra was analysed at low resolution (48-53). Subsequent study at medium resolution has been restricted to the region below  $1050\text{cm}^{-1}$  (54), which

contains  $\nu_5$ ,  $\nu_6$ ,  $\nu_8$  and  $\nu_9$ , whilst at high resolution only the region above  $3100\text{cm}^{-1}$  containing  $\nu_7$  and the  $\nu_2 + \nu_8$  combination (55) has been studied. Very recently, an analysis of the region below  $900\text{cm}^{-1}$  of  $\text{D}_2\text{CCO}$  has been made at high resolution (56).

The studies reported here deal principally with the four A-type  $\nu_1 - \nu_4$  fundamentals. The two C-type vibrations  $\nu_5$  and  $\nu_6$  and two of the three B-type vibrations  $\nu_7$  and  $\nu_8$  were also reexamined. In addition to these, three overtone levels  $2\nu_5$ ,  $2\nu_6$ , and  $2\nu_8$  were also studied.

On account of the wide spread of individual bands in the gas phase spectrum, arising principally from the very large A rotational constant, the possibility of perturbation within the bands was anticipated. Indeed, a-axis Coriolis interactions affecting  $\nu_5$ ,  $\nu_6$ ,  $\nu_8$  and  $\nu_9$  have most recently been studied by Nemes (54) and a probable Fermi resonance interaction between  $\nu_7$  and  $\nu_2 + \nu_8$  was reported by Johns et al. (55). In order to assist in the elucidation of these perturbations, the spectra of  $\text{H}_2^{13}\text{CCO}$ ,  $\text{H}_2\text{C}^{13}\text{CO}$  and  $\text{D}_2\text{CCO}$  have also been studied.

From the above studies,  $\text{H}_2\text{CCO}$  and  $\text{D}_2\text{CCO}$  frequencies and  $^{13}\text{C}$  frequency shifts were collected to be used to calculate a revised force field for ketene. The  $^{13}\text{C}$  shifts in particular were anticipated to be invaluable in helping to distinguish between alternative force field solutions to the  $\text{B}_1$  symmetry block and also to define the  $\text{A}_1$  block more

accurately.

## 2.2 EXPERIMENTAL PROCEDURE

### (a) Synthesis of ketene

Ketene was prepared by hot wire pyrolysis of acetone under high vacuum (54). The ketene produced was separated from most other products by repeated fractional distillation through a series of low temperature baths and condensed at  $-154^{\circ}\text{C}$ . After each distillation, preliminary low resolution infrared scans ( $\sim 1\text{cm}^{-1}$ ) in the region  $4000 - 400\text{cm}^{-1}$  of the distillate in a gas cell at 25torr were carried out to check purity. Fractional distillation was repeated until impurity absorptions were removed from the spectrum. However, a small trace of  $\text{CO}_2$  always remained in the distillate, its condensation temperature being close to that of ketene.  $\text{CO}_2$  absorptions were anticipated to interfere only in the  $\nu_5$  and  $\nu_6$  region of the spectrum and since these vibrations were only to be examined superficially, further purification was deemed unnecessary. Samples of  $\text{H}_2\text{CCO}$ ,  $\text{H}_2\text{C}^{13}\text{CO}$ ,  $\text{H}_2^{13}\text{CCO}$  and  $\text{D}_2\text{CCO}$  were obtained in this manner from the relevant isotopically substituted acetones.

## (b) Spectra

Spectra were recorded on the Nicolet 7199 FTIR at maximum resolution ( $\sim 0.05\text{cm}^{-1}$ ), using 20cm and multi-reflection cells of up to 9m pathlength, with gas pressures of up to 2torr. Liquid  $\text{N}_2$  cooled In-Sb ( $> 2000\text{cm}^{-1}$ ) and Hg-Cd-Te ( $< 2000\text{cm}^{-1}$ ) detectors were used and any interference from atmospheric  $\text{CO}_2$  and  $\text{H}_2\text{O}$  was minimised by computer subtraction of background spectra. Calibration was effected in terms of the internal He-Ne laser and the highly accurate CO fundamental absorption frequencies, giving an estimated internal accuracy of measurement of  $\pm 0.002\text{cm}^{-1}$  and an absolute accuracy of better than  $\pm 0.005\text{cm}^{-1}$ .

## 2.3 METHOD OF ANALYSIS OF ROTATIONAL STRUCTURE

### (a) A-type

Assignments in the A-type bands of ketene were greatly simplified by calculation of the appropriate ground state combination differences (GSCD) from the precisely known ground state rotational constants given in table 2.1. These were determined from a combination of microwave and infrared studies by Johns et al. (55).

For subbands, where the effects of asymmetry are slight at the resolution available ( $K_a > 2$ , and  $K_a = 2$ ,  $J < 15$ ), transitions were analysed in terms of a symmetric rotor

energy expression with corrections for asymmetry made in terms of the second-order expressions of Polo (57). This method, first employed by Lafferty et al. for diborane (58), involves essentially the plotting of  $[\nu_{R_{Ka}}^{(J-1)} + \nu_{P_{Ka}}^{(J+1)}]/2$  against  $J^2$  to yield a subband origin,  $\nu_{Ka}^0$ , and  $\Delta\bar{B}_{Ka} = (\bar{B}'_{Ka} - \bar{B}'')$  for the subbands in question. The method makes the assumption that  $\Delta_J' = \Delta_J''$  and  $\Delta_{JK}' = \Delta_{JK}''$ , which was found to be perfectly reasonable for the quality of the spectra. The subband origins, corrected if necessary to an averaged value of  $\Delta\bar{B}$ , were then fitted to a quadratic equation in  $K_a^2$ ,

$$\begin{aligned} \nu_{Ka}^0 &= \nu^0 + [(A' - \bar{B}') - (A'' - \bar{B}'')]K_a^2 - (\Delta_K' - \Delta_K'')K_a^4 \\ &= \nu^0 + \Delta(A - \bar{B})K_a^2 - (\Delta_K' - \Delta_K'')K_a^4 \end{aligned} \quad 2.1$$

from which the vibrational band origin  $\nu^0$ , and rotational  $\Delta A$  and  $(\Delta_K' - \Delta_K'')$  values can be determined.

Table 2.1. Ground state parameters<sup>a</sup> for H<sub>2</sub>CCO, cm<sup>-1</sup>.

A	9.40921(40)
B	0.343370(1)
C	0.330737(1)
$\Delta_J$	$1.13(1) \times 10^{-7}$
$\Delta_{JK}$	$1.588(1) \times 10^{-5}$
$\Delta_K$	$7.85(29) \times 10^{-4}$
$\delta_J$	$4.8(1) \times 10^{-9}$
$\delta_K$	$1.10(1) \times 10^{-5}$

<sup>a</sup> I<sup>r</sup> representation

Refinements made in terms of the full quartic asymmetric rotor model have been performed to both ground and upper state combination differences (USCD) for transitions involving  $K_a < 2$ , where possible. These enable values for  $\Delta B$ ,  $\Delta C$  and  $(\Delta_J' - \Delta_J'')$  to be determined. In cases where perturbations appeared to have little effect on the upper state constants, higher (and hence unsplit)  $K_a$  transitions could be included in this refinement. In other cases, the effects of perturbations precluded this.

(b) B and C-type bands

For B and C-type bands, only preliminary studies of the Q branch structures have been made, primarily to determine  $^{13}\text{C}$  frequency shifts. This has been achieved through simple contour comparisons where assignments to the  $^p_{Q_{K_a}}$  and  $^r_{Q_{K_a}}$  structure were aided by the nuclear spin statistical weights which render even  $K_a$  transitions at a third of the intensity of odd  $K_a$  transitions in  $\text{H}_2\text{CCO}$  species. Lower  $^p_{Q_{K_a}}$  and  $^r_{Q_{K_a}}$  transitions, especially  $^p_{Q_1}$  and  $^r_{Q_0}$  were principally used to determine shifts since these are least affected by isotopic changes in the major a-axis rotational resonances which are present. An analysis of the effects of these resonances in terms of Q branch structures has previously been reported for the B and C-type vibrations lying below  $1000\text{cm}^{-1}$  (54).

## 2.4 RESULTS AND DISCUSSION OF INDIVIDUAL BAND ANALYSES

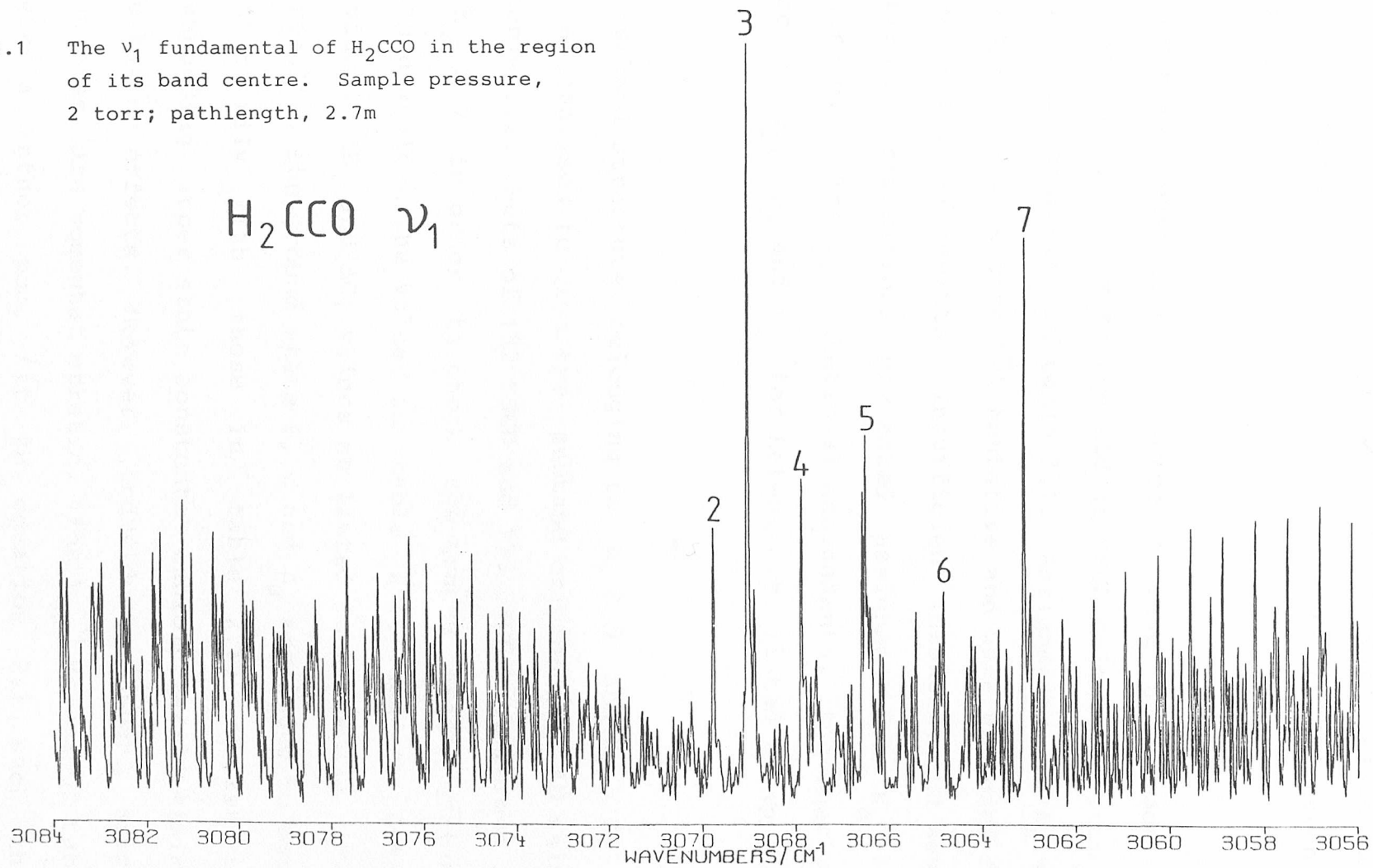
For all the fundamentals and overtones studied, the spectra of three isotopomers were available for examination, namely  $\text{H}_2\text{CCO}$ ,  $\text{H}_2\text{C}^{13}\text{CO}$  and  $\text{H}_2^{13}\text{CCO}$ , and for the  $A_1$  fundamentals,  $\text{D}_2\text{CCO}$  spectra were also available. Instrumentation limitations prevented examination of the low-lying  $\nu_9$  vibration in any isotopomeric form.

Individual bands are discussed below roughly in order of decreasing degrees of complexity and thoroughness of investigation. The A-type vibrations ( $\nu_1$ ,  $\nu_2$ ,  $\nu_3$ ,  $\nu_4$ ,  $2\nu_5$ ,  $2\nu_6$  and  $2\nu_8$ ), and in particular the fundamentals were most comprehensively studied and are discussed first. The contour comparison analyses of two of the B-type vibrations ( $\nu_7$  and  $\nu_8$ ) are then discussed and finally, similar contour comparisons made of the C-type vibrations ( $\nu_5$  and  $\nu_6$ ) are considered.

(a)  $\nu_1$ ,  $\text{CH}_2$  symmetric stretch,  $3070\text{cm}^{-1}$

Two features are immediately apparent from inspection of the central Q structure of this band, shown in figure 2.1. Individual  $Q_{Ka}$  branches are sharp features indicating that  $\bar{B}' \approx \bar{B}''$ , whilst a marked subband degradation to lower frequency infers that the A constant decreases significantly from its ground state value. This marked degradation pattern is a common feature of A-type bands in ketene spectra.

Figure 2.1 The  $\nu_1$  fundamental of  $\text{H}_2\text{CCO}$  in the region of its band centre. Sample pressure, 2 torr; pathlength, 2.7m



Assignments to the Q structure are straightforward due to the nuclear spin statistical weights which result in odd  $K_a$  levels having three times the weighting of even  $K_a$  levels.

Over 300 unambiguous assignments have been made for  $J \leq 36$  and  $K_a \leq 7$ , with the aid of GSCD calculated from the rotational constants in table 2.1. Assignments to  $K_a = 2^\pm$  and 6 series were somewhat tentative and were excluded from upper state refinements. Insufficient intensity and severe overlap of transitions prevented assignment to  $K_a > 7$  structure. (The  $\nu_1$  rotational assignments, together with those for  $\nu_2$ ,  $\nu_3$  and  $\nu_4$  for ketene are listed in appendix A).

Subband structure belonging to  $K_a \geq 3$  and  $K_a = 2$  (low J) was analysed to give the subband origins and  $\Delta\bar{B}$  values in table 2.2. Sets of 192 GSCD and 175 USCD were formed for  $0 \leq K_a \leq 7$  in order to check the ground state constants obtained against the values in table 2.1, and to obtain individual  $\Delta B_1$  and  $\Delta C_1$  values as listed in table 2.2. From the results, the ground state B, C and  $\Delta_J$  are found to agree satisfactorily with those in table 2.1, whilst the corresponding upper state constants exhibit fairly minimal perturbation effects. However, individual subband origin frequencies are somewhat erratic. The  $\nu_{K_a}^0$  values of table 2.2 give a rather poor fit to equation 2.1 such that extrapolation to a reliable vibrational band origin is difficult, and the best fit parameters predict a change in

Table 2.2. Results of analysis of  $\nu_1$  fundamental of  $\text{H}_2\text{CCO}$ ,  $\text{cm}^{-1}$ .

$K_a$	$\Delta\bar{B} \times 10^4$	$\nu_{Ka}^\circ$
2	-3.68(11)	3069.779(2)
3	-3.27(4)	69.073(2)
4	-3.70(2)	67.914(1)
5	-4.18(2)	66.616(1)
6	-4.14(38)	64.962(7)
7	-3.72(9)	63.179(4)
Average		-3.78(17)

	<u>GS constants</u>	<u>US constants</u>	<u>US - GS</u>
B	0.343436(33)	0.343096(43)	-0.000340(77)
C	0.330616(32)	0.330199(42)	-0.000418(74)
$\Delta_J$	$1.0(1) \times 10^{-7}$	$0.9(2) \times 10^{-7}$	$-0.1(3) \times 10^{-7}$
No. of data	192	175	
		$\Delta\bar{B}$	-0.000379(76)

$\Delta_K$  of about 30%, which seems very large.

Spectra of the corresponding vibration in  $H_2C^{13}CO$  and  $H_2^{13}CCO$  were examined carefully to try to elucidate the origin of this behavior. As expected, both bands have the same overall structural appearance as that for ordinary ketene, and assignment to the very sharp Q branch features for  $2 \leq K_a \leq 7$  is straightforward. For ketene itself, the observed Q branch maxima and Q branch origins of table 2.2, determined from observed J structure, are almost identical, so the observed Q branch maxima in  $\nu_1$  of  $H_2C^{13}CO$  and  $H_2^{13}CCO$  were subjected to analysis in terms of equation 2.1. The results for all three isotopic species are collected in table 2.3, where it will be seen that both  $^{13}C$  species, particularly  $H_2^{13}CCO$ , exhibit even more erratic behaviour than ordinary ketene. It appears that in  $H_2CCO$ , there is a small perturbation localised around  $K_a = 3$  and 4, whereas in both  $H_2C^{13}CO$  and  $H_2^{13}CCO$  there is a considerably larger perturbation localised around  $K_a = 2$  and 3. This can readily be seen in figure 2.2, where the spectra are compared.

Table 2.4 lists a number of combination levels likely to be either in Fermi resonance or a-axis Coriolis resonance with  $\nu_1$  and thus cause or contribute to the observed perturbations to the  $\nu_1$  spectrum. The  $\nu_4 + 2\nu_8$  level ( $A_1$ ), calculated to lie almost coincident with  $\nu_1$  in  $H_2CCO$ , and which can be in a Fermi resonance with  $\nu_1$ , seems the most probable source of perturbation. However, by itself this

Table 2.3. Subband  
ketenes,

$K_a$	$H_2CCO$	
	OBS	O - C
2	3069.779	-0.029
3	69.073	0.050
4	67.914	-0.030
5	66.616	0.025
6	64.962	-0.027
7	63.179	0.009
8		
$\nu^O$	3070.44(10)	
$\Delta(A-\bar{B})$	-0.1600(96)	
$(\Delta_{K'} - \Delta_{K''})$	-0.00024(18)	
$\nu^O$	3070.40(36)	
$\Delta(A-\bar{B})$	-0.1579(245)	
$(\Delta_{K'} - \Delta_{K''})$	-0.00021(37)	

analyses for  $\nu_1$  fundamental of isotopic  
 $\text{cm}^{-1}$ .

$\text{H}_2\text{C}^{13}\text{CO}$		$\text{H}_2^{13}\text{CCO}$		$\text{D}_2\text{CCO}$	
OBS	O - C	OBS	O - C	OBS	O - C
3069.707	0.101	3064.252	0.221	2267.093	0.003
68.680	-0.151	62.965	-0.248	66.794	-0.006
67.775	0.017	62.018	-0.073	66.396	0.001
66.424	0.023	60.735	0.046	65.880	0.005
64.801	0.027	59.085	0.048	65.242	-0.001
62.879	-0.018	57.210	0.038	64.498	-0.002
		55.099	-0.038	63.649	0.001
3070.23(24)		3064.70(35)		2267.323(8)	
-0.1569(238)		-0.1672(264)		-0.05820(65)	
-0.00015(44)		-0.00028(38)		-0.000012(10)	
<u>'Best fit' estimates</u>					
3070.18(6)		3064.62(9)			
-0.1510(40)		-0.1597(45)		as above	
-0.00043(62)		-0.00172(50)			

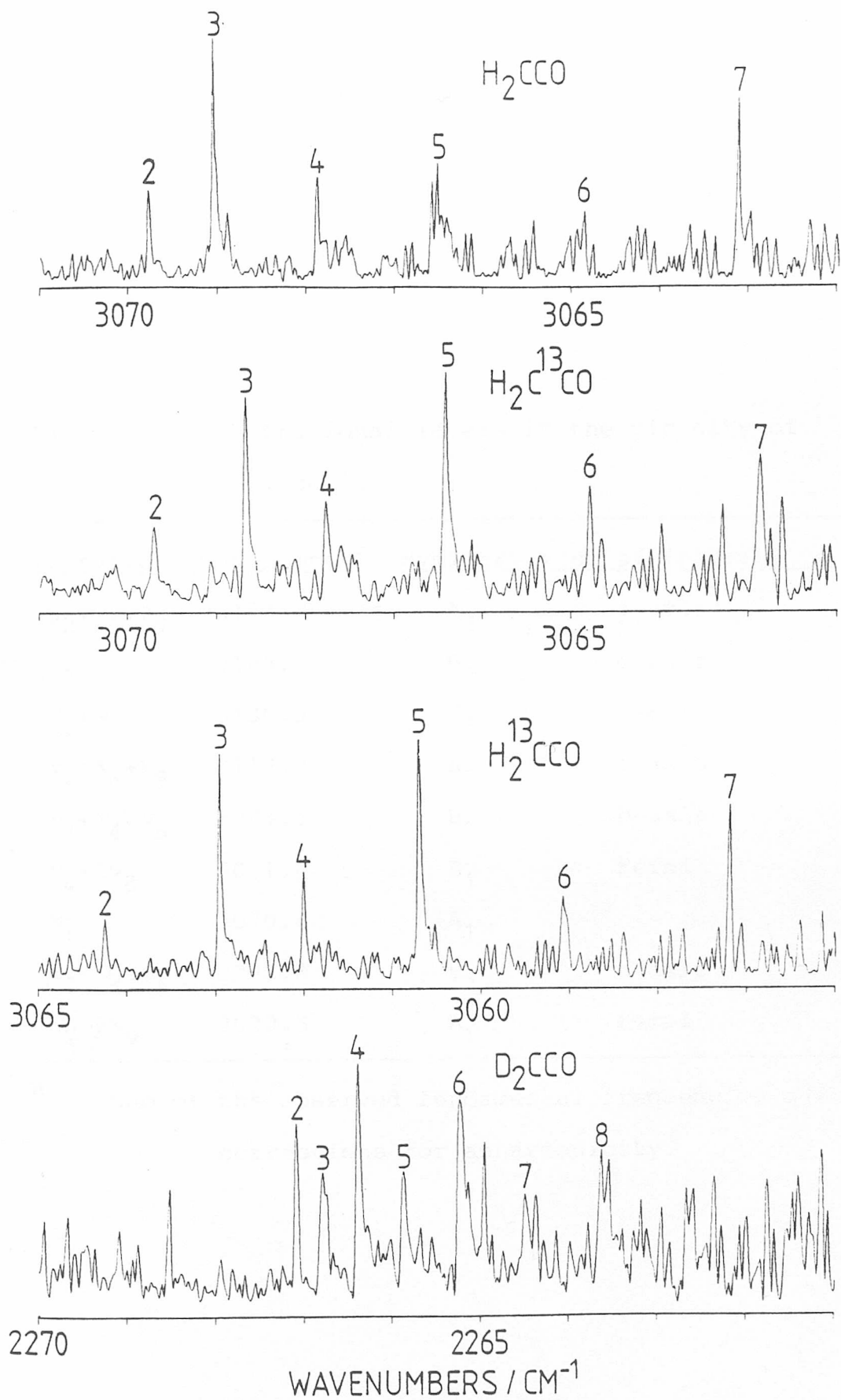


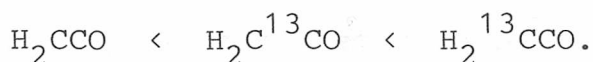
Figure 2.2 Comparison of the Q branch structures in  $\nu_1$  fundamentals of  $\text{H}_2\text{CCO}$ ,  $\text{H}_2\text{C}^{13}\text{CO}$ ,  $\text{H}_2^{13}\text{CCO}$  and  $\text{D}_2\text{CCO}$ .

Table 2.4. Vibrational levels in the vicinity of  $\nu_1$ ,  $\text{cm}^{-1}$ .

<u>Vibration</u>	<u>Wavenumber</u> <sup>a</sup>	<u>Symmetry</u>	<u>Type of interaction</u>
$\nu_2 + \nu_5 + \nu_9$	3178.8	A <sub>2</sub>	a-axis
$\nu_7$	3165.3	B <sub>2</sub>	c-axis
$\nu_2 + \nu_8$	3130.3	B <sub>2</sub>	c-axis
$\nu_2 + \nu_6 + \nu_9$	3119.8	A <sub>2</sub>	a-axis
$\nu_3 + \nu_4 + \nu_5$	3091.3	B <sub>1</sub>	b-axis
$\nu_4 + 2\nu_8$	3071.6	A <sub>1</sub>	Fermi
$\nu_1$	3070.4	A <sub>1</sub>	-
$\nu_3 + \nu_4 + \nu_6$	3032.3	B <sub>1</sub>	b-axis
$\nu_2 + 2\nu_9$	3030.5	A <sub>1</sub>	Fermi

<sup>a</sup> Sum of the observed fundamental frequencies with no corrections for anharmonicity.

seems insufficient to explain the observed effects.  $\nu_4 + 2\nu_8$  is predicted to have a value of  $\Delta A$  of about  $+1.5\text{cm}^{-1}$  (which is calculated from Coriolis contributions to  $\Delta A$ , see table 1.2, determined from force field calculations (59)). The interacting vibration would thus exhibit a very large upward subband degradation, but should experience downward  $^{13}\text{C}$  frequency displacements in the region of  $20\text{cm}^{-1}$  in both  $^{13}\text{C}$  species. This should lead to perturbations in  $\nu_1$  of higher  $K_a$  levels in the  $^{13}\text{C}$  species than in ketene itself, since the vibrational separations are larger but decrease with increasing  $K_a$ . This is the opposite effect to that observed, and also cannot explain why the perturbation effects appear to increase markedly in the order



The fundamental  $\nu_4$  (see section 2.4(d)) is highly perturbed by Fermi resonance itself, which thus casts doubt on the reliability of the harmonic predictions for  $\nu_4 + 2\nu_8$ . Less likely, but possible contributory sources of perturbation in table 2.4 are the inactive  $A_2$  combinations  $\nu_2 + \nu_5 + \nu_9$  and  $\nu_2 + \nu_6 + \nu_9$ , which could Coriolis interact locally with  $\nu_1$  through rotation about the a-axis. In spite of not knowing their anharmonicity corrections, both levels seem too far separated from  $\nu_1$  in all isotopic species to be a contributory factor to the observed effects.

The 'best estimate' vibration frequencies of  $\nu_1$  in  $\text{H}_2\text{CCO}$ ,  $\text{H}_2\text{C}^{13}\text{CO}$  and  $\text{H}_2^{13}\text{CCO}$ , have been extrapolated from the

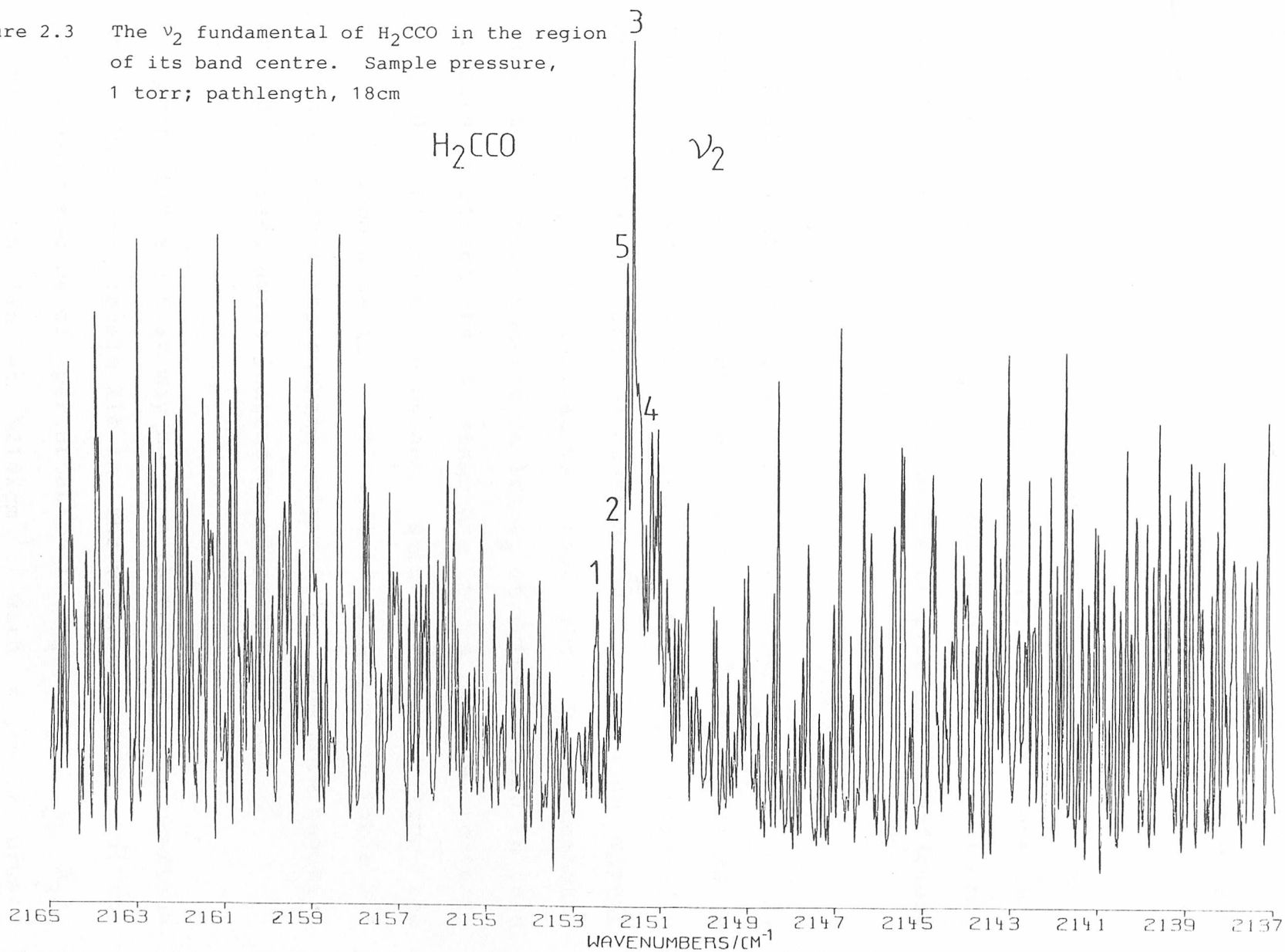
least perturbed Q branches observed to obtain the parameters in the lower half of table 2.3. The band origin of  $\nu_1$  for  $\text{H}_2\text{CCO}$  is not well defined. The values of  $(\Delta_K' - \Delta_K'')$  have little physical significance, being simply the mathematical values to improve the quality of the fit.

The spectrum of the  $\nu_1$  fundamental of the  $\text{D}_2\text{CCO}$  presents similar sharp and readily assigned subband Q branches, supported by observed J structure, remembering that in this case the nuclear spin statistical weights are such that even  $K_a$  : odd  $K_a$  have weights in the ratio 2 : 1. In contrast to the hydrogenated ketenes, the subband structure analyses perfectly in terms of equation 2.1, as shown in table 2.3, yielding the parameters listed. This demonstrates the quality of fit that can be achieved, and confirms that the effects observed in  $\text{H}_2\text{CCO}$  ketenes are genuine. The spectrum around the band centre is included in figure 2.2 for comparison.

(b)  $\nu_2$ , CCO asymmetric stretch,  $2152\text{cm}^{-1}$

In contrast with the other A-type bands of ketene, the Q structure of the  $\nu_2$  band does not exhibit discrete, sharp  $Q_{K_a}$  absorptions, but rather consists of overlapping structures resulting in an almost continuous overall Q branch, as shown in figure 2.3. Close inspection indicates a general downwards degradation of subbands with a downwards degradation of the J structure within each subband, inferring that  $A'' > A'$  and  $\bar{B}'' > \bar{B}'$ . The large degree of

Figure 2.3 The  $\nu_2$  fundamental of  $\text{H}_2\text{CCO}$  in the region of its band centre. Sample pressure, 1 torr; pathlength, 18cm



overlapping of structure inhibited assignment to most of the Q branch structure, except for the  ${}^qQ_3$  absorption, which is characteristically the most intense feature of these A-type bands.

With the aid of GSCD, assignment to P and R branch structure for  $J \leq 36$  and  $K_a = 1^\pm, 2^\pm, 3, 4, 5$  have been made. Assignments to  $K_a = 0^+$  and  $\geq 6$  structure were not possible due respectively to severe overlap and insufficient intensity in the spectra.

Analysis of structure for  $K_a > 3$  and  $K_a = 2$  (low J) subbands yields the subband origins and  $\Delta\bar{B}$  values listed in table 2.5. The subband variation in the rather precisely defined  $\Delta\bar{B}$  values and the observation that  ${}^qQ_5$  lies between  ${}^qQ_2$  and  ${}^qQ_3$  is indicative that the  $\nu_2$  fundamental experiences perturbation to its  $K_a$  structure, which in turn appears to affect its J structure to a smaller extent. Individual B' and C' constants were determined from the  $K_a = 1^\pm$  subband series. It will be observed in table 2.5 that the higher the subband origin lies, the more negative the B becomes, again indicative of perturbation.

From table 2.6 it may be seen that a number of overtone and combination levels lie in the vicinity of  $\nu_2$ , but the most likely source of perturbation is  $\nu_4 + \nu_5 + \nu_9$  ( $A_2$ ), calculated to lie at  $\sim 2142\text{cm}^{-1}$  with a small upward degradation. This combination can Coriolis interact with  $\nu_2$  through molecular rotation about the a-axis. Such an

Table 2.5. Results of analysis of  $\nu_2$  fundamental of  $\text{H}_2\text{CCO}$ ,  $\text{cm}^{-1}$ .

$K_a$	$\Delta\bar{B} \times 10^3$	$\nu_{Ka}^0$
1	-2.217(48)	2152.475(5)
2	-2.094(15)	2152.181(2)
3	-1.896(10)	2151.738(5)
4	-1.883(13)	2151.152(3)
5	<u>-1.964(4)</u>	2151.911(2)

Average -1.959(95)

'Best estimate' parameters

$\nu^0$	2152.56(5)
$\Delta(A-\bar{B})$	-0.092(8)

Table 2.6. Vibrational levels in the vicinity of  $\nu_2$ ,  $\text{cm}^{-1}$ .

<u>Vibration</u>	<u>Wavenumber<sup>a</sup></u>	<u>Symmetry</u>	<u>Type of interaction</u>
$2\nu_4$	2232.0	$A_1$	Fermi
$\nu_4 + \nu_5 + \nu_6$	2231.6	$A_1$	Fermi
$\nu_4 + 2\nu_6$	2172.6	$A_1$	Fermi
$\nu_2$	2152.6	$A_1$	-
$2\nu_5 + \nu_8$	2152.4	$B_2$	c-axis
$\nu_4 + \nu_5 + \nu_9$	2142.3	$A_2$	a-axis
$\nu_4 + \nu_8$	2093.8	$B_2$	c-axis
$\nu_5 + \nu_6 + \nu_8$	2093.4	$B_2$	c-axis
$\nu_4 + \nu_6 + \nu_9$	2083.3	$A_2$	a-axis

<sup>a</sup> Sum of the observed fundamental frequencies with no corrections for anharmonicity.

interaction is  $K_a$ -dependent and could manifest itself in an increasing upward displacement of  $K_a$  structure in  $\nu_2$  as  $K_a$  increases, as observed. The effect is small, as is to be expected for interaction between a fundamental and ternary combination. It may also be seen from table 2.6 that the combination vibration  $\nu_8 + 2\nu_5$  ( $B_2$ ) also lies very close to  $\nu_2$ . This combination should degrade very rapidly to higher frequencies ( $\Delta A \approx +3\text{cm}^{-1}$ ) and the c-axis Coriolis interaction possible here may contribute to the variation of the subband  $\Delta\bar{B}$  values observed in  $\nu_2$ . Approximate estimates of the  $\nu_2$  vibrational frequency and  $\Delta(A - \bar{B})$  value may be obtained by considering the  $K_a = 1, 2$  and  $3$  subbands to be essentially unperturbed, giving the parameters at the bottom of table 2.5.

The  $\nu_2$  fundamentals of  $\text{H}_2\text{C}^{13}\text{CO}$  and  $\text{H}_2^{13}\text{CCO}$  have also been studied. Although visually similar to the  $\text{H}_2\text{CCO}$  band, assignments can fairly readily be made for  $\text{H}_2\text{C}^{13}\text{CO}$ , but not at all for  $\text{H}_2^{13}\text{CCO}$ , where the rotational structure appears to be very confused. For  $\text{H}_2\text{C}^{13}\text{CO}$ , the  $\nu_2$  vibration shifts downwards by some  $56.5\text{cm}^{-1}$ , and now lies below both the probable perturbing levels. The shift for  $\text{H}_2^{13}\text{CCO}$  is only  $5.3\text{cm}^{-1}$ , and the perturbation present should be somewhat similar to those found in  $\text{H}_2\text{CCO}$ . For  $\text{H}_2\text{C}^{13}\text{CO}$ , assigned structure enables the  $K_a = 1, 2, 3,$  and  $5$  subband origins to be determined and analysed. Comparison of the results for  $\text{H}_2\text{CCO}$  and  $\text{H}_2\text{C}^{13}\text{CO}$ , shown in table 2.7, reveals a marked change in the  $\Delta(A - \bar{B})$  constant. This is considered to be evidence of a small Fermi resonance with the lower lying

Table 2.7. Subband analysis for  $\nu_2$  fundamental  
of isotopic ketenes,  $\text{cm}^{-1}$ .

$K_a$	$\text{H}_2\text{CCO}$		$\text{H}_2\text{C}^{13}\text{CO}$		$\text{H}_2^{13}\text{CCO}$	$\text{D}_2\text{CCO}$	
	OBS	O - C	OBS	O - C		OBS	O - C
1	2152.475	0.007	2095.924	-0.028	No assignments made due to confused structure	-	-
2	2152.181	-0.011	2095.904	0.022		2120.346	-0.003
3	2151.738	0.004	2095.780	0.014		2120.199	0.011
4	(2152.152) <sup>a</sup>	-	-	-		2119.980	-0.016
5	(2151.911) <sup>a</sup>	-	2095.386	-0.007		2119.814	0.010
6						2119.652	-0.002
7						(2119.074) <sup>a</sup>	-
8						(2118.137) <sup>a</sup>	-
$\nu^0$	2152.56(5)		2095.97(6)		2147.2 <sup>b</sup>	2120.49(4)	
$\Delta(\text{A}-\bar{\text{B}})$	-0.092(8)		-0.0233(45)		-	-0.0372(54)	
$(\Delta_{K'} - \Delta_{K''})$	-		-		-	-0.00039(13)	

<sup>a</sup> Values not used in estimates of vibration - rotation parameters.

<sup>b</sup> Estimated from visual inspection of spectrum. See Figure 2.4.

level  $2\nu_8$ , which lies much closer to  $\nu_2$  in  $\text{H}_2\text{C}^{13}\text{CO}$  than in  $\text{H}_2\text{CCO}$  or  $\text{H}_2^{13}\text{CCO}$ , due to the large downward shift of  $\nu_2$  in  $\text{H}_2\text{C}^{13}\text{CO}$ .  $2\nu_8$  exhibits a very large upward subband degradation (see section 2.4(g)). For  $\text{H}_2^{13}\text{CCO}$ , only an approximate vibration frequency, estimated visually from the observed Q branch can be quoted. The central regions of all three spectra are compared in figure 2.4, where the different Q branch spacings in  $\text{H}_2\text{CCO}$  and  $\text{H}_2\text{C}^{13}\text{CO}$  can readily be seen.

In the case of  $\text{D}_2\text{CCO}$ , the subband Q branch structure is once again sharp and well-defined as shown at the bottom of figure 2.4. Subband origins for  $K_a = 2 - 8$  are listed in table 2.7 and give evidence of a minor perturbation and a crossing of energy levels between  $K_a = 6$  and 7. Subband origins appear to be pushed upwards for  $K_a \leq 6$  and downwards for  $K_a \geq 7$ . Both  $\nu_3 + \nu_5 + \nu_9$  ( $A_2$ ) and  $\nu_3 + 2\nu_6$  ( $A_1$ ) lie close to  $\nu_2$  and may contribute to the observed effects. By analysing only the least perturbed subband origins, the vibration frequency has been estimated and is given in table 2.7.

(c)  $\nu_3$ ,  $\text{CH}_2$  deformation,  $1387\text{cm}^{-1}$

Inspection of the central region of the  $\nu_3$  fundamental of  $\text{H}_2\text{CCO}$ , shown in figure 2.5, reveals sharp individual  ${}^q\text{Q}_{K_a}$  branches which possess neither a regular degradation pattern nor the expected intensity alternation arising from the nuclear spin statistical weights. In addition, a very

Figure 2.4 Comparison of the Q branch structures in  $\nu_2$  fundamentals of  $\text{H}_2\text{CCO}$ ,  $\text{H}_2\text{C}^{13}\text{CO}$ ,  $\text{H}_2^{13}\text{CCO}$  and  $\text{D}_2\text{CCO}$ .

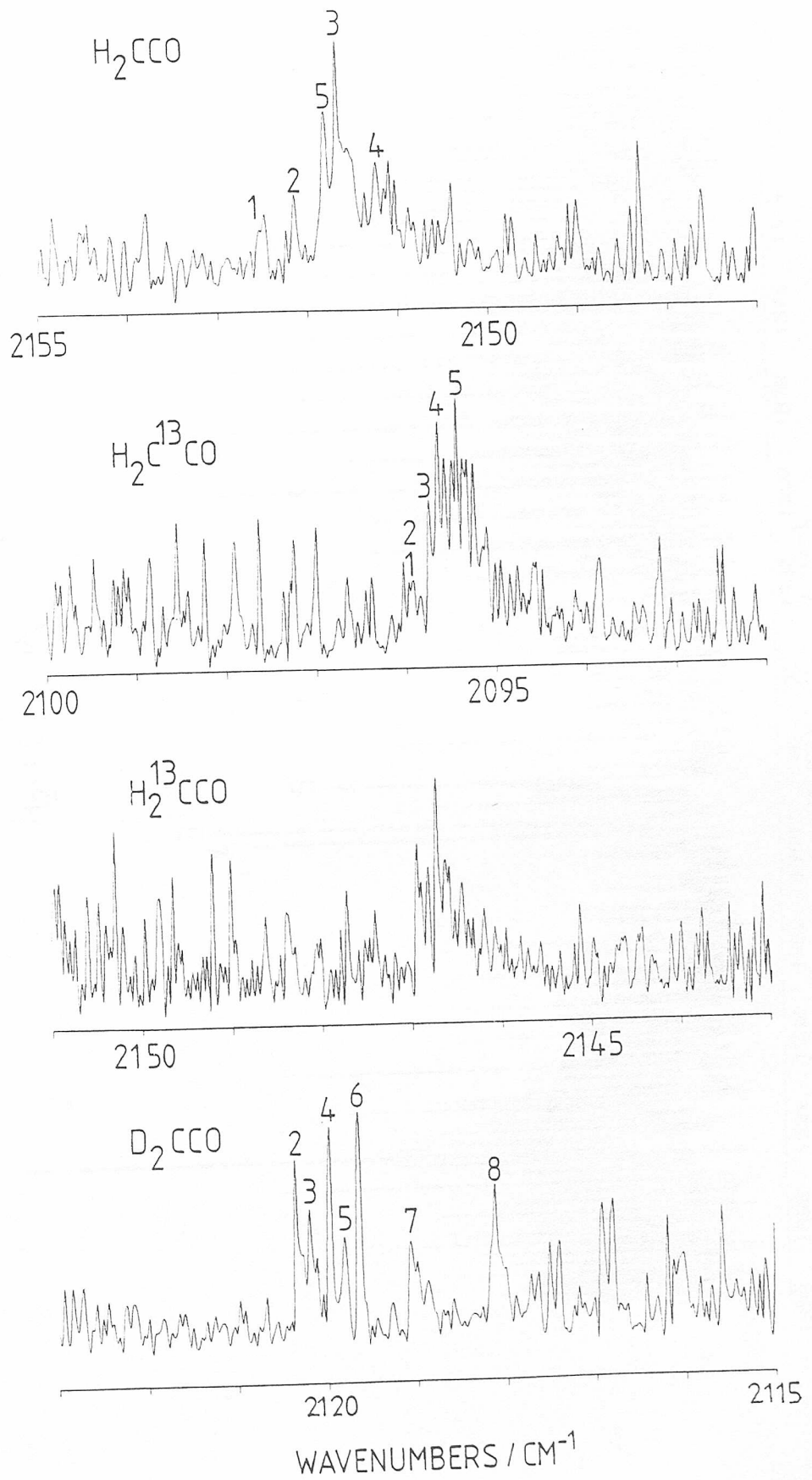
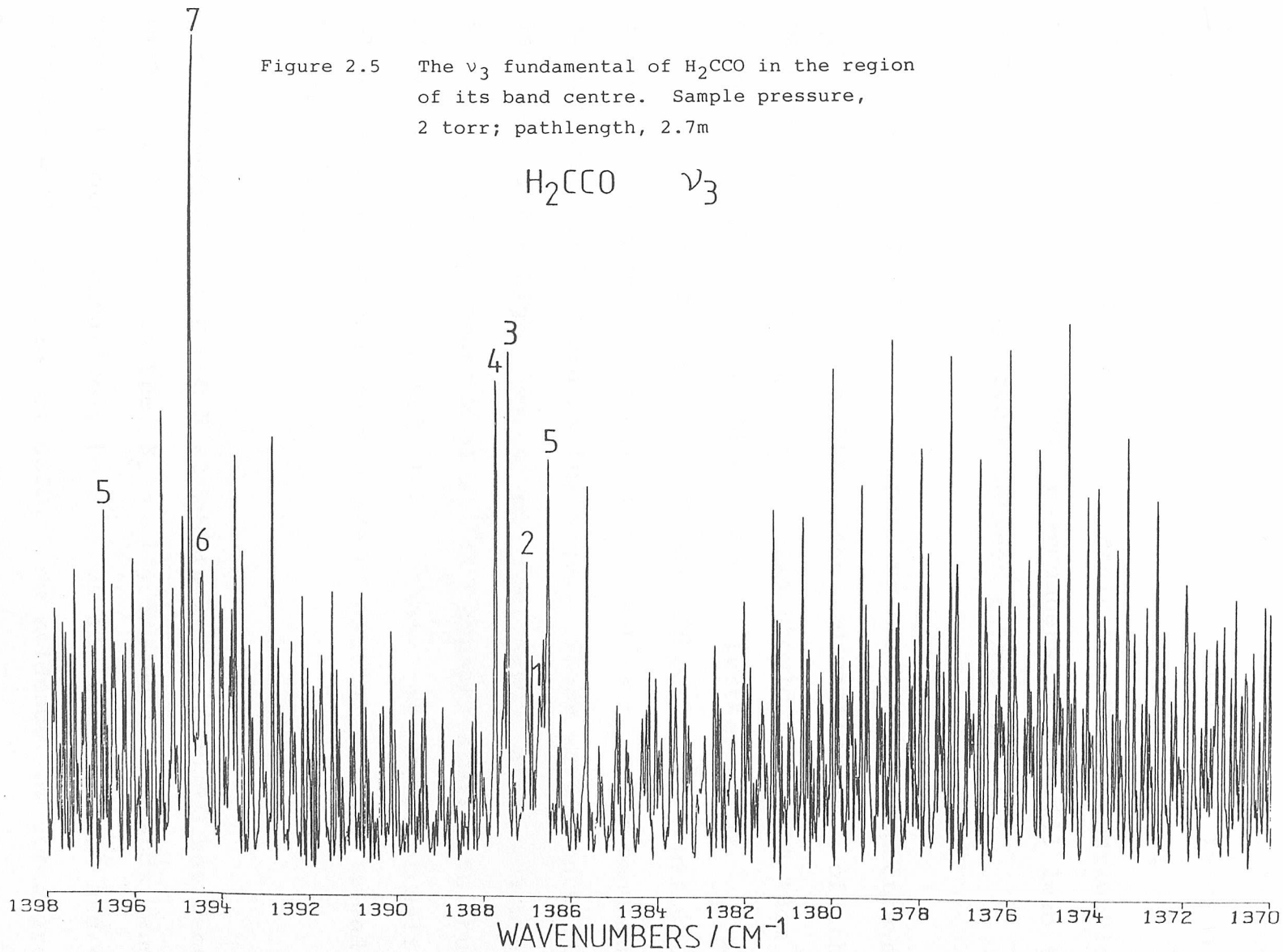


Figure 2.5 The  $\nu_3$  fundamental of  $\text{H}_2\text{CCO}$  in the region of its band centre. Sample pressure, 2 torr; pathlength, 2.7m

$\text{H}_2\text{CCO}$   $\nu_3$

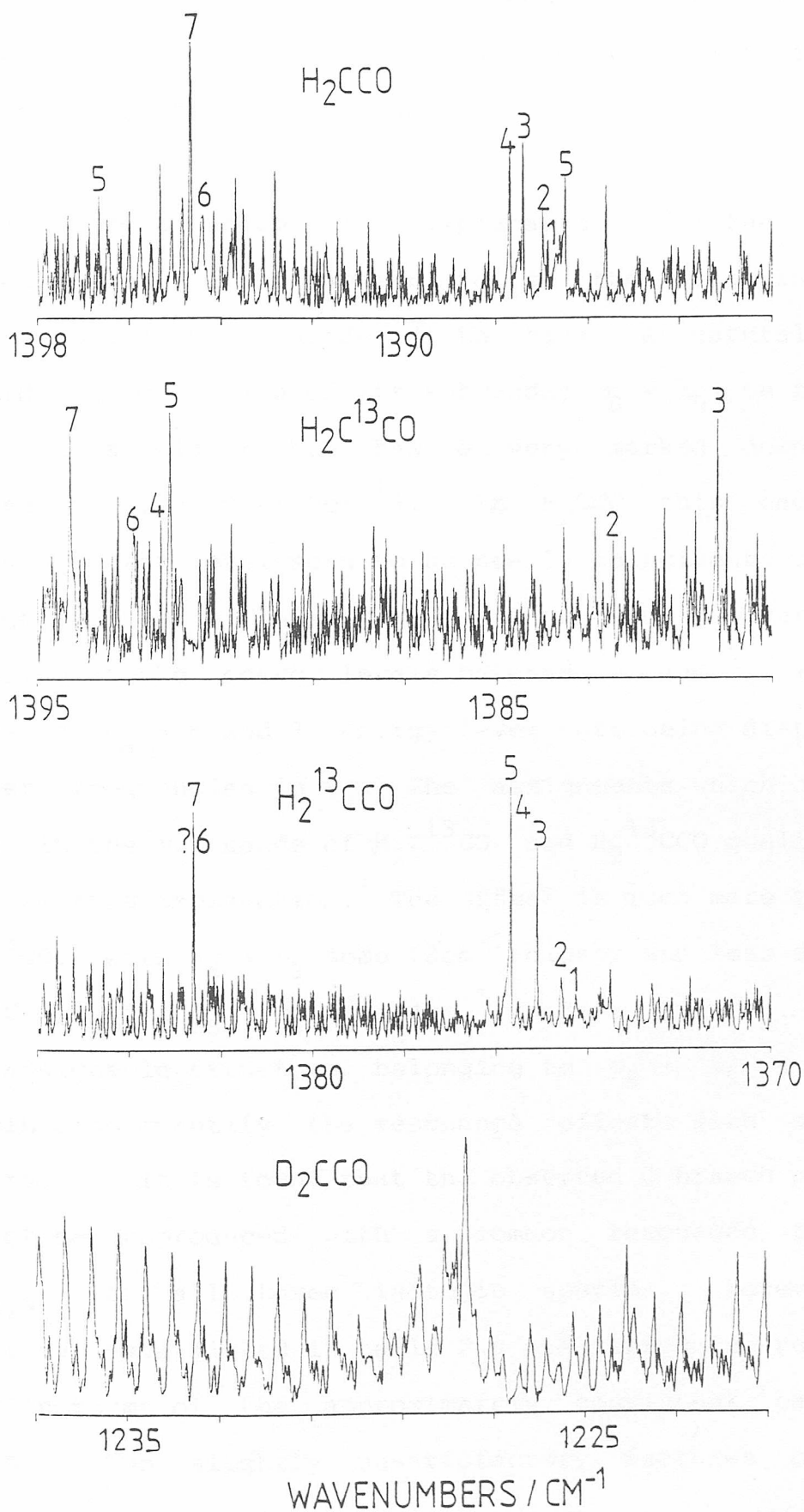


intense sharp absorption occurs some  $8\text{cm}^{-1}$  higher than the main Q branch structure. Clearly, the rotational energy levels of this vibration are subjected to significant perturbations, almost certainly through a Fermi resonance with  $\nu_8 + \nu_9$  ( $A_1$ ), which is calculated to lie at  $\sim 1417\text{cm}^{-1}$ . This vibration is expected to exhibit a strong degradation of its  $K_a$  structure to lower wavenumbers, which will lead to a crossing of energy levels between  $\nu_3$  and  $\nu_8 + \nu_9$ .

Examination of the corresponding bands in the spectra of  $\text{H}_2\text{C}^{13}\text{CO}$  and  $\text{H}_2^{13}\text{CCO}$  support the identification of the perturbing level as  $\nu_8 + \nu_9$ . This should lie about  $18\text{cm}^{-1}$  closer in  $\text{H}_2\text{C}^{13}\text{CO}$  but about  $4\text{cm}^{-1}$  further from  $\nu_3$  in  $\text{H}_2^{13}\text{CCO}$ . The spectrum of  $\text{H}_2\text{C}^{13}\text{CO}$  exhibits no obviously assignable Q branch degradation pattern, but rather contains highly displaced Q branch features. These were eventually assigned with a high degree of confidence after careful studies. The  $\nu_3$  spectrum of  $\text{H}_2^{13}\text{CCO}$  appears similar to, but somewhat less perturbed than, that of  $\text{H}_2\text{CCO}$  itself. Comparison of the central regions of all three bands is made in figure 2.6.

Assignment of P and R structure in  $\nu_3$  of  $\text{H}_2\text{CCO}$  has been made for  $J \leq 36$  in the  $K_a = 1^\pm, 3$  and 5 subbands, and somewhat more tentatively to  $J \leq 20$  in the  $K_a = 2^\pm$  and 4 subbands with the aid of GSCD. No evidence of structure belonging to  $K_a = 6$  could be found, but structure consistent with  $K_a = 7$  could be found associated with the  $1395\text{cm}^{-1}$  Q branch. Results of the analysis of these assignments are

Figure 2.6 Comparison of band centre regions of  $\nu_3$  fundamentals of  $\text{H}_2\text{CCO}$ ,  $\text{H}_2\text{C}^{13}\text{CO}$ ,  $\text{H}_2^{13}\text{CCO}$  and  $\text{D}_2\text{CCO}$ , with assignments to highly displaced subband Q branches.



given in table 2.8. These confirm the effects of a major resonance, causing different degrees of mixing of rotational levels for different  $K_a$  between the two vibrations concerned, which give rise to a large variation in the  $\Delta\bar{B}$  values for different subbands.

The most acceptable explanation of the observed structure in  $\nu_3$  would appear to be the following. The unperturbed  $\nu_3$  is considered to have a natural, small upward  $K_a$  degradation of its subbands;  $\nu_8 + \nu_9$ , on the other hand, lies higher but has a very marked downward  $K_a$  degradation ( $\Delta A \approx -1.0\text{cm}^{-1}$ ). In  $\text{H}_2\text{CCO}$  this causes the  $K_a = 5$  energy level sets to be nearly coincident, such that a high degree of mixing and displacement occurs. The crossing of the energy levels between  $\nu_3$  and  $\nu_8 + \nu_9$  then leads to  $K_a = 6$  and  $7$  energy level sets being displaced to higher frequencies in  $\nu_3$ . The assignments which have been made in the  $\nu_3$  bands of  $\text{H}_2\text{C}^{13}\text{CO}$  and  $\text{H}_2^{13}\text{CCO}$  qualitatively confirm this explanation. The effect is much more severe in  $\text{H}_2\text{C}^{13}\text{CO}$ , with  $\nu_8 + \nu_9$  some  $18\text{cm}^{-1}$  closer and less severe in  $\text{H}_2^{13}\text{CCO}$ , with  $\nu_8 + \nu_9$  some  $4\text{cm}^{-1}$  further, from  $\nu_3$ . Without any assignable structure belonging to  $\nu_8 + \nu_9$ , it is not possible to quantify the resonance effects with any great accuracy. It is found that the observed Q branch positions cannot be reproduced with a common resonance parameter  $W_{3,8,9}$  for all three isotopic species. However, the observed data listed in table 2.9 are reproduced remarkably well in terms of the approximately consistent parameters given. Two slightly unsatisfactory features of these

Table 2.8 Results of analysis of  $\nu_3$   
fundamental of  $\text{H}_2\text{CCO}$ ,  $\text{cm}^{-1}$ .

$K_a$	$\Delta\bar{B} \times 10^5$	$\nu_{Ka}^o$
1	-7.7(59) <sup>a</sup>	1386.71(1)
2	+1.4(13)	1387.010(2)
3	+4.3(1)	1387.433(1)
4	+10.4(3)	1387.725(2)
5	+63.5(4)	1386.499(3)
6	-	1394.40 <sup>b</sup>
7	-15.4(7)	1394.731(3)

<sup>a</sup> Obtained from upper state

$$B = 0.343692(59), \quad C = 0.330261(59) \text{ cm}^{-1}.$$

<sup>b</sup> Visual inspection value. See figure 2.5.

Table 2.9. Reproduction of observed Q branches in  $\nu_3$  of  $\text{H}_2\text{CCO}$ ,  $\text{H}_2\text{C}^{13}\text{CO}$  and  $\text{H}_2^{13}\text{CO}$  after correction for Fermi resonance perturbations with  $\nu_8 + \nu_9$ ,  $\text{cm}^{-1}$ .

$K_a$	$\text{H}_2\text{CCO}$		$\text{H}_2\text{C}^{13}\text{CO}$		$\text{H}_2^{13}\text{CO}$	
	OBS	O-C <sup>a</sup>	OBS	O-C <sup>a</sup>	OBS	O-C <sup>a</sup>
1	1386.71	0.0			1374.29	0.0
2	1387.01	-0.1	1382.51	0.2	1374.61	-0.1
3	1387.43	0.0	1380.24	-0.4	1375.15	-0.1
4	1387.72	0.0	1392.35	-0.1	1375.72	0.1
5	1386.50	0.0	1392.15	0.0	1375.72	0.1
6	1394.40	-0.2	1392.95	0.3	?1382.63	0.0
7	1394.74	-0.1	1394.30	0.2	1374.63	0.0
$\nu_3$	1387.5		1386.0		1375.1	
$\Delta(A_3 - \bar{B}_3)$	+0.14		+0.14		+0.13	
$\nu_8 + \nu_9$	1416		1398		1409	
$\Delta(A - \bar{B})$	-1.0		-1.0		-1.0	
$W_{3,8,9}$	5.0		7.0		5.2	

<sup>a</sup> Since the calculations are at best only approximate, comparison with the accurately observed Q branch features is made only to the first decimal place.

estimates are that  $W_{3,8,9}$  is required to take significantly different values of  $5.0\text{cm}^{-1}$  ( $\text{H}_2\text{CCO}$ ),  $7.0\text{cm}^{-1}$  ( $\text{H}_2\text{C}^{13}\text{CO}$ ), and  $5.2\text{cm}^{-1}$  ( $\text{H}_2^{13}\text{CCO}$ ), and that  $\nu_3$  ( $\text{H}_2\text{C}^{13}\text{CO}$ ) apparently lies  $\sim 1.5\text{cm}^{-1}$  lower than  $\nu_3$  ( $\text{H}_2\text{CCO}$ ), when an unperturbed isotopic shift close to zero would be expected. However, it is anticipated that this cannot be improved upon without further information. Part of the problem is almost certainly due to the assumption that for each isotope  $\nu_8 + \nu_9$  will degrade in a regular sense to lower frequencies, when it almost certainly will not, due to Coriolis effects on the subbands through resonances with  $\nu_5 + \nu_8$  and  $\nu_6 + \nu_8$ . Nevertheless, the fact that the main features observed in the three spectra depicted in figure 2.6 are well reproduced in terms of the sets of almost consistent parameters in table 2.9 tends to indicate that the explanation is basically correct.

For  $\text{D}_2\text{CCO}$ , the Q branch structure is compressed into a very small region of the spectrum around  $1227\text{cm}^{-1}$ , as can be seen in the bottom spectrum in figure 2.6. It appears that a natural degradation to higher frequencies is present, but spacings and intensities are irregular, rendering assignment almost impossible. The same Fermi resonance interaction with  $\nu_8 + \nu_9$  can occur in  $\text{D}_2\text{CCO}$  as in  $\text{H}_2\text{CCO}$  species, but here the vibration lies extremely close, with  $\nu_8 + \nu_9$  calculated to lie at  $\sim 1223\text{cm}^{-1}$ . The highly compressed subband structure in  $\nu_3$  is consistent with that expected to arise through Fermi resonance with a vibration lying slightly lower, and with a marked degradation to lower

frequencies. The perturbations to the subbands in  $\nu_3$  would then all be to higher frequency, but would diminish rapidly as  $K_a$  increases. If the natural subband degradation in  $\nu_3$  is small and upwards (as in  $H_2CCO$  species) this would give rise to the highly compressed and confused structure which is observed. The resonance parameter  $W_{3,8,9}$  will be smaller than that for  $H_2CCO$  species, so it is estimated that the unperturbed  $\nu_3$  vibration frequency will be some  $2 - 3\text{cm}^{-1}$  below the observed band centre, at ca.  $1225\text{cm}^{-1}$ .

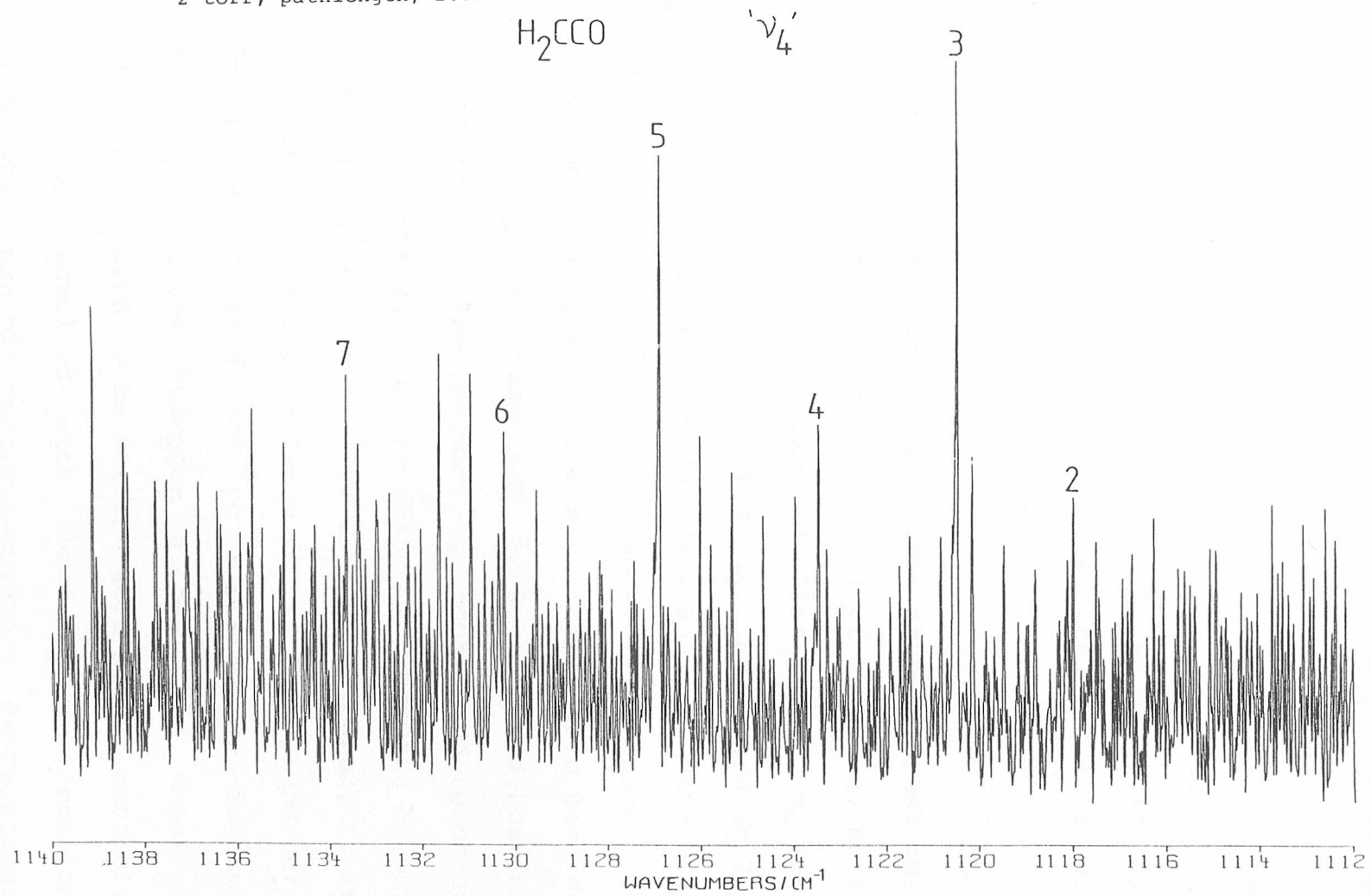
(d)  $\nu_4$ , CCO symmetric stretch,  $1116\text{cm}^{-1}$

This band is characterised by a distinctive Q branch degradation to higher frequency, as displayed in figure 2.7. Individual  ${}^qQ_{K_a}$  branches are sharp, and can be assigned readily.

Unambiguous assignments to over 200 transitions in the P and R branches have been made in terms of the GSCD. Assignments for  $J \leq 36$  in the  $K_a = 2^\pm, 3, 4, 5$  subbands were certain, but assignments to the asymmetry split  $K_a = 1^\pm$  series give indication of perturbations to both their expected absolute and relative positions. As in previous cases, severe overlapping and/or lack of intensity prevented assignment to  $K_a = 0$  and  $K_a \geq 6$  subband series.

Analysis of  $K_a \geq 3$  and  $K_a = 2$  (low J) subbands yield the results listed in table 2.10. No refinement to individual upper state B and C constants was possible since the  $K_a = 1^\pm$

Figure 2.7 The ' $\nu_4$  fundamental' of  $\text{H}_2\text{CCO}$  in the region of its band centre. Sample pressure, 2 torr; pathlength, 2.7m



energy levels are clearly perturbed, and insufficient  $K_a = 2^\pm$  assignments have been made. The subband  $\Delta\bar{B}$  values in table 2.10 for  $K_a = 2 - 5$  show reasonable consistency, but the subband origins give a poor fit to equation 2.1, and the parameters determined require that  $\Delta_K'$  has a magnitude of nearly 6 times that of the ground state value. Clearly, once again, quite severe resonance perturbations are present.

Of possible interacting levels, the three nearest ones are  $2\nu_5$ ,  $\nu_5 + \nu_6$ , and  $2\nu_6$  (all  $A_1$ ), all of which may be in Fermi resonance with  $\nu_4$ . Of these,  $2\nu_5$  lies higher,  $\nu_5 + \nu_6$  almost coincident, and  $2\nu_6$  lower than  $\nu_4$ . Structure in  $2\nu_5$  and  $2\nu_6$  can be assigned and preliminary analyses have been performed (see 2.4(e) and 2.4(f)). However, assignment to the closer lying  $\nu_5 + \nu_6$  vibration was not possible because of overlap with  $\nu_4$  structure and lack of evidence of assignable structure. The resonance is considered to occur between all four levels, from the evidence presented by our observations on  $\text{H}_2\text{C}^{13}\text{CO}$  and  $\text{H}_2^{13}\text{CCO}$  spectra. Indeed, it is difficult to rationalise such a large  $\Delta A$  value as found here with a vibration which would not be expected to involve major displacements of the hydrogen atoms. The observed degradation is considered to be attributable almost entirely to the resonances involved with three other vibration levels, two of which exhibit enormous upward  $K_a$  degradations due to the major Coriolis interactions which occur between  $\nu_5$ ,  $\nu_6$  and  $\nu_9$ .

Table 2.10. Results of analysis of  $\nu_4$   
fundamental of  $\text{H}_2\text{CCO}$ ,  $\text{cm}^{-1}$ .

$K_a$	$\Delta\bar{B} \times 10^4$	$\nu_{K_a}^o$
2	+2.87(14)	1118.000(2)
3	+3.43(2)	1120.466(1)
4	+3.28(4)	1123.449(2)
5	+2.94(3)	1126.879(2)
6	-	1130.363 <sup>a</sup>
7	-	1133.388 <sup>a</sup>
Average +3.13(30)		
$\nu^o$		1115.96(10)
$\Delta(A-\bar{B})$		+0.5296(173)
$(\Delta_{K'} - \Delta_{K''})$		+0.00373(58)
$\Delta A$		+0.5299(74)

<sup>a</sup> Observed positions of sharp Q branch maxima. See figure 2.7.

In table 2.11, the  ${}^qQ_{Ka}$  frequencies for the  $\nu_4$  fundamentals of  $\text{H}_2\text{CCO}$ ,  $\text{H}_2\text{C}^{13}\text{CO}$ ,  $\text{H}_2^{13}\text{CCO}$  and  $\text{D}_2\text{CCO}$  are listed, along with 'best estimate' parameters. These are only effective values, due to the major perturbations present, and the vibration frequencies cannot be accepted as those of the  $\nu_4$  fundamental. Force constant calculations (see chapter 3) predict  $^{13}\text{C}$  frequency shifts on  $\nu_4$  of  $< 1\text{cm}^{-1}$  for  $\text{H}_2\text{C}^{13}\text{CO}$  and  $\sim 16\text{cm}^{-1}$  for  $\text{H}_2^{13}\text{CCO}$ , which may be compared with 'experimental' values of  $7.9\text{cm}^{-1}$  and  $5.2\text{cm}^{-1}$  respectively! Comparison of the central regions of all four bands is made in figure 2.8.

Collected in table 2.12 are the data which have been obtained from careful Q branch assignment of the spectra of  $\nu_5$ ,  $\nu_6$ ,  $2\nu_5$ ,  $2\nu_6$ , and  $\nu_4$  for  $\text{H}_2\text{CCO}$ ,  $\text{H}_2\text{C}^{13}\text{CO}$  and  $\text{H}_2^{13}\text{CCO}$ . The values for the levels in the  $1100\text{cm}^{-1}$  in the region are compared with the values expected using a simple harmonic oscillator approach, where the isotopic shift on an overtone, or combination level is simply twice, or the sum of the shift(s) on the constituent fundamental(s). It will be seen that almost all observations are at complete variance with expectation. The observed data on  $\nu_5$  and  $\nu_6$  should be accurate and reliable, since the vibrations are at low energy and suffer minimal vibrational resonance perturbations; the major rotational resonance perturbations to  $\nu_5$  and  $\nu_6$  do not affect their vibrational frequencies. Thus the anticipated isotopic shifts on  $2\nu_5$ ,  $2\nu_6$  and  $\nu_5 + \nu_6$  should be quite reliable, and it is concluded from the evidence in table 2.12 that all four vibrations in the

Table 2.11. Subband analyses for  $\nu_4$  fundamental  
of isotopic ketenes,  $\text{cm}^{-1}$ .

$K_a$	$\text{H}_2\text{CCO}$		$\text{H}_2\text{C}^{13}\text{CO}$		$\text{H}_2^{13}\text{CCO}$		$\text{D}_2\text{CCO}$	
	OBS	O - C	OBS	O - C	OBS	O - C	OBS	O - C
2	(1118.004) <sup>a</sup>	-	(1108.272)	-	(1112.002)	-	925.122	-0.027
3	(1120.485)	-	(1112.066)	-	1114.734	-0.007	925.561	0.036
4	1123.473	0.001	1115.432	0.003	1117.285	0.017	925.968	0.015
5	1126.905	-0.002	1118.972	-0.008	1119.811	-0.015	926.301	-0.037
6	1130.363	0.001	1122.774	0.006	1121.902	0.004	926.567	0.013
7	1133.388	-0.001	1126.455	-0.002	(1124.556)	-	-	-
$\nu^0$	1116.013(12)		1108.108(46)		1110.804(68)		924.737(43)	
$\Delta(A-\bar{B})$	+0.52030(78)		+0.4979(31)		+0.4805(70)		+0.1049(72)	
$(\Delta_K' - \Delta_K'')$	+0.003382(12)		+0.00252(50)		+0.00478(15)		+0.00170(24)	

<sup>a</sup> Data in parentheses were not used in least squares fit.

All data refer to observed subband Q branch maxima.

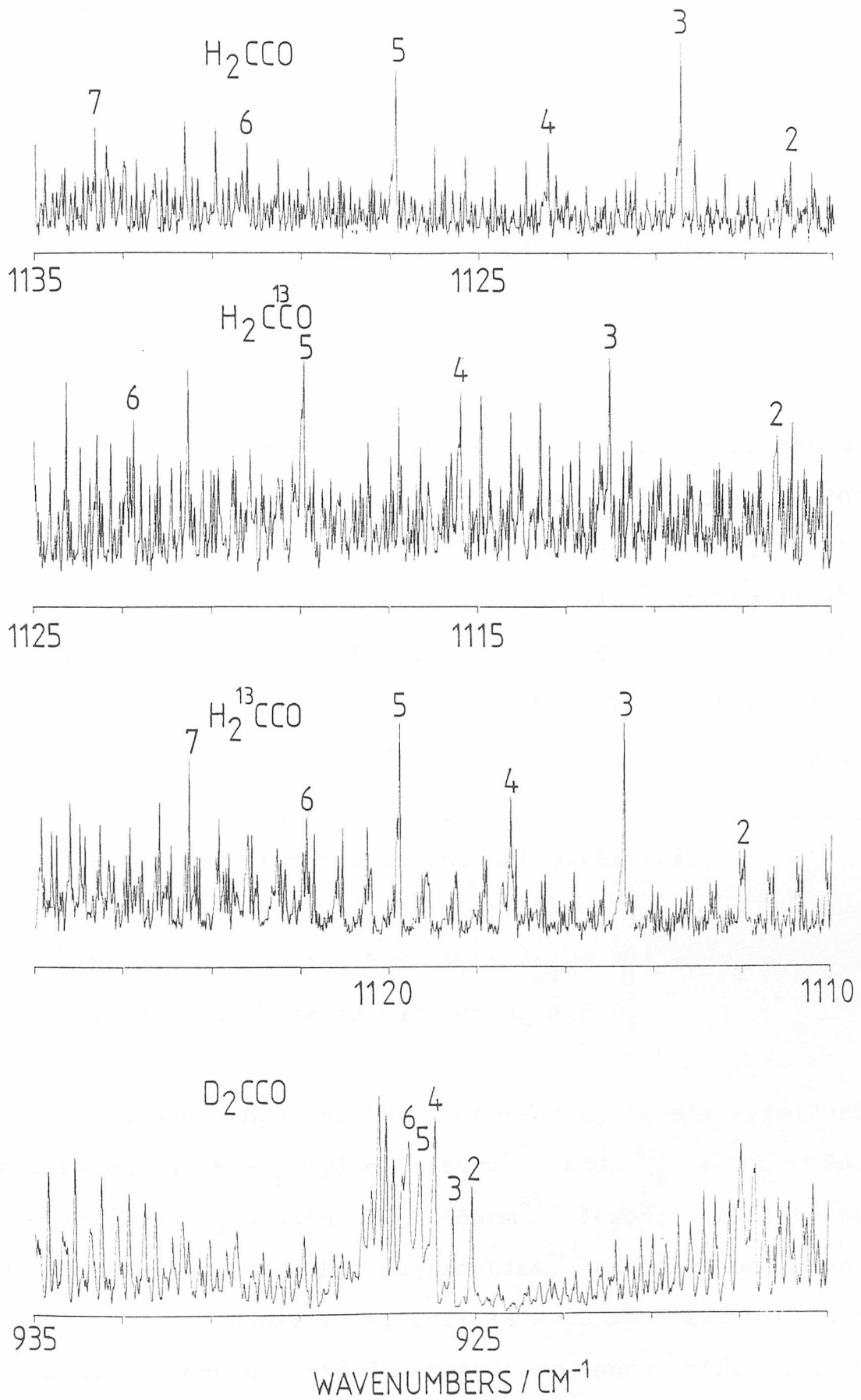


Figure 2.8 Comparison of band centre regions of ' $\nu_4$  fundamentals' of  $\text{H}_2\text{CCO}$ ,  $\text{H}_2\text{C}^{13}\text{CO}$ ,  $\text{H}_2^{13}\text{CCO}$  and  $\text{D}_2\text{CCO}$ , with assignments to subband Q branches.

1100cm<sup>-1</sup> region of ketene are in Fermi resonance.

Table 2.12. Vibrational data for  $\nu_4$ ,  $\nu_5$ ,  $\nu_6$ ,  $2\nu_5$ ,  $2\nu_6$ , and  $\nu_5 + \nu_6$  in isotopic ketenes, cm<sup>-1</sup>.

	H <sub>2</sub> CCO		H <sub>2</sub> C <sup>13</sup> CO		H <sub>2</sub> <sup>13</sup> CCO	
	OBS	PRED	OBS	PRED	OBS	PRED
$\nu_5$	587.3	-	5.40	5.34 <sup>a</sup>	0.37	0.40 <sup>a</sup>
$\nu_6$	528.4	-	9.68	9.73 <sup>a</sup>	5.52	5.75 <sup>a</sup>
$2\nu_6$	1065.1	1056.8	8.6	19.4 <sup>b</sup>	11.09	11.1 <sup>b</sup>
$\nu_5 + \nu_6$	-	1115.7	-	15.1	-	5.9 <sup>b</sup>
$\nu_4$	1116.0	-	7.9	0.8 <sup>a</sup>	5.2	15.9 <sup>a</sup>
$2\nu_5$	1187.5	1174.6	10.2	10.8	5.3	0.8 <sup>b</sup>

<sup>a</sup> Predicted from force constant estimates.

See table 3.17.

<sup>b</sup> Assuming  $(2\nu_i) = 2 \times \nu_i$ ,  $(\nu_i + \nu_j) = \nu_i + \nu_j$ , using the observed data on  $\nu_5$  and  $\nu_6$ .

In dideuteroketene the interacting levels are further separated, with  $2\nu_5$  lying  $\sim 160\text{cm}^{-1}$  and  $\nu_5 + \nu_6 \sim 50\text{cm}^{-1}$  higher than  $\nu_4$ , with  $2\nu_6 \sim 55\text{cm}^{-1}$  lower. Whilst still exhibiting an upward  $K_a$  degradation, as can be seen in figure 2.8 and table 2.11, this is much less extreme than in ketene, reflecting the decreased resonance effects in this case. The  $\nu_4$  band is rather weak and badly overlapped by structure belonging to  $\nu_8$  and  $2\nu_6$ .

(e)  $2\nu_5$ , CCO deformation overtone,  $1189\text{cm}^{-1}$

Preliminary studies of the first overtone of  $\nu_5$ , located  $\sim 70\text{cm}^{-1}$  above  $\nu_4$  indicate that it consists of sharp, clearly defined Q branches which degrade dramatically to higher frequencies, spanning some  $110\text{cm}^{-1}$ . Similar spreads are observed in the  $\text{H}_2\text{C}^{13}\text{CO}$  and  $\text{H}_2^{13}\text{CCO}$  spectra. In the  $\nu_4$  analysis, Fermi resonance interactions between  $\nu_4$ ,  $2\nu_5$ ,  $2\nu_6$  and  $\nu_5 + \nu_6$  levels were found to have significant effects on  $\nu_4$ . The same interactions were thus anticipated to have significant effects on  $2\nu_5$ .

The sharp individual Q branches were taken to be good approximations to the subband origins and were analysed in terms of equation 2.1 for all three hydrogenated ketenes. These are listed, together with the derived parameters in table 2.13. The fits to individual subbands are found to be poor and are almost certainly caused by the Fermi resonance interactions. A study of the vibrational levels in this region of the spectrum indicates that the large calculated  $\Delta(A - \bar{B})$  values of table 2.13 are almost entirely attributable to the major a-axis Coriolis interactions with  $\nu_5 + \nu_8$  and  $\nu_5 + \nu_9$ .

Since the  $\nu_5 + \nu_6$  combination could not be located in any of the spectra, the  $\nu_4/2\nu_5/2\nu_6/\nu_5 + \nu_6$  Fermi resonance could not be solved. However, a qualitative measure of the relative extents of perturbation to  $2\nu_5$  in the  $\text{H}_2\text{CCO}$ ,  $\text{H}_2\text{C}^{13}\text{CO}$  and  $\text{H}_2^{13}\text{CCO}$  spectra can be obtained, in the first

Table 2.13. Approximate subband analyses of  $2\nu_5$  of isotopic ketenes,  $\text{cm}^{-1}$ .

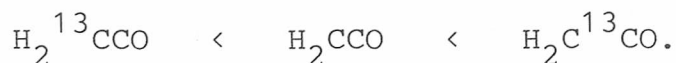
$K_a$	$\text{H}_2\text{CCO}$		$\text{H}_2\text{C}^{13}\text{CO}$		$\text{H}_2^{13}\text{CCO}$	
	OBS	O-C	OBS	O-C	OBS	O-C
2	1196.3	0.5	1185.6	1.0	1191.4	0.1
3	1205.7	-0.3	1193.1	-0.5	1202.1	-0.1
4	1219.4	-0.5	1205.1	-0.9	1217.0	0.1
5	1236.9	0.0	1221.4	-0.3	1235.3 <sup>a</sup>	0.1
6	1257.0	0.2	1241.1	0.5	1255.9	0.1
7	1278.9	0.2	1262.9	0.7	1278.0	-0.1
8	1302.0	-0.2	1286.1	-0.4	1301.2	0.0
9			(1310.1) <sup>b</sup>		(1324.6) <sup>b</sup>	
$\nu^{\text{O}}$	1187.5(4)		1177.3(9)		1182.1(1)	
$\Delta(\text{A}-\bar{\text{B}})$	+2.092(30)		+1.818(65)		+2.282(11)	
$(\Delta_{\text{K}}' - \Delta_{\text{K}}'')$	+0.00470(44)		+0.00174(94)		+0.00663(15)	

<sup>a</sup> Uncharacteristic absorption pattern. Possibly caused by a localized c-axis Coriolis interaction with  $K_a = 6$  level of  $3\nu_9$ .

<sup>b</sup> Broad and weak absorption feature which were not used in least squares fit.

All data refer to observed Q branch maxima.

instance by comparison of the the standard deviations associated with the subband analyses in table 2.13. A second estimation can be deduced from the discrepancies between the twice-fundamental frequencies and observed (perturbed) band centres of  $2\nu_5$  (see table 2.12). For all three isotopomers,  $2\nu_5$  is found to absorb at frequencies appreciably above those calculated from the fundamentals. This may be caused by the Fermi resonance interactions but may also be partly attributable to a negative anharmonicity factor. These investigations tend to indicate that the degree of interaction of  $2\nu_5$  with the  $\nu_4/2\nu_6/\nu_5 + \nu_6$  system is such that it follows the order



(f)  $2\nu_6$ ,  $\text{CH}_2$  wagging overtone,  $1060\text{cm}^{-1}$

The first overtone of  $\nu_6$  is located some  $50\text{cm}^{-1}$  below  $\nu_4$ . Individual Q branch absorptions were found to be sharp, and markedly degraded to lower frequencies. Similar degradation patterns are also evident in the  $\text{H}_2\text{C}^{13}\text{CO}$  and  $\text{H}_2^{13}\text{CCO}$  spectra. The large  $K_a$  degradation is largely attributable to a-axis Coriolis interactions with  $\nu_6 + \nu_8$  and  $\nu_6 + \nu_9$ . The unresolved Fermi resonance interactions between  $\nu_4$ ,  $2\nu_5$ ,  $2\nu_6$  and  $\nu_5 + \nu_6$  previously reported for  $\nu_4$  and  $2\nu_5$ , were expected to also affect the  $2\nu_6$  level appreciably. If this is so, then since  $2\nu_6$  lies below these interacting levels, it would be expected to be displaced to lower frequencies.

As before, absorption peak maxima were taken to be good approximations to the subband origins and were analysed in terms of equation 2.1. These subband origins, together with the derived parameters are listed in table 2.14. The fit of subband centres was predictably found to be poor for all isotopomers, particularly for the  $\text{H}_2\text{C}^{13}\text{CO}$ . This is almost certainly due to the anticipated Fermi resonance interactions.

The observed band centres for all three isotopomers are compared with those calculated by simple harmonic estimates based on the well defined fundamental origins in table 2.12. Discrepancies between the observed and calculated band centres are found to be smallest for  $\text{H}_2\text{C}^{13}\text{CO}$ . Surprisingly, however,  $2\nu_6$  in all three isotopomeric species is observed at frequencies above those predicted despite possible Fermi resonance interactions with levels at higher frequencies. This may be indicative of an appreciable negative anharmonicity factor associated with the overtone. For the corresponding vibrational displacements found in the  $2\nu_5$  studies (see section 2.4(e)), it was not possible to establish whether these were attributable to negative anharmonicity or Fermi resonance, but for  $2\nu_6$  the former seems to predominate. Indeed, Moore and Pimentel (52) rationalised negative anharmonicity for the out of plane vibrations,  $\nu_5$  and  $\nu_6$  (as well as for  $\nu_9$ ), in terms of a steep potential function arising from negative quartic contributions.

Table 2.14. Subband analyses of  $2\nu_6$  of isotopic ketenes,  $\text{cm}^{-1}$ .

$K_a$	$\text{H}_2\text{CCO}$		$\text{H}_2\text{C}^{13}\text{CO}$		$\text{H}_2^{13}\text{CCO}$	
	OBS	O-C	OBS	O-C	OBS	O-C
2	(1061.0) <sup>a</sup>		(1048.0)		(150.3)	
3	(1058.0)		(1047.8)		(1047.0)	
4	1053.3	0.002	1045.9	0.047	1042.1	-0.011
5	1046.7	-0.005	1039.8	-0.118	1035.5	0.027
6	1038.7	0.004	1032.8	0.098	1027.4	-0.022
7	1029.3	-0.001	1024.2	-0.027	1018.0	0.006
$\nu^0$	1065.11(3)		1056.47(66)		1054.02(15)	
$\Delta(\bar{A}-\bar{B})$	-0.7418(18)		-0.666(45)		-0.749(10)	
$(\Delta_{K'} - \Delta_{K''})$	+0.000225(23)		+0.00017(68)		+0.000278(15)	

<sup>a</sup> Data in parentheses may be subject to appreciable Fermi resonance displacement and were thus excluded from least squares fit. All data refer to observed subband Q branch maxima.

(g)  $2\nu_8$ ,  $\text{CH}_2$  rocking overtone,  $1952\text{cm}^{-1}$

Structure belonging to this overtone of  $\nu_8$  is readily observed in the spectra, lying below the extremely intense  $\nu_2$  fundamental. The subband Q branches are sharply defined features, degrading rapidly to higher frequency as a result of major a-axis Coriolis interactions with the lower lying  $A_2$  levels,  $\nu_5 + \nu_8$  and  $\nu_6 + \nu_8$ . This causes  ${}^qQ_2$  through  ${}^qQ_9$  to span some  $80\text{cm}^{-1}$  of the spectrum in all three  $\text{H}_2\text{CCO}$  species studied. The observed  ${}^qQ_{K_a}$  peak maxima, taken to be good approximations to the subband origins of  $2\nu_8$  in  $\text{H}_2\text{CCO}$ ,  $\text{H}_2\text{C}^{13}\text{CO}$  and  $\text{H}_2^{13}\text{CCO}$ , are listed in table 2.15, with parameters determined from them. In this case, an almost perfect fit in terms of equation 2.1 can be achieved over  $K_a = 2 - 7$  in all three bands, with only slight misfits to  ${}^qQ_8$  and  ${}^qQ_9$  within the uncertainties in the parameters.

The apparent very large changes in  $\Delta(A - \bar{B})$  and  $\Delta_K$  for each isotopomer do not derive directly from the vibration concerned. Rather, they are numerical parameters required to account for the effects of the Coriolis resonances which are of sufficient magnitude to fall barely within a strictly second-order perturbation treatment, upon which the physical validity of equation 2.1 depends. Nevertheless, the ability to fit accurately the subband origins of  $2\nu_8$  means that this level would seem to be almost vibrationally unperturbed in all three hydrogenated ketene species studies. The slight misfits to  ${}^qQ_8$  and  ${}^qQ_9$  frequencies may derive from the Coriolis interactions mentioned above, or from the effects

Table 2.15. Subband analyses for  $2\nu_8$  overtone of ketenes,  $\text{cm}^{-1}$ .

$K_a$	$\text{H}_2\text{CCO}$		$\text{H}_2\text{C}^{13}\text{CO}$		$\text{H}_2^{13}\text{CCO}$	
	OBS	O-C	OBS	O-C	OBS	O-C
2	1957.07	-0.01	1935.75	-0.01	1941.50	0.00
3	1962.92	0.00	1941.50	0.01	1947.38	0.00
4	1970.97	0.01	1949.40	0.01	1955.50	0.00
5	1981.07	0.00	1959.31	-0.01	1965.68	-0.02
6	1993.08	-0.01	1971.13	0.00	1977.83	0.02
7	2006.82	0.01	1984.59	0.00	1991.63	-0.01
8	(2022.18) <sup>a</sup>	-	(1999.67)	-	(2007.19)	-
9	(2038.88)	-	(2015.58)	-	(2024.01)	-
$\nu^0$	1952.353(14)		1931.118(12)		1936.727(17)	
$\Delta(A-\bar{B})$	+1.1876(14)		+1.1667(11)		+1.1985(16)	
$(\Delta_{K'} - \Delta_{K''})$	+0.001553(25)		+0.001537(21)		+0.001591(30)	

<sup>a</sup> Data in parentheses were not used in least squares fit but are essentially reproduced within the uncertainties in the determined parameters.

of Fermi resonance with  $\nu_2$ , which is suspected from the study of the  $\nu_2$  bands described in 2.4(b).

(h)  $\nu_7$ ,  $\text{CH}_2$  asymmetric stretch,  $3165\text{cm}^{-1}$

The  $\nu_7$   $\text{CH}_2$  asymmetric stretching vibration has previously been analysed, together with microwave data, by Johns et al. (55) in order to determine the ground state rotational constants of table 2.1. These authors pointed out however, that the upper state parameters were perturbed most probably through a Fermi resonance with the  $\nu_2 + \nu_8$  level which lies some  $45\text{cm}^{-1}$  below. An indication of the extent of interaction can be gained by comparison of the ground and upper state  $\Delta_K$  constants in table (iv) of their paper, where it is found that the upper state value is 12 times the magnitude of that of the ground state. This is a common feature of Fermi resonance perturbations of ketene vibrations (see sections 2.4(d) and 2.4(e), for example).

In the present study, the  $\text{H}_2\text{CCO}$  spectrum of  $\nu_7$  at rather lower resolution ( $\approx 0.05\text{cm}^{-1}$ ) than that available to the above authors, was compared with the same vibration in the  $\text{H}_2\text{C}^{13}\text{CO}$  and  $\text{H}_2^{13}\text{CCO}$  spectra by simple contour shift method. The  $\nu_2 + \nu_8$  bands was also examined in the same way in the  $\text{H}_2\text{CCO}$  and  $\text{H}_2^{13}\text{CCO}$  spectra. However, because of the large isotopic shift to  $\nu_2$ , the  $\nu_2 + \nu_8$  combination could not be located in the  $\text{H}_2\text{C}^{13}\text{CO}$  spectrum because of overlap with  $\nu_1$ .

The assigned  ${}^r Q_{Ka}$  and  ${}^p Q_{Ka}$  frequencies for  $\nu_7$  and

$\nu_2 + \nu_8$  are listed in table 2.16, whilst the observed  $^{13}\text{C}$  shifts are given, together with force field predicted (unperturbed)  $\nu_7$  shifts and simple harmonic  $\nu_2 + \nu_8$  shifts in table 2.17. The observed  $\Delta\nu_7(\text{H}_2^{13}\text{CCO})$  shift of  $13.6\text{cm}^{-1}$  compares favourably with its predicted value of  $\sim 12.7\text{cm}^{-1}$ . The numerical similarity between these can be accounted for in terms of an almost identical observed shift to  $\nu_2 + \nu_8$  in the same spectrum, which would result in virtually the same degree of interaction between  $\nu_7$  and  $\nu_2 + \nu_8$  in both the  $\text{H}_2\text{CCO}$  and  $\text{H}_2^{13}\text{CCO}$  spectra. The same force field calculations predict an unperturbed  $\Delta\nu_7(\text{H}_2\text{C}^{13}\text{CO})$  shift of  $\sim 0.0\text{cm}^{-1}$ , which seems reasonable since the vibration should involve virtually no motion of the isotopically substituted carbon. However, the observed shift is  $4.1\text{cm}^{-1}$ . The discrepancy is almost certainly due to the diminished effects of Fermi resonance with  $\nu_2 + \nu_8$  in  $\text{H}_2\text{C}^{13}\text{CO}$  on account of the shift of  $56.2\text{cm}^{-1}$  suffered by  $\nu_2$ .

If it is assumed that there are no other vibrational resonances involved, then the Fermi resonance perturbation of  $\nu_7$  by  $\nu_2 + \nu_8$  may be corrected for in terms of equation 1.10. This is restated below in terms of parameters relating to the present investigations:

$$\begin{aligned}
 E_7^{\text{O}}(\text{pert}) &= 1/2 \{E_7^{\text{O}}(\text{unp}) + E_{28}^{\text{O}}(\text{unp})\} \\
 &+ 1/2 ([d_0]^2 + 4[W_{7,2,8}]^2)^{1/2}
 \end{aligned}
 \tag{2.2}$$

and

Table 2.16.  $r_{Q_{Ka}}$  and  $p_{Q_{Ka}}$  assignments for  $\nu_7$  and  $\nu_2 + \nu_8$ ,  $\text{cm}^{-1}$ .

	$\text{H}_2\text{CCO}$		$\text{H}_2\text{C}^{13}\text{CO}$		$\text{H}_2^{13}\text{CCO}$	
	$\nu_7$	$\nu_2 + \nu_8$	$\nu_7$	$\nu_2 + \nu_8$	$\nu_7$	$\nu_2 + \nu_8$
$r_{Q_5}$		3227.8				3215.6
$r_{Q_4}$		3210.3				3196.7
$r_{Q_3}$	3227.21	2190.4	3222.72		3214.20	3175.0
$r_{Q_2}$	3210.57		3205.0		3196.7	
$r_{Q_1}$	3192.90	3148.9	3188.0		3178.80	
$r_{Q_0}$	3174.20	3129.9	3170.05		3160.70	3115.9
$p_{Q_1}$	3156.20	3110.9	3152.20		3142.50	
$p_{Q_2}$	3138 <sup>a</sup>		3134 <sup>a</sup>		3123.5 <sup>a</sup>	
$p_{Q_3}$	3199.75		3115.25		3106.20	
$p_{Q_4}$	3101.8		3096.36			
$p_{Q_5}$			3078.0			

<sup>a</sup> Tentative assignment.

Table 2.17. Frequencies and  $^{13}\text{C}$  frequency shifts for  $\nu_7$  and  $\nu_2 + \nu_8$ ,  $\text{cm}^{-1}$ .

	$\text{H}_2\text{CCO}$	$\text{H}_2\text{C}^{13}\text{CO}$	$\text{H}_2^{13}\text{CCO}$
$\nu_7$ (OBS)	3165.299 <sup>a</sup>	4.1	13.6
$\nu_7$ (CALC <sup>b</sup> )	-	0.0	12.7
$\nu_2 + \nu_8$ (OBS)	3120.095 <sup>a</sup>	-	14.0
$\nu_2 + \nu_8$ (CALC <sup>c</sup> )	3130.3	66.9	13.3

<sup>a</sup> Johns et al. (55).

<sup>b</sup> Predicted from force field studies. See chapter 3.

<sup>c</sup> See footnote <sup>b</sup> of table 2.12.

$$E_{28}^{\circ}(\text{pert}) = 1/2 \{E_7^{\circ}(\text{unp}) + E_{28}^{\circ}(\text{unp})\} - 1/2 ([d_0]^2 + 4[W_{7,2,8}]^2)^{1/2} \quad 2.3$$

where  $d_0 = (E_7^{\circ}(\text{unp}) - E_{28}^{\circ}(\text{unp}))$ ,  $W_{7,2,8}$  is an interaction parameter, and pert and unp represent perturbed and unperturbed respectively.

Clearly the first term on the right hand side of equations 2.2 and 2.3 are equivalent to the average of the perturbed energies, i.e.

$$1/2 (E_7^{\circ}(\text{unp}) + E_{28}^{\circ}(\text{unp})) = 1/2 (E_7^{\circ}(\text{pert}) + E_{28}^{\circ}(\text{pert})) \quad 2.4$$

Equations 2.2 and 2.3 can be solved for by an iterative procedure such that the observed frequencies are reproduced in terms of unperturbed separations  $d_0$  and isotopically related values of  $W_{7,2,8}$ , such that

$$W_{7,2,8}^* = (\nu_7^* \cdot \nu_2^* \cdot \nu_8^* / \nu_7 \cdot \nu_2 \cdot \nu_8)^{1/2} \cdot W_{7,2,8} \quad 2.5$$

The results of this analysis are given in table 2.18. It should be noted that despite changes to the Fermi resonance corrected values of the frequencies, the shift on  $\nu_7$  in the  $\text{H}_2^{13}\text{CCO}$  spectrum remains the same as it was prior to the perturbation analysis. However, from the analysis an estimated shift of  $66.9\text{cm}^{-1}$  for  $\nu_2 + \nu_8$  in the  $\text{H}_2\text{C}^{13}\text{CO}$  spectrum was determined, which agrees exactly with that determined from the sum of the shifts to the constituent

fundamentals. This large shift places the combination close to  $\nu_1$  in the  $\text{H}_2\text{C}^{13}\text{CO}$  spectrum and may result in contributions to some of the perturbation effects observed in  $\nu_1$  discussed in section 2.4.1. An anharmonicity constant  $x_{28} = -3.6(1)\text{cm}^{-1}$  for  $\nu_2 + \nu_8$  was also estimated from the analysis for all isotopomers.

Table 2.18. Unperturbed frequencies and  $^{13}\text{C}$  frequency shifts for  $\nu_7$  and  $\nu_2 + \nu_8$ ,  $\text{cm}^{-1}$ .

	$\text{H}_2\text{CCO}$	$\text{H}_2\text{C}^{13}\text{CO}$	$\text{H}_2^{13}\text{CCO}$
$\nu_7$ (UNP)	3158.7	0.0 <sup>a</sup>	13.6
$\nu_2 + \nu_8$ (UNP)	3126.7	66.9	13.4
$w_{7,2,8}$	15.990	15.685	15.872

<sup>a</sup> Constraint imposed in perturbation analysis.

(i)  $\nu_8$ ,  $\text{CH}_2$  rock,  $978\text{cm}^{-1}$

In his examination of the B-type  $\text{CH}_2$  rocking vibration, Nemes (54) reported significant a-axis Coriolis interactions between  $\nu_8$  and the lower lying  $\nu_5$  and  $\nu_6$  vibrations. The net effect of these interactions is a large degradation of the band to higher frequency, caused by a-axis Coriolis contributions to the upper state A constant. This is accompanied by a marked intensity perturbation which renders the  $r_{\text{Q}_{\text{Ka}}}$  absorptions very weak. In the present studies, the  $\nu_8$  in  $\text{H}_2\text{CCO}$ ,  $\text{H}_2\text{C}^{13}\text{CO}$  and  $\text{H}_2^{13}\text{CCO}$  have been examined to

determine  $^{13}\text{C}$  frequency shifts.

As indicated in section 2.3, the shifts were obtained by comparison of the contours of the  $^r\text{Q}_{\text{Ka}}$  and  $^p\text{Q}_{\text{Ka}}$  absorptions and the wavenumbers of these, together with individual subband shifts are given in table 2.19. The assignment to the asymmetric  $^r\text{Q}_0$  feature in the  $\text{H}_2\text{CCO}$  spectrum was somewhat tentative mainly because of low intensities, but was, nevertheless believed to be accurate to within  $\pm 0.1\text{cm}^{-1}$ . Estimation of accurate  $^{13}\text{C}$  frequency shifts is not simple due to differing perturbation of the  $^p\text{Q}_1$  branches. The structure of the  $\text{H}_2\text{CCO}$ ,  $\text{H}_2\text{C}^{13}\text{CO}$  and  $\text{H}_2^{13}\text{CCO}$  asymmetric  $^p\text{Q}_1$  absorptions are significantly different from each other and are shown in figure 2.9. In the  $\text{H}_2\text{CCO}$  spectrum, some of the absorption corresponding to higher J transitions seem to be pushed to higher wavenumbers whilst the  $^p\text{Q}_1$  absorptions in the  $\text{H}_2^{13}\text{CCO}$  spectrum appear to suffer an intensity perturbation affecting lower J transitions. In addition, an anomalous sharp absorption at  $960.8\text{cm}^{-1}$  in the  $\text{H}_2^{13}\text{CCO}$  spectrum cannot readily be assigned in terms of the structure of  $\nu_8$ . In contrast, the  $\text{H}_2\text{C}^{13}\text{CO}$   $^p\text{Q}_1$  absorption exhibits no apparent evidence of perturbation and follow a regular degradation pattern.

These differences in the  $^p\text{Q}_1$  contours are almost certainly attributable to a localised interaction with the infrared inactive combination vibration  $\nu_6 + \nu_9$ , which is predicted from force field studies (of chapter 3) to lie  $10.4\text{cm}^{-1}$ ,  $16.8\text{cm}^{-1}$  and  $8.2\text{cm}^{-1}$  below  $\nu_8$  in the  $\text{H}_2\text{CCO}$ ,

Table 2.19. Individual  $r_{Q_{Ka}}$  and  $p_{Q_{Ka}}$  assignments for  $\nu_8$  of isotopic ketenes and derived  $^{13}\text{C}$  shifts,  $\text{cm}^{-1}$ .

	$\text{H}_2\text{CCO}$	$\text{H}_2\text{C}^{13}\text{CO}$	Shift	$\text{H}_2^{13}\text{CCO}$	Shift
$r_{Q_4}$	1071.84	1060.96	10.88		
$r_{Q_3}$	1049.80	1039.22	10.58	1042.12 <sup>a</sup>	7.68
$r_{Q_2}$	1027.95	1017.44	10.51	1020.22	7.73
$r_{Q_1}$	1007 <sup>b,c</sup>	996.65 <sup>b,c</sup>	10.35	999.32 <sup>b,c</sup>	7.68
$r_{Q_0}$	987.2 <sup>a,b</sup>	976.80 <sup>b</sup>	10.40	979.44 <sup>b</sup>	7.76
$p_{Q_1}$	968.61 <sup>b,d</sup>	958.17 <sup>b</sup>	10.44	960.03 <sup>b,d</sup>	(8.58)
$p_{Q_2}$					
$p_{Q_3}$	934.65	924.18	10.47	926.83	7.82
$p_{Q_4}$	919.31	908.82	10.49	911.44	7.85
$p_{Q_5}$	905.12	894.56	10.56	897.28	7.84
$p_{Q_6}$	891.98	881.36	10.62	881.36	7.85
$p_{Q_7}$	879.88	869.17	10.71	872.04	7.84
$p_{Q_8}$	898.64	857.90	10.74	860.82	7.82
$p_{Q_9}$	858.54	847.66	10.88	850.76	7.78

<sup>a</sup> Overlapping absorption.

<sup>b</sup> Absorption minima.

<sup>c</sup> Weak absorption.

<sup>d</sup> Uncharacteristic degradation pattern.

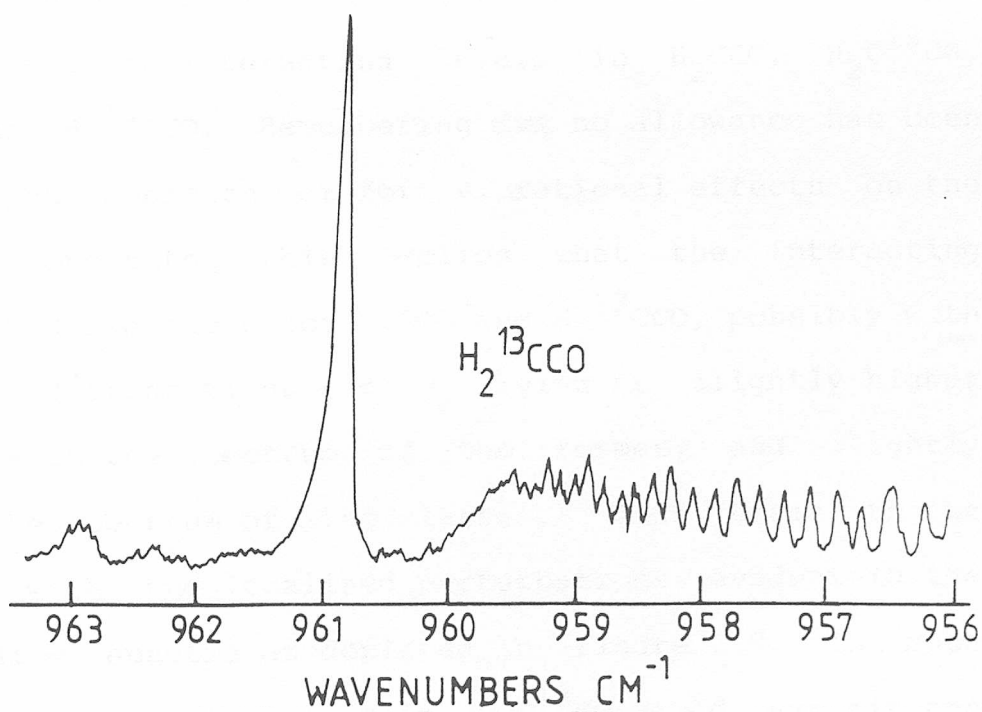
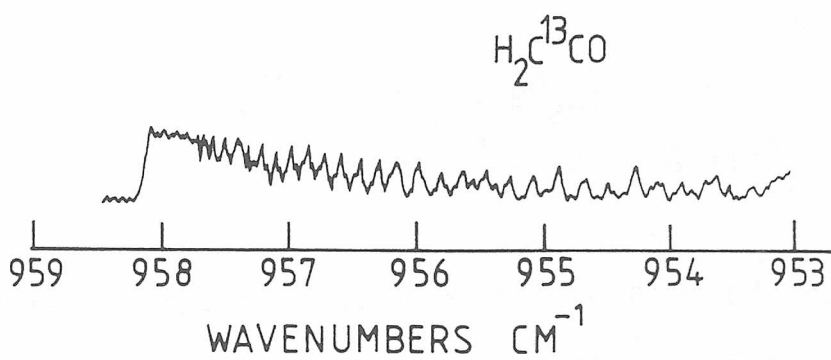
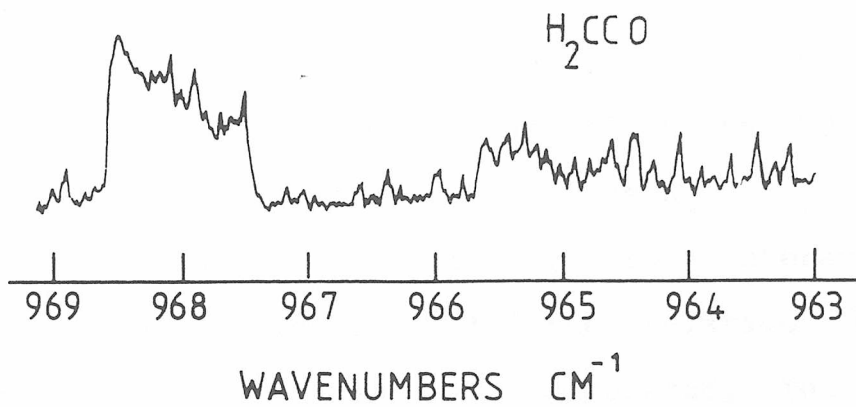


Figure 2.9 Comparison of the  $\text{P}_{\text{Q}_1}$  absorptions of  $\nu_8$  fundamentals of  $\text{H}_2\text{CCO}$ ,  $\text{H}_2\text{C}^{13}\text{CO}$  and  $\text{H}_2^{13}\text{CCO}$ .

$\text{H}_2\text{C}^{13}\text{CO}$  and  $\text{H}_2^{13}\text{CCO}$  spectra respectively. The  $\nu_8$  and  $\nu_6 + \nu_9$  vibrations can interact through a b-axis  $K_a' \pm 1$  Coriolis interaction by rotation about the b-axis, though only a  $K_a' + 1$  interaction can affect the  $P_{Q_1}$  absorption since it involves transitions to the  $K_a' = 0$  level. The difference in the energies for the two interacting levels can give an indication of the relative extents of interaction. This can be calculated, in the first approximation in terms of the following expression:

$$(E_{K_a'=0}^8 - E_{K_a'=1}^{69}) = (E_8^0 - E_{69}^0) + \{(A' - \bar{B}')_0^2 - (A' - \bar{B}')_1^2\} \quad 2.6$$

On the assumption that  $A' \approx A''$  and  $B' \approx B''$  for  $\nu_6 + \nu_9$ , then differences of  $\sim +1.3\text{cm}^{-1}$ ,  $\sim +7.7\text{cm}^{-1}$  and  $\sim -0.9\text{cm}^{-1}$  are calculated for the interacting levels in  $\text{H}_2\text{CCO}$ ,  $\text{H}_2\text{C}^{13}\text{CO}$ ,  $\text{H}_2^{13}\text{CCO}$  and  $\text{H}_2^{13}\text{CCO}$ . Remembering that no allowance has been made for anharmonicity or for vibrational effects on the rotational constants, this implies that the interacting levels should lie close for  $\text{H}_2\text{CCO}$  and  $\text{H}_2^{13}\text{CCO}$ , possibly with the  $K_a' = 0$  transitions, of  $\nu_8$  lying at slightly higher frequencies in the spectrum of the former, and slightly lower in the spectrum of the latter. This seems to be consistent with the localised perturbations evident in the corresponding spectra as depicted in figure 2.9. The much larger separation of levels in  $\text{H}_2\text{C}^{13}\text{CO}$  would explain the seemingly unperturbed appearance of  $P_{Q_1}$  for this isotopomer. The interaction is clearly a very small one, and is unlikely to produce significant effects in other subbands, due to the

larger separations of interacting levels involved.

The  $^{13}\text{C}$  shifts determined from all other  $^p\text{Q}_{\text{Ka}}$  and  $^r\text{Q}_{\text{Ka}}$  transition are consistent, as can be seen in table 2.19. From these subband shifts, the band origins and the frequency shifts are estimated and listed in table 2.20. These are considered to be accurate to within  $\pm 0.1\text{cm}^{-1}$ .

Table 2.20. Frequencies and  $^{13}\text{C}$  frequency shifts for  $\nu_8$ ,  $\text{cm}^{-1}$ .

	$\text{H}_2\text{CCO}$	$\text{H}_2\text{C}^{13}\text{CO}$	$\text{H}_2^{13}\text{CCO}$
$\nu_8$	977.8 <sup>a</sup>	967.36 <sup>b</sup>	970.00 <sup>b</sup>
$\Delta\nu_8$	-	10.44	7.80

<sup>a</sup> Nemes (54).

<sup>b</sup> Calculated in terms of  $\text{H}_2\text{CCO}$  frequency.

#### Comparison of $\nu_8$ and $2\nu_8$ $^{13}\text{C}$ shift data

The  $^{13}\text{C}$  shifts to the  $\nu_8$  vibration may, in fact be obtained from two sources. Firstly, as above, by comparison of the contours of  $\nu_8$  in the  $\text{H}_2\text{CCO}$ ,  $\text{H}_2\text{C}^{13}\text{CO}$  and  $\text{H}_2^{13}\text{CCO}$  spectra. Secondly,  $^{13}\text{C}$  shifts are available from subband analyses of  $2\nu_8$  (see section 2.4(g)), where the shifts on  $\nu_8$  may be taken to be half of the observed shifts on  $2\nu_8$  for the same isotopomers. This assumes a common anharmonicity factor. The calculated shifts are collected in table 2.21.

Despite the slight disparity between the  $\text{H}_2\text{C}^{13}\text{CO}$  shifts estimated by the two methods, the agreement is pleasing and demonstrates the accuracy with which the  $^{13}\text{C}$  shifts to the B-type and C-type vibrations are determined. From these comparisons, values of  $10.5\text{cm}^{-1}$  and  $7.8\text{cm}^{-1}$  are thus believed to represent the most accurate  $\nu_8$  frequency shifts for  $\text{H}_2\text{C}^{13}\text{CO}$  and  $\text{H}_2^{13}\text{CCO}$  respectively.

Table 2.21. Comparison of  $\nu_8$   $^{13}\text{C}$  frequency shifts as determined from both fundamental and overtone studies,  $\text{cm}^{-1}$ .

	$\text{H}_2\text{C}^{13}\text{CO}$	$\text{H}_2^{13}\text{CCO}$
$\Delta\nu_8$	10.44	7.80
$1/2(\Delta 2\nu_8)^a$	<u>10.62</u>	<u>7.81</u>
Average	10.53	7.80

<sup>a</sup> Values quoted assume negligible anharmonicity contributions.

(j)  $\nu_5$ , CCO deformation,  $587\text{cm}^{-1}$   
and  $\nu_6$ ,  $\text{CH}_2$  wagging,  $528\text{cm}^{-1}$

The C-type  $\nu_5$  and  $\nu_6$  vibrations at  $587\text{cm}^{-1}$  and  $528\text{cm}^{-1}$  in the  $\text{H}_2\text{CCO}$  were most recently examined by Nemes (54). His studies indicated major Coriolis a-axis perturbations of these vibrations through interaction with  $\nu_8$  and  $\nu_9$ . In the present studies, the  $\text{H}_2\text{CCO}$   $\nu_5$  and  $\nu_6$  bands have been

reexamined and their contours compared with those of the same vibrations in the  $\text{H}_2\text{C}^{13}\text{CO}$  and  $\text{H}_2^{13}\text{CCO}$  species in order to determine  $^{13}\text{C}$  frequency shifts. The analyses were hindered by the presence of a number of hot bands in the region in addition to some  $\text{CO}_2$  absorptions originating from contamination within the samples. Further difficulties were experienced in locating the  $^p\text{Q}_{\text{Ka}}$  absorptions for both vibrations: for the  $\nu_5$  vibrations, significant intensity perturbations resulted in low intensity in the P wing, whilst instrumentation limitations prevented the recording of spectra of good quality below  $\sim 420\text{cm}^{-1}$  for  $\nu_6$ . The assigned  $^r\text{Q}_{\text{Ka}}$  and  $^p\text{Q}_{\text{Ka}}$  frequencies, together with the calculated subband shifts for  $\nu_5$  and  $\nu_6$  are listed in tables 2.22 and 2.23 respectively.

Figures 2.10 and 2.11 display the variation of the  $\text{H}_2\text{C}^{13}\text{CO}$  and  $\text{H}_2^{13}\text{CCO}$  frequency shifts relative to  $\text{H}_2\text{CCO}$  for  $\nu_5$  and  $\nu_6$ . Large variations in the shifts to individual subbands of  $\nu_5$  and  $\nu_6$  for  $\text{H}_2\text{C}^{13}\text{CO}$ , are mainly attributable to significant changes in the extents of a-axis Coriolis interactions in  $\text{H}_2\text{CCO}$  and  $\text{H}_2\text{C}^{13}\text{CO}$ . By contrast, the  $\text{H}_2^{13}\text{CCO}$  shifts remain reasonably constant over all the subbands, indicative of Coriolis interaction of more or less the same extent as in  $\text{H}_2\text{CCO}$ . Quantification of these perturbations in the  $^{13}\text{C}$  spectra was not attempted.

From the lower  $^p\text{Q}_{\text{Ka}}$  and  $^r\text{Q}_{\text{Ka}}$  absorptions, the best estimates of the true vibrational frequency shifts to  $\nu_5$  and  $\nu_6$  for  $\text{H}_2\text{C}^{13}\text{CO}$  and  $\text{H}_2^{13}\text{CCO}$  were obtained relative to the

Table 2.22. Individual  $r_{Q_{Ka}}$  and  $p_{Q_{Ka}}$  assignments for  $\nu_5$  of isotopic ketenes and derived  $^{13}\text{C}$  shifts,  $\text{cm}^{-1}$ .

	$\text{H}_2\text{CCO}$	$\text{H}_2\text{C}^{13}\text{CO}$	Shift	$\text{H}_2^{13}\text{CCO}$	Shift
$r_{Q_9}$	840.45 <sup>a</sup>	833.07	7.38	841.06	-0.61
$r_{Q_8}$	811.32	803.41	7.91	811.54	-0.22
$r_{Q_7}$	781.88	773.87	8.01	782.20	-0.32
$r_{Q_6}$	752.58	744.55	8.03	752.80	-0.22
$r_{Q_5}$	723.70	715.78	7.92	723.85	-0.15
$r_{Q_4}$	695.58	687.96	7.62	695.65	-0.17
$r_{Q_3}$	668.50	661.31	7.19	668.61	-0.11
$r_{Q_2}$	642.96	636.36	6.60	642.89	0.07
$r_{Q_1}$	619.20	613.15	6.05	619.10	0.10
$r_{Q_0}$	597.70	592.30	5.40	597.40 <sup>b,c</sup>	0.30
$p_{Q_1}$	578.32	573.07 <sup>b</sup>	5.25	577.95	0.37
$p_{Q_2}$	561.02 <sup>b</sup>				
$p_{Q_3}$	546.70	540.81	5.89	546.50 <sup>c</sup>	0.20
$p_{Q_4}$	535 <sup>c</sup>	527.70	7.3	534.11	0.89
$p_{Q_5}$	523.78	516.57	7.21	523.62	0.16

<sup>a</sup> Broad absorption.

<sup>b</sup> Overlapping absorption.

<sup>c</sup> Tentative assignment.

Table 2.23. Individual  $r_{Q_{Ka}}$  and  $p_{Q_{Ka}}$  assignments for  $\nu_6$  of isotopic ketenes and derived  $^{13}\text{C}$  shifts,  $\text{cm}^{-1}$ .

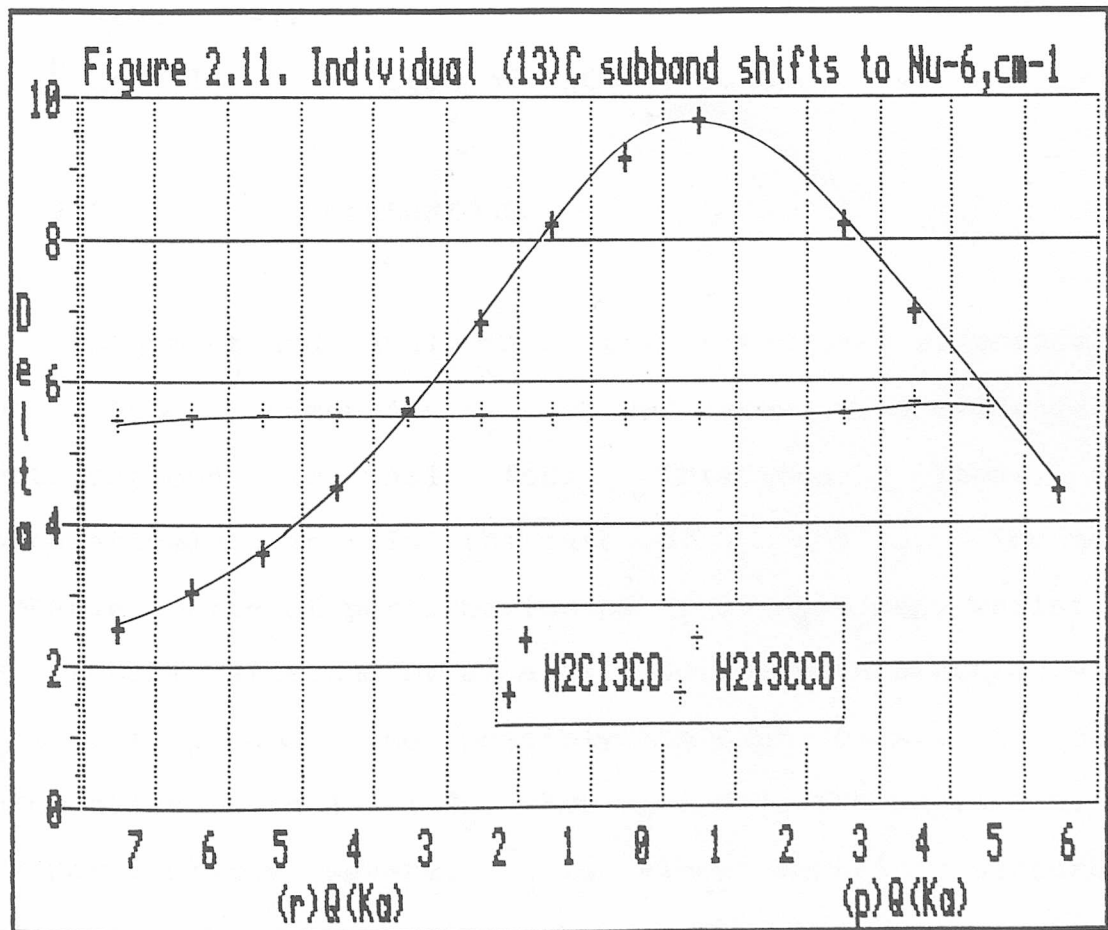
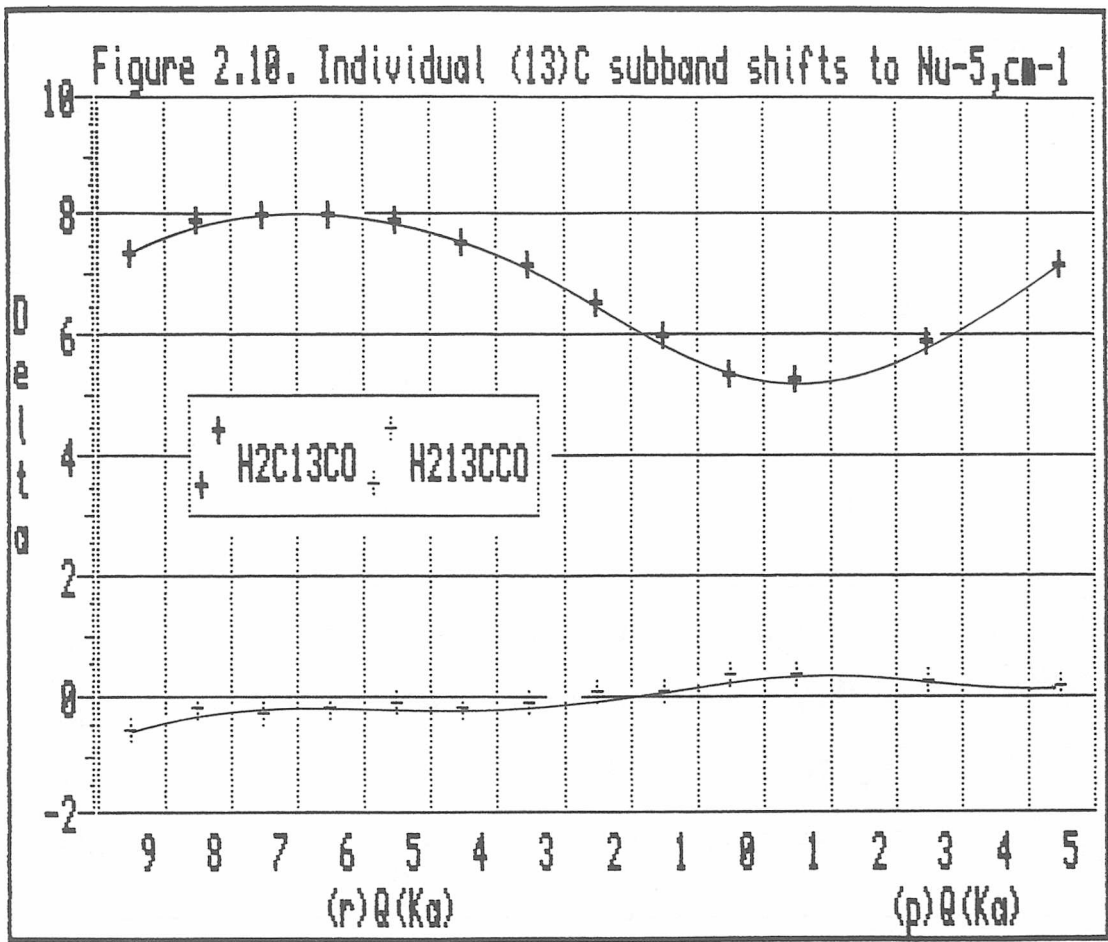
	$\text{H}_2\text{CCO}$	$\text{H}_2\text{C}^{13}\text{CO}$	Shift	$\text{H}_2^{13}\text{CCO}$	Shift
$r_{Q_7}$	648.05	645.48	2.57	642.58	5.47
$r_{Q_6}$	634.81	631.74	3.07	629.29	5.52
$r_{Q_5}$	620.60	616.98	3.62	615.10	5.50
$r_{Q_4}$	605.55	601.01	4.54	600.04	5.51
$r_{Q_3}$	589.32	583.73	5.59	583.80	5.52
$r_{Q_2}$	572.09	565.26	6.83	566.59	5.50
$r_{Q_1}$	553.94 <sup>a</sup>	545.71 <sup>a</sup>	8.23	548.43 <sup>a</sup>	5.51
$r_{Q_0}$	535.40	526.24 <sup>b</sup>	9.16	529.90	5.50
$p_{Q_1}$	517.00 <sup>c</sup>	507.32 <sup>c</sup>	9.68	511.48 <sup>c</sup>	5.52
$p_{Q_2}$	499 <sup>d</sup>	490 <sup>d</sup>	9	493.59 <sup>c</sup>	5.4
$p_{Q_3}$	481.38 <sup>c</sup>	473.22 <sup>c</sup>	8.17	475.84 <sup>c</sup>	5.54
$p_{Q_4}$	463.51	456.53	6.98	457.83	5.68
$p_{Q_5}$	444.59 <sup>c</sup>	438.97 <sup>c</sup>	5.62	438.95 <sup>c</sup>	5.64
$p_{Q_6}$	424.98	420.49	4.49		

<sup>a</sup> Absorption minima.

<sup>b</sup> Overlapping absorption.

<sup>c</sup> Mid absorption point.

<sup>d</sup> Tentative assignment.



corresponding  $\text{H}_2\text{CCO}$  frequencies. These are given in table 2.24 and the shifts are estimated to be accurate to about  $\pm 0.1\text{cm}^{-1}$ .

Table 2.24. Frequencies and  $^{13}\text{C}$  frequency shifts for  $\nu_5$  and  $\nu_6$ ,  $\text{cm}^{-1}$ .

	$\text{H}_2\text{CCO}$	$\text{H}_2\text{C}^{13}\text{CO}$	$\text{H}_2^{13}\text{CCO}$
$\nu_5$	587.30 <sup>a</sup>	581.90 <sup>b</sup>	586.93 <sup>b</sup>
$\nu_6$	528.36 <sup>a</sup>	518.68 <sup>b</sup>	522.84 <sup>b</sup>
$\Delta\nu_5$	-	5.40	0.37
$\Delta\nu_6$	-	9.68	5.52

<sup>a</sup> Nemes (54).

<sup>b</sup> Calculated in terms of  $\text{H}_2\text{CCO}$  frequency.

## 2.5 CONCLUSIONS

Assignment and analysis of the rotational structure in the A-type fundamentals  $\nu_1 - \nu_4$  of ketene give evidence of perturbations in all four vibrations. These are comparatively minor in the case of  $\nu_1$  and  $\nu_2$ . The most probable source of perturbation of  $\nu_1$  is  $\nu_4 + 2\nu_8$ , whilst  $\nu_2$  is probably affected by an a-axis Coriolis interaction with  $\nu_4 + \nu_5 + \nu_9$  and also possibly through b-axis Coriolis interaction with  $2\nu_5 + \nu_8$ . For  $\nu_3$  and  $\nu_4$  the perturbations are particularly severe.  $\nu_3$  is almost certainly perturbed by a close Fermi resonance with  $\nu_8 + \nu_9$ , whilst  $\nu_4$  is most

probably affected by Fermi resonance with all of  $2\nu_5$ ,  $2\nu_6$  and  $\nu_5 + \nu_6$ .

In the  $\text{H}_2\text{C}^{13}\text{CO}$  and  $\text{H}_2^{13}\text{CCO}$ , the A-type fundamentals appear to suffer the same perturbations, except for  $\nu_2$  which suffers an isotopic shift of  $56.5\text{cm}^{-1}$ , effectively removing it from the vicinity of  $\nu_4 + \nu_5 + \nu_9$ , but bringing it closer to  $2\nu_8$ .

In dideuteroketene, only  $\nu_1$  appears to be essentially unperturbed.  $\nu_2$  suffers minor perturbations with an apparent crossing of energy levels between  $K_a = 6$  and 7, probably through Fermi resonance with  $\nu_3 + 2\nu_6$ , although rotational resonance with  $\nu_3 + \nu_5 + \nu_9$  may also contribute.  $\nu_3$  is once again in strong Fermi resonance with  $\nu_8 + \nu_9$ , which lies slightly lower in this case.  $\nu_4$  lies between  $\nu_5 + \nu_6$  and  $2\nu_6$ , both of which affect it by Fermi resonance;  $2\nu_5$  lies nearly  $160\text{cm}^{-1}$  higher, so its resonance effects on  $\nu_4$  are comparatively small.

Preliminary studies of the rotational structure in the  $B_1$  and  $B_2$  fundamentals  $\nu_5 - \nu_8$  for  $\text{H}_2\text{CCO}$ ,  $\text{H}_2\text{C}^{13}\text{CO}$  and  $\text{H}_2^{13}\text{CCO}$  indicate that these are also significantly perturbed. The low-lying C-type fundamentals,  $\nu_5$  and  $\nu_6$ , and B-type fundamentals,  $\nu_8$  and  $\nu_9$  (the latter being too low to be detected) Coriolis interact through rotation about the a-axis as previous studies have found (54).  $\nu_8$  also shows evidence of a small localised b-axis Coriolis interaction with  $\nu_6 + \nu_9$  which lies in close proximity.

In the  $D_2CCO$  spectrum, the four lowest fundamentals,  $\nu_5$ ,  $\nu_6$ ,  $\nu_8$  and  $\nu_9$  are again in strong Coriolis resonance, an analysis of which has very recently been performed (56).

In the analysis of the B-type  $\nu_7$  above  $3000\text{cm}^{-1}$ , it is interesting to note that perturbations were again observed and that the overall fit to the observations is rather poor (55), just as has generally been found for the A-type vibrations. Moreover, the parameters so determined for the antisymmetric  $CH_2$  stretching fundamental include a value of  $\Delta_K'$  which is 12 times the magnitude of the ground state value, similar to the observations on the  $\nu_4$  band lying at  $1116\text{cm}^{-1}$ . The cause is Fermi resonance between  $\nu_7$  and  $\nu_2 + \nu_8$ . A similar perturbation has been found for  $\nu_7$  in the  $H_2^{13}CCO$  spectrum. As a consequence of the large shift on  $\nu_2$  in  $H_2C^{13}CO$  however, perturbation of  $\nu_7$  by  $\nu_2 + \nu_8$  is substantially reduced. These perturbations have been quantified and corrected.

Preliminary analysis of the first overtones of the out of plane bend,  $2\nu_5$  and  $CH_2$  wag,  $2\nu_6$  in  $H_2CCO$ ,  $H_2C^{13}CO$  and  $H_2^{13}CCO$  give clear evidence of perturbations caused mainly by Fermi resonance interaction with  $\nu_4$ .

Finally, analysis of the  $CH_2$  rock overtone  $2\nu_8$  indicates that the band is essentially unperturbed vibrationally. The derived  $^{13}C$  frequency shifts agree well with those predicted from studies of the fundamental.

Clearly ketene is a molecule the vibrations of which are highly perturbed in the gas phase. An energy level manifold of fundamental and binary vibration levels below  $3300\text{cm}^{-1}$  is shown in figure 2.12, in which a few ternary vibrations are included where it is considered that they perturb the fundamentals. The major Coriolis interactions involving the four lowest levels  $\nu_5$ ,  $\nu_6$ ,  $\nu_8$  and  $\nu_9$  reproduces itself throughout the manifold, and in a particularly complicated and extended form for  $A_1$  species vibrations. Indeed, as can be seen in figure 2.12, the interaction involving binary levels extends uninterrupted through levels from above  $1900\text{cm}^{-1}$  to below  $900\text{cm}^{-1}$ . This must contribute in a complicated manner to the perturbations observed in the  $\nu_3$  and  $\nu_4$  bands, and may even extend to involve  $\nu_2$ .

For dideuteroketene, resonances between  $\nu_5$ ,  $\nu_6$ ,  $\nu_8$  and  $\nu_9$  lead to a highly complex interacting set of 16 binary vibration energy levels, similar to that in figure 2.12, some of which, in turn, interact with the  $\nu_3$  and  $\nu_4$  fundamentals.

The vibrational frequencies and  $^{13}\text{C}$  shifts determined from these studies are collected in table 2.25 for ease of reference. They were used to assist in empirical force field calculations for ketene discussed in the following chapter. However, the value to such calculations of a number of the frequencies and shifts, particularly for the  $A_1$  fundamentals, was anticipated to be somewhat limited, due to the effects of the perturbations found to be present, and

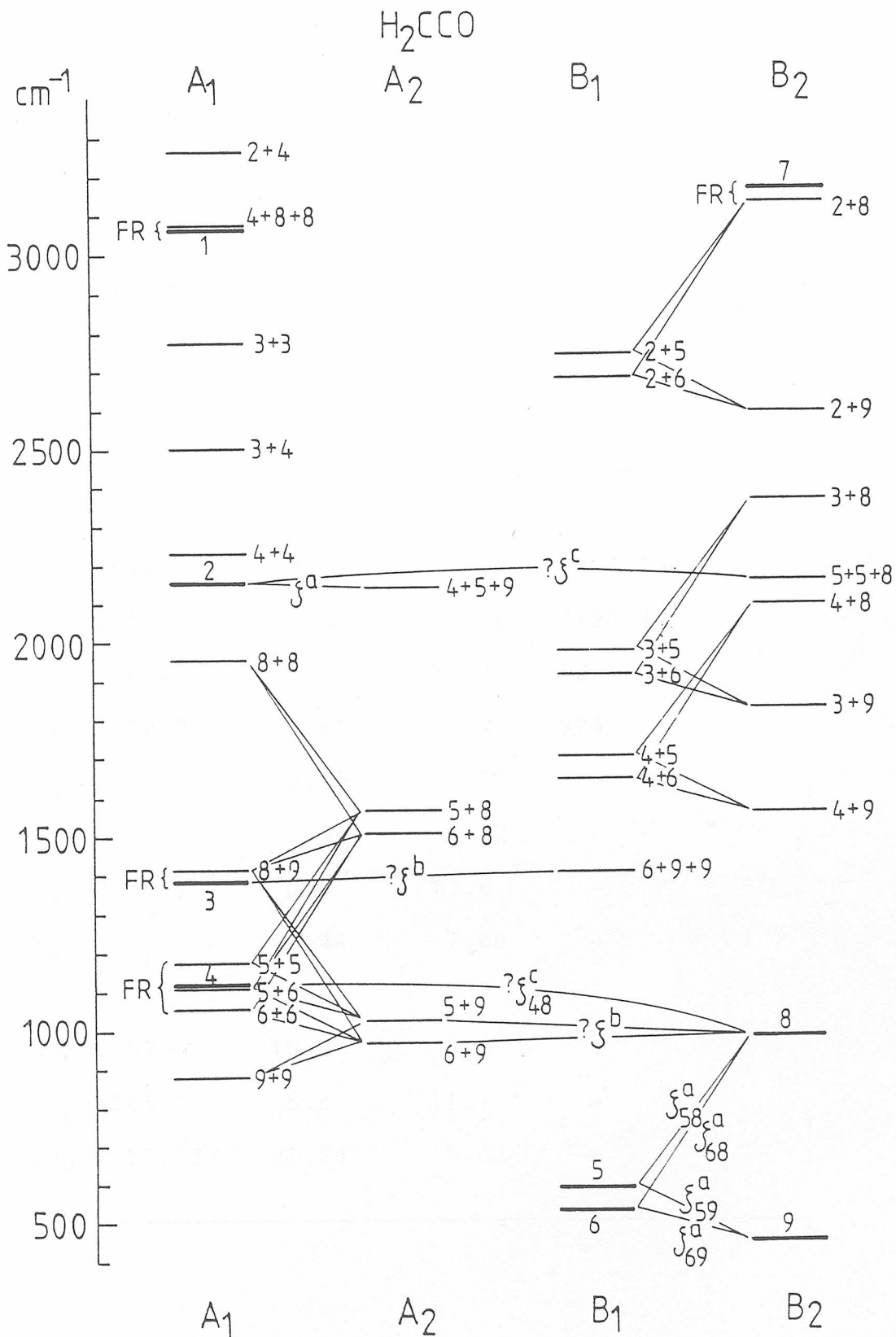


Figure 2.12 Energy level manifold for  $\text{H}_2\text{CCO}$ , showing fundamental and binary vibration levels, interconnected by Fermi resonance and Coriolis interactions. A few ternary levels are included, where they are considered to cause perturbations to the  $A_1$  species fundamentals analysed in this work.

discussed in this chapter.

Table 2.25. A summary of frequencies and  $^{13}\text{C}$  frequency shifts determined in the present studies,  $\text{cm}^{-1}$ .

	$\text{H}_2\text{CCO}$	$\text{H}_2\text{C}^{13}\text{CO}$	$\text{H}_2^{13}\text{CCO}$	$\text{D}_2\text{CCO}$
$\nu_1$	3070.4	0.17	5.70	2267.32
$\nu_2$	2152.56	56.59	5.36	2120.49
$\nu_3$	1387.5	1.5	12.4	1225
$\nu_4$	1116.01	7.91	5.21	924.7
$\nu_5$	-	5.40	0.37	-
$\nu_6$	-	9.68	5.52	-
$\nu_7$	3158.7	0.0	13.6	-
$\nu_8$	-	10.44	7.80	-
$2\nu_5$	1187.5	10.2	5.3	-
$2\nu_6$	1065.1	8.6	11.1	-
$2\nu_8$	1952.353	21.24	15.63	-

## CHAPTER 3

### AB INITIO AND EMPIRICAL FORCE FIELD STUDIES OF KETENE

#### 3.1 INTRODUCTION

The earliest empirical harmonic force field of ketene was determined by Moore and Pimentel (52) in terms of frequency data from the infrared spectra of the  $\text{H}_2\text{CCO}$ ,  $\text{HDCCO}$  and  $\text{D}_2\text{CCO}$  isotopomers. However, these authors found it necessary to constrain somewhat arbitrarily six of the interaction force constants to zero as a result of insensitivities toward the available data.

Later, Fletcher and Thompson (60) preferred to constrain two of these interaction constants to interrelated values instead of zero, in accordance with the hybrid orbital force field model of Mills (61).

In subsequent studies by McKean and Duncan (28), it was found that there were two physically acceptable force field solutions to the out-of-plane vibrations. Although the

second solution had previously been ignored, it described the available data equally well. They showed that Coriolis constant or frequency shift data would discriminate between the alternative sets.

The most recent empirical force field studies of ketene were carried out by Mallinson and Nemes (59), who introduced centrifugal distortion constants for the  $\text{H}_2\text{CCO}$ ,  $\text{HDCCO}$ ,  $\text{D}_2\text{CCO}$  species and as well as Coriolis coupling constants for the low lying vibrations in the  $\text{H}_2\text{CCO}$  species. This permitted the determination of two more interaction force constants and also allowed the discrimination between the alternative out-of-plane force constants. However, their force field is most notably deficient in describing the totally symmetric  $A_1$  vibrations, where three out of the four remaining constraints were imposed.

The only previously reported ab initio force field study of ketene was carried out by Pouchan et al. (62), who performed HF-SCF calculations using a minimal type STO-3G basis set. The same authors also predicted the force constants for ketene by a semi-empirical MINDO/2 approach and compared these with their ab initio findings.

Gleghorn and McConkey (63) also performed MINDO/2 type calculations on ketene, but many of their force constants differ significantly with those determined by the same method by Pouchan et al. (62).

By introduction of new frequency data from isotopic ketenes (discussed in chapter 2), including data from the  $\text{H}_2\text{C}^{13}\text{CO}$  and  $\text{H}_2^{13}\text{CCO}$  species, it was hoped to determine a more accurate empirical harmonic force field for ketene. However, the numerous Fermi resonance interactions, particularly in the  $A_1$  block vibrations were anticipated to lead to indeterminacies in the  $A_1$  force constants. Thus to arrive at a reliable general harmonic force field (GHFF) for ketene, complementary and supplementary ab initio studies were also performed.

In the present ab initio force field studies, it was anticipated that better quality force fields for ketene would be determined by HF-SCF calculations using split-valence contracted gaussian basis functions of the Pople group (34,36-40) and also of Pulay et al (35). This type of basis set has been found to predict molecular properties somewhat better than the largely inferior minimal type basis used by Pouchan et al. (62).

### 3.2 SYMMETRY COORDINATES

The symmetry coordinates adopted in the present studies are those previously defined by Moore and Pimentel (52). These are given in table 3.1 and the positive displacements for each of these are illustrated in figure 3.1. In the ab initio studies, these coordinate definitions were readily constructed within the program (TEXAS (64): see section

Table 3.1 Symmetry coordinates for ketene.

---


$$\begin{aligned}
 S_1 &= (\delta r_1 + \delta r_2)/(2)^{1/2} \\
 S_2 &= \delta r_3 \\
 S_3 &= \delta r_4 \\
 S_4 &= \delta \alpha \\
 \\ 
 S_5 &= \delta \phi_x \\
 S_6 &= \delta \gamma \\
 \\ 
 S_7 &= (\delta r_1 - \delta r_2)/(2)^{1/2} \\
 S_8 &= \delta \beta \\
 S_9 &= \delta \phi_y
 \end{aligned}$$


---

$\delta\gamma$  and  $\delta\beta$  measure the change in the angle between the bisector of the HCH angle and the CC bond projected in the xz and yz plane respectively.  $\phi_x$  and  $\phi_y$  measure the CCO angle bending in the xz and yz plane respectively. The sense of the positive displacement is such that the CH<sub>2</sub> group, or CCO group, bends towards the positive x or y axis. See figure 2.1

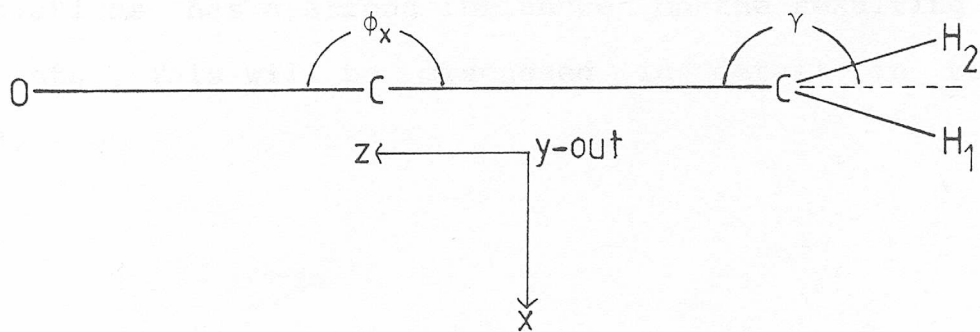
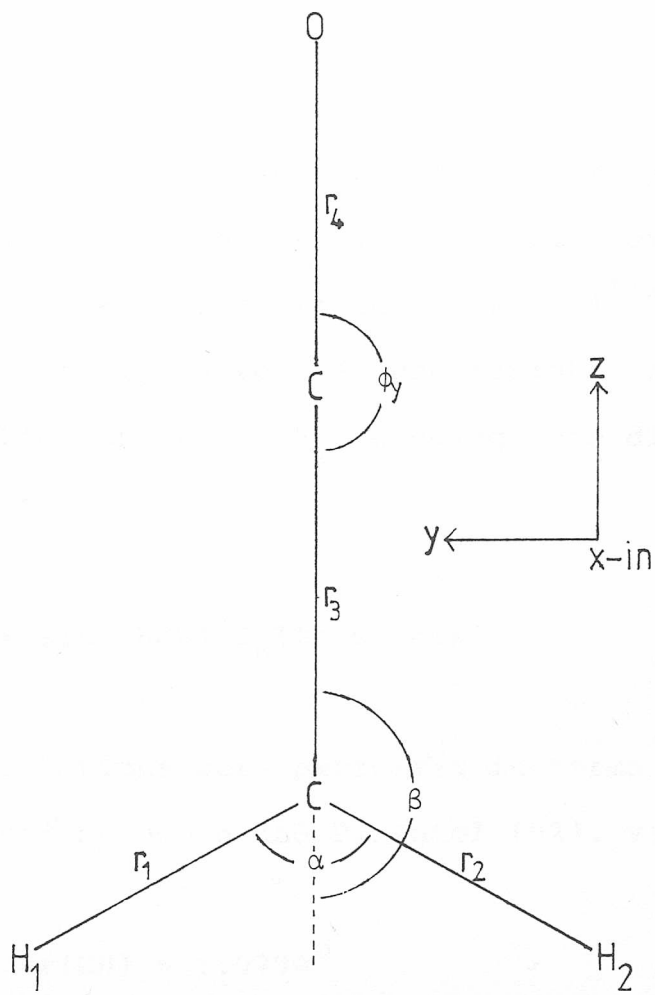


Figure 3.1. Internal valence displacement coordinates for ketene.

3.3.1), thus allowing direct comparison with the empirical force field.

This set of coordinates appears to be similar to that used by Mallinson and Nemes (59) with two exceptions. Firstly, their CH<sub>2</sub> rocking coordinate S<sub>8</sub> is -(2)<sup>1/2</sup> times S<sub>8</sub> of this work. Secondly, there is uncertainty associated with their definition of the CH<sub>2</sub> wagging coordinate S<sub>6</sub>, where it appears that

$$S_6(\text{M\&N}) = \sin(\langle\text{HCH}\rangle) \cdot S_6(\text{this work})$$

Empirical calculations were performed in terms of the r<sub>0</sub> structure determined by Moore and Pimentel (52), viz

$$r(\text{CH}) = 1.079\text{\AA}$$

$$r(\text{CC}) = 1.314\text{\AA}$$

$$r(\text{CO}) = 1.161\text{\AA}$$

$$\alpha(\text{HCH}) = 122.0^\circ$$

The selection of the geometry used in ab initio calculations has a strong influence on the resulting force constants. This will be discussed in detail in section 3.3.3.

### 3.3 AB INITIO GEOMETRY AND FORCE FIELD STUDIES OF KETENE

#### 3.3.1 HARDWARE AND SOFTWARE

All ab initio calculations were carried out on Robert Gordon's Institute of Technology's mainframe computer, the DECSYSTEM-20. This system is large enough to cope with moderately sophisticated ab initio programs. Its operating times were such that it offered the advantage of virtually continuous access. In addition, the available memory of the DECSYSTEM-20 was such that practical limitations of computing space were not encountered. However, execution times tended to be rather long, particularly daytime executions, owing to simultaneous access by other system users.

Ab initio calculations were carried out by utilization of the ab initio gradient program TEXAS (64). This is a one-configuration HF-SCF type program and the version utilized had previously been modified to incorporate iterative equilibrium geometry and saddle point optimisation routines, collectively referred to as MINIT (65). The smallest basis set used in the studies of ketene, the 4-21G (36) generally took less than 3 minutes CPU time to evaluate the SCF energy whilst the largest basis, the 6-31G\*\* (35,41) took over an hour. The more costly gradient evaluations generally took about 10 minutes and over 6 hours for the same basis sets respectively.

TEXAS has been used to carry out a comprehensive study of the molecular properties of small molecules by Pulay et al. (36). It has also been used by Schlegel et al. (66) to calculate the force constants of first row hydrides. More recently, TEXAS had been used to predict the force constants for glyoxal, acrolein, formaldehyde and ethylene (67). For ethylene (68) in particular, the ab initio force constants are in excellent agreement with highly accurate empirical constants determined by Duncan and Hamilton (69).

### 3.3.2 SELECTION OF THE BASIS FUNCTIONS

The selection of the basis functions for the present ab initio studies of ketene required careful prior consideration. It was necessary to employ basis sets which give adequate descriptions of the molecular wavefunction but which are small enough to be economical.

TEXAS limits the choice of basis functions to s and p primitive gaussian functions. Thus discussion will be restricted to this type of basis functions.

Force constant calculations have been performed in terms of valence shell triple-zeta (TZ) basis sets (70,71). These have been found to give fairly good predictions at the SCF level, but force field evaluation times are excessive (35, and references therein). Contraction of a TZ to a double-zeta (DZ) type representation in the valence shell and to a minimal basis (single-zeta) in the core has been

reported to have practically no numerical effect on resulting ab initio force fields (35). At the same time, there is a substantial reduction in the required computing time. Such bases are denoted as split-valence contracted gaussian basis sets (see also section 1.3.3). A number of these have been developed by Pople and coworkers (34,35,37-40) as well as by Pulay et al. (36) and have been used extensively to predict ab initio molecular properties at the SCF level. A distinguishing feature of this type of basis is the equality of the valence shell s and p exponents, which reduces the computing times. This feature is readily exploited by TEXAS (64).

Faster evaluation times can be achieved by further contraction of the valence shell to a minimal type basis. However, this has been shown to have detrimental effects on force constants (36) and so the minimal type basis was considered inappropriate for the present studies. The most appropriate type of basis for this work thus appeared to be the split-valence type basis sets.

With regard to scaling of the atomic basis function exponents to approximate more closely to molecular environments (72) (see also section 1.3.3), it was decided to follow the recommendations of the appropriate authors for the scaling of their basis sets.

The split-valence and other basis sets are often supplemented with higher angular momentum or "polarisation"

terms (40,41), most notably d-type functions for heavy centres and p-type functions for hydrogen. Addition of polarisation functions is often desirable since they give rise to molecular properties which are close to the HF limit but this is offset by a corresponding increase in computing expense.

The way in which the polarisation functions were introduced in the present studies has been largely dictated by TEXAS. The p-type primitive hydrogen polarisation functions are readily accommodated whilst the d-type functions are constructed from p-type gaussian functions, in accordance with recommendations by the program's author. This gives rise to six second order d functions

$$(x^2, y^2, z^2, xy, yz, xz) \exp(-\alpha_d r^2) \quad 3.1$$

which are equivalent to the five pure d-type functions

$$(3z^2 - r^2, xy, yz, xz, x^2 - y^2) \exp(-\alpha_d r^2) \quad 3.2$$

plus an s function (which is generally tolerated (64)). It was also necessary to select values for the polarisation exponents,  $\alpha_d$  for heavy centres and  $\alpha_p$  for hydrogen. Hariharan and Pople (41,42) found little dependence of  $\alpha_d$  on different chemical environments for C, N, O and F and adopted an average exponent of 0.8. A p-type hydrogen exponent of 1.1 was also recommended by the same authors.

The selected reference geometry around which derivative are calculated has quite a significant effect on the harmonic force constants, particularly stretching constants. Thus, in a similar fashion to the selection of the basis functions, the reference geometry must also be carefully selected. Ideally, true equilibrium for the molecule should be used, but for most molecules, this is not known. Frequently, the configuration corresponding to the theoretical energy minimum is used and has produced satisfactory results. However, errors arising from core-core repulsion terms in the HF approximation are often dominant contribution to the errors in force constants. Generally, theoretical geometries can be in error by as much as 10% whilst experimental geometry parameters such as  $r_o$ ,  $r_z$ , etc. are usually less than 2% in error. The experimental geometries are therefore considered to be better estimations of true equilibrium. From comprehensive studies of the geometries of small molecules by Pulay et al. (36) and Blom et al. (46) a set of empirical corrections to theoretical geometries were proposed. These will be discussed later.

Molecular geometries (and hence force constants) also have some dependence on the basis set used. This has been discussed by several authors (10,36,37,73,74). No such study has been found for ketene and thus a limited study of

the ab initio equilibrium configurations for different basis sets was carried out and compared with experimental values.

Ab initio equilibrium configurations were obtained by use of the MINIT routine (65). It includes a force relaxation routine (45) (see section 1.3.5) which utilizes a quasi-Newton type convergence method to obtain theoretical minima on molecular hypersurfaces. Molecules were considered to be sufficiently relaxed to be at equilibrium when internal forces of considerably less than 0.005mdyn remained on each centre. This criterion for the attainment of equilibrium was advocated by Schaefer (75) and was considered adequate in the present studies.

The equilibrium configurations of ketene, determined from a number of basis sets are given in table 3.2, together with experimentally derived values, for the ground state (52), which are the only ones available.

Two of the experimental geometry parameters, the CC and CO bond length are not well defined because the central atom lies close to the molecular centre of mass. However, as Herzberg indicated (3), the sum of the two bondlengths is precisely determined and Moore and Pimentel (52) obtained an  $r_0(\text{CCO})$  value of  $2.475\text{\AA}$ .

The split-valence basis sets consistently predict a CH bondlength of ca.  $1.068\text{\AA}$  which is about  $0.01\text{\AA}$  shorter than

the experimental  $r_{\text{O}}$  of  $1.079\text{\AA}$ . Inclusion of polarisation tends to increase the theoretical bondlength to around  $1.070\text{\AA}$ . The STO-3G CH bondlength of Pouchan et al. (62) is somewhat longer at  $1.075\text{\AA}$ , whilst the DZ CH bondlength of Dykstra and Schaefer (76) is similar to that of the 6-31G\*\*.

Table 3.2. Comparison of ab initio and experimental geometries<sup>a</sup> of ketene.

	r(CH)	r(CC)	r(CO)	r(CCO)	$\alpha(\text{HCH})$
4-21G	1.0683	1.2948	1.1625	2.4573	119.93
4-31G	1.0682	1.2976	1.1637	2.4613	119.81
5-31G	1.0682	1.3028	1.1656	2.4684	119.96
6-31G	1.0685	1.3038	1.1661	2.4699	120.00
6-31G**	1.0704	1.3064	1.1437	2.4501	121.71
STO-3G	1.075	1.300	1.183	2.483	119.5
DZ	1.070	1.311	1.171	2.482	120.07
DZ+P	-	-	-	-	122.0
Experimental	1.079	1.314	1.161	2.475	122.3

<sup>a</sup> Bondlengths in  $\text{\AA}$  ( $\text{\AA} \equiv 10^{-10}\text{m}$ ) and bond angles in degrees.

A different trend is found for the CC bondlength. An increase in the number of basis core functions results in a corresponding increase in the CC bondlength, up to  $1.303\text{\AA}$  for the 6-31G basis set. The effect of polarisation is to

lengthen the bond even more to  $1.306\text{\AA}$ . However, this is still nearly  $0.01\text{\AA}$  shorter than the experimental CC value of  $1.314\text{\AA}$ . A similar effect arising from the introduction of polarisation has been found for ethylene, where an increase in the CC bondlength of roughly the same amount is found. The STO-3G CC bondlength of  $1.300\text{\AA}$  is similar to those from the split-valence basis sets. However, the DZ CC bondlength of  $1.311\text{\AA}$  is considerably closer to the experimental CC value which probably results from a more complete description of the basis core functions.

The CO bondlengths of ca.  $1.16\text{\AA}$  determined from the split-valence basis sets are fairly consistent, varying by only  $0.0036\text{\AA}$  and are close to the experimental CO value of  $1.161\text{\AA}$ , but are considerably shorter than those of the STO-3G and DZ. By inclusion of polarisation functions, the CO bondlength substantially decreases by almost  $0.02\text{\AA}$  to  $1.144\text{\AA}$ . Similar trends have also been found for the CO bonds of formaldehyde and  $\text{CO}_2$  (36) where the decrease in the CO bondlength is about  $0.02\text{\AA}$  and  $0.015\text{\AA}$  respectively.

By comparison of the CCO bondlength sums in table 3.2, it is found that the split-valence basis sets are all less than the experimental value and inclusion of polarisation functions results in an even greater underestimation. The STO-3G CCO bondlength sum is somewhat closer to, though larger than that of the  $r_0$  structure (52). The DZ CCO bondlength is in closest agreement with experiment although it is also an overestimate.

The split-valence HCH angles are fairly consistent, ranging from  $119.8^\circ$  to  $120.0^\circ$ , but are considerably less than the  $r_o$  value of  $122.3^\circ$ . The DZ HCH angle is similar to that of the split-valence basis sets whilst the STO-3G angle of  $119.5^\circ$  is poorer. Inclusion of polarisation functions however results in a substantial increase in the HCH angle by ca.  $1.7^\circ$  and hence better agreement with experiment. Dykstra (77) found similar effects in his studies of the energies of isomers of ketene, where a DZ basis set supplemented with d-type polarisation functions (DZ+P) was used. His HCH angle of  $122.0^\circ$  agrees rather better with the experimental value than that of the 6-31G\*\*. (Nb. Dykstra did not quote any bondlengths for the DZ+P basis set.)

The total energies associated with the theoretical equilibrium configurations for split-valence and polarisation included basis sets as well as the DZ and DZ+P are given in table 3.3. The total energy associated with the STO-3G equilibrium was not quoted by Pouchan et al. (62), but is expected to be higher than that of the other basis sets considered here. From table 3.3, it can be seen that the split-valence energies improve as the number of basis functions increase. It can also be seen that the DZ basis set is roughly equivalent to a 6-31G whilst a DZ+P is about the same as a 6-31G\*\*.

From table 3.2, it can be seen that deviations of the split-valence equilibrium geometries from the experimental  $r_o$  structure are fairly systematic. Such systematic

deviations were also found by Pulay et al. (36) for a wide range of small molecules. As a result, for force constant calculations, these authors recommended empirical correction of the ab initio geometry. Their corrections were made in terms of a set of small reference molecules and apply to the 4-21G basis set. Similar scaling was practised by Blom and Altona for the 4-31G basis set (46,78-83). In addition to these, several larger basis sets including, the 6-31G and 6-31G\*\*, were also employed. Comprehensive studies of geometry trends for these larger basis sets were not available<sup>+</sup> and thus empirical corrections to the theoretical geometries derived from these could not be established. Furthermore, the accuracy of such corrections to the theoretical geometry of ketene perhaps have to be treated with caution, because of the unusual adjacent double bond structure present.

Table 3.3. Total ab initio energies for ketene, Hartree.

Basis	Energy + 151
4-21G	-0.3736
4-31G	-0.4949
5-31G	-0.6176
6-31G	-0.6493
6-31G**	-0.7302
DZ	-0.6724
DZ+P	-0.7556

<sup>+</sup> Since the time of writing, both published and unpublished molecular geometry data have been brought together for larger basis sets in "Ab Initio Molecular Orbital Theory" by Hehre, Radon, Schleyer and Pople, Wiley (1986).

The ab initio quadratic force constants of ketene are given in table 3.4. These were calculated from the 4-21G (36), 4-31G (34), 5-31G (35), 6-31G (35) and 6-31G\*\* (41) basis sets. For the most part, the reference geometry was taken to be the theoretical minima (columns 1 to 5), though calculations were repeated for some basis sets at other geometries. Specifically, the 6-31G and 6-31G\*\* force fields were also determined at the experimental  $r_0$  structure (52) (columns 6 and 7) and the 4-21G force constants were also evaluated around an empirically corrected theoretical geometry (column 8). The latter geometry was obtained by adjusting the 4-21G theoretical geometry in terms of the corrections given in table IV of reference (36).

All the force constants were determined by numerical followed by analytical differentiation of the molecular energy in terms of the symmetry coordinates (45) (see also section 1.3.5) of table 3.1. For columns 1 to 8, the quadratic and dominant cubic force constants were evaluated in terms of the two-sided distortion expressions 1.43 and 1.44. The distortions were taken to be  $\pm 0.05\text{\AA}^\circ$  for stretching coordinates and  $\pm 0.04\text{rad}$  for bending coordinates, in accordance with recommendations of Fogarasi and Pulay (12). The 4-21G'/corr.  $A_1$  force constants of column 9 were determined by a more elaborate method in which internal forces for several distortions were fitted to cubic terms of polynomials. This method has the advantage over the

Table 3.4. Ab initio quadratic force constants<sup>a</sup> for ketene determined from split-valence basis sets around various reference geometries.

$F_{ij}$	4-21G/ 4-21G	4-31G/ 4-31G	5-31G/ 5-31G	6-31G/ 6-31G	6-31G**/ 6-31G**	6-31G/ Expt	6-31G**/ Expt	4-21G <sup>b</sup> /Corr <sup>b</sup>	4-21G <sup>c</sup> /Corr <sup>b,c</sup>
$F_{11}$	6.460	6.483	6.520	6.522	6.465	6.146	6.165	6.204	6.165
$F_{12}$	0.139	0.129	0.116	0.116	0.133	0.134	0.143	0.139	0.139
$F_{13}$	-0.095	-0.083	-0.074	-0.074	-0.085	-0.073	-0.084	-0.093	-0.094
$F_{14}$	0.045	0.047	0.044	0.044	0.045	0.030	0.043	0.050	0.050
$F_{22}$	11.51	11.61	11.37	11.34	10.990	10.667	10.495	10.072	9.951
$F_{23}$	0.937	0.947	0.954	0.951	1.276	0.973	1.226	0.951	0.950
$F_{24}$	-0.432	-0.415	-0.416	-0.416	-0.351	-0.418	-0.349	-0.430	-0.430
$F_{33}$	17.50	17.25	16.84	16.760	19.811	17.353	17.537	18.068	17.772
$F_{34}$	0.008	0.009	0.008	0.008	-0.002	0.007	-0.002	0.011	0.010
$F_{44}$	0.763	0.755	0.752	0.751	0.710	0.739	0.703	0.756	0.756
$F_{55}$	0.782	0.694	0.727	0.707	0.811	0.707	0.779	0.783	
$F_{56}$	0.089	0.086	0.091	0.091	0.105	0.094	0.106	0.098	
$F_{66}$	0.205	0.211	0.215	0.215	0.147	0.224	0.150	0.188	
$F_{77}$	6.391	6.434	6.485	6.489	6.404	6.124	6.105	6.137	
$F_{78}$	-0.383	-0.354	-0.356	-0.344	-0.284	-0.348	-0.284	-0.360	
$F_{79}$	0.004	0.004	0.006	0.006	0.013	0.007	0.011	0.004	
$F_{88}$	1.064	1.060	1.098	1.076	0.927	1.107	0.927	1.106	
$F_{89}$	-0.211	-0.208	-0.209	-0.209	-0.226	-0.209	-0.223	-0.183	
$F_{99}$	0.786	0.719	0.730	0.727	0.778	0.732	0.758	0.817	

<sup>a</sup> Units are consistent with energy measured in aJ (aJ  $\equiv$  mdyne<sup>0</sup>), stretching coordinates in A<sup>0</sup> (A<sup>0</sup>  $\equiv$  10<sup>-10</sup>m) and bendings in radians.

<sup>b</sup> Empirically corrected theoretical geometry of Pulay et al. (36).

<sup>c</sup> Force constants determined by multi-distortion analyses.

two-sided distortion approach that it takes the dominant quartic force constant contributions into account but suffers from numerical inaccuracies affecting such higher derivatives, particularly if larger distortions are used (34). Thus, in the stretching coordinates and deformation coordinates, distortions of not more than  $0.05\text{\AA}^\circ$  and  $0.04\text{rad}$  were used. A second disadvantage of this method is that a larger number of calculations are required therefore force constant evaluation times are considerably longer.

The most striking overall feature of table 3.4 is that the force constants are of remarkable consistency, particularly with regard to the sign and magnitude of the interaction constants. Surprisingly, the force constants seem on the whole to be comparatively insensitive to the reference geometry used. By comparing the force constants calculated around different geometries (4-21G/4-21G and 4-21G/corr; 6-31G/6-31G and 6-31G/Expt; 6-31G\*\*/6-31G\*\* and 6-31G\*\*/Expt), it can be seen that the main effects are on the diagonal force constants. These have an inverse relationship with their corresponding geometry parameters, and the most pronounced example of this may be seen in the 6-31G\*\* CO bondlength, where adoption of the experimental geometry causes a decrease of more than  $2\text{mdyn}\text{\AA}^{\circ-1}$  in the corresponding  $F_{33}$  diagonal constant.

The main effect of the inclusion of polarisation terms seems to be to increase substantially the  $F_{33}$  CO (stretch) and  $F_{23}$  CC (stretch) / CO (stretch) constants whilst causing

a smaller decrease in the  $F_{22}$  CC (stretch). Again, the changes in the  $F_{22}$  and  $F_{33}$  diagonals can be reasoned in terms of the effects of polarisation on the geometry. From section 3.3.3, it was seen that inclusion of polarisation caused a slight increase in the CC bondlength and a large decrease in the CO bondlength. This almost certainly causes the small decrease and large increase in the  $F_{22}$  and  $F_{33}$  constants respectively. The  $F_{23}$  constant will be discussed later.

A second notable effect of polarisation is to decrease markedly the  $F_{66}$   $\text{CH}_2$  wag in relation to the other  $B_1$  constants. Although the absolute change is only about 0.05mdyn, this represents approximately a 30% decrease in the value of the constant.

By comparison of the 4-21G force fields around a common empirically corrected theoretical geometry from the two-sided distortion and multi-distortion methods (columns 8 and 9), it is found that the discrepancies are minimal. This indicates that the two-sided distortion method for obtaining force constants is sufficiently accurate for the present purposes.

The cubic diagonal and semi-diagonal force constants obtained from the 6-31G and 6-31G\*\* basis sets around both theoretical and experimental geometries are given in table 3.5. Here, it may be seen that the cubic force constants are very consistent, though less so than the quadratic

Table 3.5. 6-31G and 6-31G\*\* diagonal and semi-diagonal cubic force constants<sup>a</sup> determined around theoretical and experimental geometries.

$F_{ijj}$	6-31G/ 6-31G/	6-31G/ Expt.	6-31G**/ 6-31G**	6-31G**/ Expt.
$F_{111}$	-26.0	-24.6	-25.3	-24.2
$F_{112}$	0.276	0.280	0.244	0.228
$F_{113}$	-0.001	0.029	0.031	0.007
$F_{114}$	-0.095	-0.121	-0.080	-0.081
$F_{221}$	0.138	0.163	0.224	0.215
$F_{222}$	-66.2	-63.1	-64.2	-61.8
$F_{223}$	-0.096	-0.008	-0.771	-0.584
$F_{224}$	-0.245	-0.322	-0.446	-0.469
$F_{331}$	-0.020	-0.017	-0.015	-0.008
$F_{332}$	-2.75	-2.74	-2.77	-2.64
$F_{333}$	-115.0	-118.4	-135.1	-122.7
$F_{334}$	-0.039	-0.050	-0.004	-0.006
$F_{441}$	-0.472	-0.389	-0.330	-0.332
$F_{442}$	-0.188	-0.100	0.025	0.037
$F_{443}$	-0.073	-0.035	-0.058	-0.091
$F_{444}$	-0.125	-0.145	-0.172	-0.169
$F_{551}$	-0.041	-0.041	-0.026	-0.027
$F_{552}$	-1.24	-1.23	-1.30	-1.23
$F_{553}$	-1.36	-1.36	-1.19	-1.10
$F_{554}$	0.014	0.015	0.023	0.024
$F_{661}$	-0.196	-0.182	-0.129	-0.142
$F_{662}$	-0.773	-0.758	-0.635	-0.662
$F_{663}$	0.245	0.254	0.286	0.291
$F_{664}$	0.496	0.522	0.388	0.396
$F_{771}$	-26.5	-25.0	-25.6	-24.5
$F_{772}$	0.315	0.358	0.307	0.289
$F_{773}$	0.053	0.063	0.088	0.090
$F_{774}$	0.311	0.262	0.278	0.271
$F_{881}$	-0.342	-0.288	-0.252	-0.262
$F_{882}$	0.019	0.125	0.359	0.345
$F_{883}$	-0.159	-0.141	-0.145	-0.136
$F_{884}$	0.410	0.388	0.315	0.314
$F_{991}$	0.030	0.031	0.026	0.023
$F_{992}$	-0.783	-0.775	-0.746	-0.686
$F_{993}$	-0.949	-0.948	-0.824	-0.770
$F_{994}$	0.004	0.003	0.001	0.002

<sup>a</sup> For units, see footnote <sup>a</sup> to table 3.4.

constants. Cubic constants determined from the other quoted basis sets of table 3.4 are very similar, generally agreeing to within 5% or 0.15 of their absolute magnitude. The most marked changes are found in the  $F_{333}$  CO and  $F_{223}$  CC/CC/CO constants, where the inclusion of polarisation functions causes a numerical decrease of up to  $\sim 17 \text{mdynA}^{0-2}$  and  $\sim 0.75 \text{mdynA}^{0-2}$  respectively. The corresponding quadratic constants  $F_{33}$  and  $F_{23}$  were found to be very sensitive to polarisation functions above. Curiously, this sensitivity seems not to be reflected in the rather large  $F_{332}$  CO/CO/CC constant which remains essentially unaltered over all the studied basis sets and geometries.

The diagonal quartic stretch force constants determined from the multi-distortion analysis are given in table 3.6. These figures are subject to inherent numerical errors and should be treated with caution.

Table 3.6. Quartic diagonal force constants<sup>a</sup> obtained from multi-distortion analysis using a 4-21G basis set and empirically corrected geometry.

---

$F_{1111}$	+91
$F_{2222}$	+287
$F_{3333}$	+674
$F_{4444}$	+2.2

---

<sup>a</sup> For units, see footnote <sup>a</sup> of table 3.4.

From tables 3.4 and 3.5, it was seen that the quadratic and dominant cubic constants are internally consistent. However, this does not necessarily infer an assurance of accuracy. Generally, the reliability of the force constants has been judged from comparison with experimental force constants (when available). For most molecules, it has been found that agreement is good, though ab initio constants are systematically overestimated at the SCF level, generally by as much as 20%. One noteworthy exception to this is CO<sub>2</sub>, where the neglect of electron correlation results in an ab initio CO/CO interaction constant much larger than a well defined experimental value (85-87). Inclusion of polarisation functions was found to have a detrimental effect on the constant (86). It was therefore anticipated that the CC/CO interaction constant of ketene would probably be similarly overestimated for the same reason at the SCF level.

The reliability of the ab initio force fields for ketene can at least be partially gauged by comparing some of the force constants with their ethylene equivalents. Recently, Fogarasi and Pulay (68) found that their ab initio force constants for ethylene, obtained from TEXAS, were generally in excellent agreement with accurate experimental values determined by Duncan and Hamilton (69). The largest basis set which Fogarasi and Pulay used was a 6-31G\*\* and their force constants were calculated around an empirically corrected (4-21G) theoretical geometry (which is close to the experimentally estimated  $r_e$  structure (89)). These

constants are best compared with the 6-31G\*\*/Expt force constants of ketene. The two sets of comparable constants are given in table 3.7 (below), where it can be seen that they are quite similar.

Table 3.7. Comparison of 6-31G\*\* analogous quadratic constants<sup>a</sup> of ketene and ethylene using coordinate definitions of table 3.1.

	Ketene	Ethylene
CH <sub>2</sub> sym str	6.165	6.171
CC str	10.495	10.545
CH <sub>2</sub> def	0.703	0.818
CH <sub>2</sub> wag	0.150	0.337
CH <sub>2</sub> asym str	6.105	6.100
CH <sub>2</sub> rock	0.927	1.270
CH <sub>2</sub> sym str/CC str	0.143	0.139
CH <sub>2</sub> sym str/CH <sub>2</sub> def	0.043	0.120
CC str/CH <sub>2</sub> def	-0.349	-0.269
CH <sub>2</sub> asym str/ CH <sub>2</sub> rock	-0.223	-0.276

<sup>a</sup> For units, see footnote <sup>a</sup> to table 3.4.

There is complete agreement with regard to sign and also, all stretch and stretch/stretch constants are in close numerical agreement. The larger  $\text{CH}_2$  bending constants for ethylene are consistent with the vibrations occurring at higher frequency than in ketene, particularly in the case of the wag. As well as determining quadratic force constants for ethylene, Fogarasi and Pulay also evaluated cubic constants from the 6-31G\*\* basis set (68), though this time at the theoretical equilibrium. Their CC and  $\text{CH}_2$  stretch diagonals of  $-56.1\text{mdynA}^{\text{O}-2}$  and  $-32.7\text{mdynA}^{\text{O}-2}$  are in fairly good agreement with the corresponding values of  $-64.2\text{mdynA}^{\text{O}-2}$  and  $-25.3\text{mdynA}^{\text{O}-2}$  respectively for ketene.

The ab initio force fields determined here from split-valence contracted gaussian functions are compared with the only previous ab initio force field study of Pouchan et al. (62), and with the experimental force field of Mallinson and Nemes (59) in table 3.8. Since the ab initio force fields of table 3.4 are essentially the same for all basis sets, for clarity only those obtained from the largest (and therefore most accurate) - 6-31G\*\*/6-31G\*\* and 6-31G\*\*/Expt - are included in table 3.8. Although both the split-valence and STO-3G minimal basis set force fields are in general qualitative agreement (with the exception of  $F_{89}$  rock/in-plane CCO bend), the former are in much closer quantitative agreement with the experimental force field particularly with regard to the interaction force constants. Specifically, the  $F_{34}$  CO/ $\text{CH}_2$  (symmetric) def(ormation) and  $F_{79}$   $\text{CH}_2$  asym(metric) str/in-plane CCO bend which were

Table 3.8. Comparison of the Mallinson and Nemes experimental force constants<sup>a</sup> for ketene with those predicted from STO-3G, 6-31G\*\*/6-31G\*\* and 6-31G\*\*/Expt.

$F_{ij}$	M&N(59)	STO-3G(62)	6-31G** /6-31G**	6-31G** /Expt
$F_{11}$	6.080(105)	7.63	6.465	6.165
$F_{12}$	1.590(296)	0.227	0.133	0.143
$F_{13}$	[0.000] <sup>b</sup>	-0.216	-0.085	-0.084
$F_{14}$	[0.176] <sup>c</sup>	0.050	0.045	0.043
$F_{22}$	9.219(955)	13.28	10.990	10.495
$F_{23}$	0.515(478)	0.344	1.276	1.226
$F_{24}$	-0.288(34)	-0.361	-0.351	-0.349
$F_{33}$	15.28(155)	19.17	19.811	17.537
$F_{34}$	[0.000] <sup>b</sup>	0.100	-0.002	-0.002
$F_{44}$	0.613(13)	0.862	0.710	0.703
$F_{55}$	0.681(8)	0.797	0.811	0.779
$F_{56}$	0.101(4)	0.156	0.105	0.106
$F_{66}$	0.093(2)	0.316	0.147	0.150
$F_{77}$	5.754(25)	7.74	6.404	6.105
$F_{78}$	-0.098(262)	-0.289	-0.284	-0.284
$F_{79}$	[0.000] <sup>b</sup>	0.037	0.013	0.012
$F_{88}$	0.708(24)	1.262	0.927	0.927
$F_{89}$	-0.204(8)	0.141	-0.226	-0.223
$F_{99}$	0.696(24)	0.696	0.778	0.760

<sup>a</sup> For units see footnote <sup>a</sup> of table 3.4.

<sup>b</sup> Constrained to the value quoted.

<sup>c</sup> Constrained to hybrid orbital model prediction -  
 $F_{14} = 0.029F_{11}$  (61).

constrained to zero in the experimental force field, are predicted to be close to zero by the ab initio force fields. In addition, the ab initio  $F_{11}/F_{77}$  sym/asym  $\text{CH}_2$  stretch ratio is in close accord with that of Mallinson and Nemes (59).

There are a few noteworthy discrepancies between the 6-31G\*\* and the Mallinson and Nemes (59) experimental force fields particularly in the  $A_1$  block. Most importantly, the empirical  $F_{12}$   $\text{CH}_2$  sym str/CC constant is some 10 times that predicted by ab initio calculations. From table 3.7, it may be seen that the ab initio  $\text{CH}_2$  sym str/CC constant for ethylene is about the same magnitude as that for ketene. Although a somewhat larger  $\text{CH}_2$  sym str/CO constant for formaldehyde has been found (by both ab initio and experimental studies (89)), it is anticipated that the Mallinson and Nemes  $F_{12}$  is a serious overestimation. From table 3.8 it may also be seen that the ab initio  $F_{13}$   $\text{CH}_2$  sym str/CO constant of ca.  $-0.08\text{mdynA}^{-1}$  is considerably removed from zero, to which it was constrained by Mallinson and Nemes (59). The  $F_{23}$  CO/CC constant of the experimental force field is about one half of the value of that predicted from the 6-31G\*\* (or any other split-valence) basis set. Despite the fact that the experimental constant is barely determined, it is considered that the ab initio constant is seriously overestimated, as has been found for the analogous CO/CO interaction force constant of  $\text{CO}_2$  (86-88), unless electron correlation is included in the calculations, as discussed above. Other discrepancies between the empirical

and ab initio force fields may be found in the  $B_1$  and  $B_2$  force constants. There is a difference in magnitude of the  $F_{78}$  constant by a factor of 3. Here, however, the Mallinson and Nemes constant not effectively determined, being subject to a very large uncertainty. Comparison of the  $F_{55}$  out-of-plane CCO bend and  $F_{99}$  in-plane CCO bend constants indicates that the former is the smaller empirical constant, whilst the latter is the smaller ab initio constant. Since the corresponding  $\nu_5$  vibration is found to lie at a higher frequency than  $\nu_9$  then intuitively, one would expect the  $F_{55}$  constant to be larger. More seriously, the  $F_{66}$  wag is considerably overestimated by ab initio calculations. The  $B_1$  vibrations are very sensitive to small changes in any of the three  $B_1$  force constants and since a similar overestimation is not found for the  $F_{56}$  out-of-plane CCO bend/wag constant, then it was anticipated that ab initio vibrational predictions for the  $B_1$  constants (see section 3.5) might be in considerable error.

### 3.4 EMPIRICAL HARMONIC FORCE FIELD OF KETENE

#### 3.4.1 EXPERIMENTAL DATA AND THEIR ASSESSMENT

##### (a) Vibration frequencies

An investigation of the high resolution infrared spectra of a number of fundamental and overtone vibrations in chapter 2 has demonstrated that severe perturbations are present in almost all fundamental vibrations. The determined band origins for the totally symmetric ( $A_1$ ) vibrations are subject to Fermi resonance displacements and/or inaccuracies arising from a-axis Coriolis resonances, which are particularly severe due to the large magnitude of the A rotational constant. Either effect usually leads to irregularity in the observed subband origins such that the location of accurate vibration frequency is difficult. Of all the  $A_1$  vibrations studied, it would appear that only the  $\nu_1$  ( $CD_2$  symmetric stretch) of  $D_2CCO$  is essentially unperturbed.

Such inaccuracies in the absolute values of the frequencies are generally not of crucial importance to force constant calculations unless frequency shifts are being used. It was hoped that the availability of the spectra of  $H_2C^{13}CO$  and  $H_2^{13}CCO$  would yield valuable data for the determination of the 10  $A_1$  species force constants. The perturbations of the spectra however, render the  $^{13}C$  frequency shifts on  $\nu_1$  and  $\nu_3$  of only limited value, whilst

those on  $\nu_4$  are totally useless.

The effects of the very large a-axis Coriolis perturbations in the four lowest vibrations  $\nu_5$ ,  $\nu_6$ ,  $\nu_8$  and  $\nu_9$  also create difficulties as has been demonstrated by Nemes (54). Here however, accurate  $^{13}\text{C}$  frequency shifts were determined by careful measurement of the displacements of equivalent Q branch features in the spectra, since the  $K_a$ -dependent perturbations are zero at subband  $P_{Q_1}$ . A recent analysis of the low frequency region of  $\text{D}_2\text{CCO}$  has located the vibrations accurately (56).

The asymmetric  $\text{CH}_2$  stretch,  $\nu_7$  is in strong Fermi resonance with  $\nu_2 + \nu_8$  in  $\text{H}_2\text{CCO}$  as has been shown by Johns et al (55). In this case, the data available for  $\text{H}_2\text{CCO}$ ,  $\text{H}_2\text{C}^{13}\text{CO}$  and  $\text{H}_2^{13}\text{CCO}$  was analysed in terms of related resonance interaction constants to yield unperturbed frequency data.

A summary of the resonance interactions established for the fundamentals of the  $\text{H}_2\text{CCO}$  and  $\text{D}_2\text{CCO}$  species and their effect on the reliability of the data towards the determination of the potential function is given in table 3.9.

#### (b) Coriolis Interaction Constants

Only for the  $\nu_5$ ,  $\nu_6$ ,  $\nu_8$  and  $\nu_9$  system of  $\text{H}_2\text{CCO}$  have Coriolis interaction constants,  $\zeta_{ij}$ , been determined directly from spectroscopic analysis by Nemes (54). The

Table 3.9. Resonance interactions identified in  $\text{H}_2\text{CCO}$  species and in  $\text{D}_2\text{CCO}$ , and their effect on frequency data.

Fundamental	Interacting level(s)	Type of interaction	Effect on data
$\text{H}_2\text{CCO}$ species			
$\nu_1$	$\nu_4 + 2\nu_8$	Fermi	$\Delta\nu_1$ poor
$\nu_2$	$\nu_4 + \nu_5 + \nu_9$	Coriolis	$\Delta\nu_2$ good
$\nu_3$	$\nu_8 + \nu_9$	Fermi	$\Delta\nu_3$ poor
$\nu_4$	$2\nu_5, \nu_5 + \nu_6, 2\nu_6$	Fermi	$\nu_4$ poor, $\Delta\nu_4$ useless
$\nu_5$	$\nu_8, \nu_9$	Coriolis	$\Delta\nu_5$ good
$\nu_6$	$\nu_8, \nu_9$	Coriolis	$\Delta\nu_6$ good
$\nu_7$	$\nu_2 + \nu_8$	Fermi	$\Delta\nu_7$ good (analysed)
$\nu_8$	$\nu_5, \nu_6$	Coriolis	$\Delta\nu_8$ good
$\nu_9$	$\nu_5, \nu_6$	Coriolis	$\Delta\nu_9$ unknown
$\text{D}_2\text{CCO}$ species			
$\nu_1$	-	Unperturbed	
$\nu_2$	$\nu_3 + 2\nu_6, \nu_3 + \nu_5 + \nu_9$	Fermi/Coriolis	
$\nu_3$	$\nu_8 + \nu_9$	Fermi	
$\nu_4$	$2\nu_5, \nu_5 + \nu_6, 2\nu_6$	Fermi	$\nu_4$ poor
$\nu_5$	$\nu_8, \nu_9$	Coriolis	
$\nu_6$	$\nu_8, \nu_9$	Coriolis	
$\nu_7$	-	?Unperturbed	
$\nu_8$	$\nu_5, \nu_6$	Coriolis	
$\nu_9$	$\nu_5, \nu_6$	Coriolis	

recent analysis of the corresponding system in  $D_2CCO$  (56) fits a large number of rovibration transitions in terms of excited state constants with the Coriolis interactions treated explicitly in terms of the values predicted by force constants of Mallinson and Nemes (59). For  $H_2CCO$  Nemes determined two constants to be large and two to be much smaller (54). The former produce the predominant perturbations, which are approximately proportional to  $\zeta_a^2 K_a^2$ . It is found that the two larger constants are useful parameters in the calculations, but that the two smaller constants are apparently poorly determined by the available spectroscopic information.

#### (c) Quartic Distortion Constants

Fourteen constants are available from microwave or combined microwave-infrared analysis of the ground state for  $H_2CCO$  (55),  $HDCCO$  and  $D_2CCO$  (91). It was hoped that these would be of considerable assistance in improving the definition of the force field. However, they were found to be mutually incompatible, both within a single isotopic species and between isotopic species. Basically reasonable fits to combinations of up to four constants could be achieved but only at the expense of extremely poor fits to the remainder. In a recent reanalysis of the ground state microwave and infrared data (92), it was concluded that the literature values of  $A_J^0$ ,  $A_{JK}^0$  and  $\delta_J^0$  were reliable to about 5%,  $\delta_K^0$  to about 10% (but less so for  $H_2CCO$ ) and  $A_K^0$  to about 15% for the  $H_2CCO$ ,  $HDCCO$  and  $D_2CCO$  species, as far

as force constant calculations are concerned.

A total of 58 data comprising 27 frequencies, 13 frequency shifts, 4 Coriolis constants and 14 distortion constants over 5 isotopic species of ketene were thus available for use in the force field refinement.

#### 3.4.2 ANHARMONICITY CORRECTIONS

Frequency and shift data corrected for Fermi resonance where necessary were harmonized in terms of Dennison's rule (equations 1.30 and 1.31). For vibrational modes not involving the oxygen atom,  $H_2CCO$  anharmonicity constants are those used for ethylene, viz 0.045 for CH stretching, 0.020 for CH bending and 0.015 for CC stretching. In previous studies Mallinson and Nemes (59) assumed a value of 0.010 for the CCO bending mode. This is adopted here. For the CO stretching mode, these authors used the anharmonicity constant found for the corresponding formaldehyde mode. Here, however, it is considered that the CC and CO anharmonicity constants should be the same since major coupling must be occurring between the two modes. Therefore, a value of 0.015 is also adopted for the CO stretching mode.

Listed in table 3.10 are the product rule ratios obtained from the observed, harmonized and calculated frequencies of the  $H_2CCO$ ,  $HDCCO$  and  $D_2CCO$  isotopomers. It may be seen from table 3.10 that only the  $A_1 D_2CCO/H_2CCO$

product rule ratio discrepancy is satisfactorily removed on harmonizing the observed data (though it must be remembered that the  $\nu_4$  frequencies for both these species are quite uncertain).

Table 3.10. Observed, "harmonized" and theoretical product rule ratios for ketene and deuteroketenes.

		OBS	HARM	THEORY
$D_2CCO/H_2CCO$	$A_1$	0.5321	0.5230	0.5122
	$B_1$	0.7581	0.7547	0.7693
	$B_2$	0.5548	0.5463	0.5516
$HDCCO/H_2CCO$	$A'$	0.5393	0.5306	0.5327
	$A''$	0.8890	0.8874	0.8922

The  $D_2CCO/H_2CCO$   $B_2$  and  $HDCCO/H_2CCO$   $A'$  product rule ratios indicate over-correction by harmonizing. More seriously, the calculated  $D_2CCO/H_2CCO$   $B_1$  and the corresponding  $HDCCO/H_2CCO$   $A''$  ratios are considerably larger than those observed. Mallinson and Nemes (59) found a similar  $B_1$   $D_2CCO/H_2CCO$  "overshoot" and attributed it to an incorrect band origin in either species. The  $D_2CCO$   $\nu_5$  and  $\nu_6$  frequencies have more recently been accurately determined and this implies that the inaccuracies most likely lie in the  $H_2CCO$  species. However, removal of the overshoot

requires reassignment of either  $\nu_5$  or  $\nu_6$  by at least  $6\text{cm}^{-1}$ . This seems rather large. The product rule ratio discrepancy in this case could alternatively be accounted for in terms of negative anharmonicity associated with the out-of-plane vibrations. Further evidence of this has probably been found in the analysis of  $2\nu_5$  and  $2\nu_6$  in chapter 2, where the respective band origins were found to be at frequencies appreciably higher than those calculated from the corresponding fundamental frequencies.

Anharmonicity corrections to the Coriolis coupling constants and distortion constants could not be made since the effects of anharmonicity on these are not known. Thus the experimental values were used, with uncertainties which it was hoped would cover such effects.

### 3.4.3 UNCERTAINTIES ALLOWED IN DATA

The allowed uncertainties in the frequency data are 1% (but 2% on  $\nu_4$  data), which corresponds to an uncertainty of 0.010 in the anharmonicity constants. On the frequency shifts, this leads to an uncertainty of 2% of the observed shift on to which is added the experimental uncertainty in the estimate. The observed Coriolis constants for  $\text{H}_2\text{CCO}$  have been allowed uncertainties of between 0.10 and 0.30. Finally, for the distortion constants, uncertainties of 5% in  $\Delta_J^0$ ,  $\Delta_{JK}^0$ , 10% in  $\delta_J^0$ ,  $\delta_K^0$  and 20% in  $\Delta_K^0$  (and  $\delta_K^0$  for  $\text{H}_2\text{CCO}$ ) have been adopted. The experimental data, harmonized frequencies, frequency shifts and associated uncertainties

are collected in table 3.11.

#### 3.4.4 FORCE CONSTANT CALCULATIONS

At the outset, it was assumed that interaction force constants between symmetry coordinates with no common atoms should be constrained to zero. Thus  $F_{13}$  ( $\text{CH}_2$  sym str/CO) and  $F_{34}$  (CO/ $\text{CH}_2$  def) were set equal to zero. In addition,  $F_{79}$  ( $\text{CH}_2$  asym str/in-plane CCO bend) was set equal to zero since this force constant was undetermined by the accumulated data. The refinement thus became an attempt to determine 16 parameters in terms of the 58 data in table 3.11.

The  $^{13}\text{C}$  frequency shift data proved to be of great value in defining the  $B_1$  and  $B_2$  species force constants much more precisely than hitherto. However, for the  $A_1$  species, a wide variation in the resulting force constants could be achieved dependent upon which of the distortion constants one wished to reproduce most closely, it being impossible to fit all at once. The limited accuracy of the  $^{13}\text{C}$  frequency shift data did little to assist this problem which is demonstrated in table 3.12. The  $\Delta_J^{\circ}$ ,  $\Delta_{JK}^{\circ}$ ,  $\delta_J^{\circ}$  and  $\delta_K^{\circ}$  could be fitted rather well (column 1), but at the expense of very poor fits to  $\Delta_K^{\circ}$ ,  $\omega_1$ ,  $\omega_2$  and  $\Delta\omega_1$  data. This produced a very large  $F_{12}$  constant and corresponds to the result reported by Mallinson and Nemes (59). (The fact that  $F_{12}$  calculated here is not as large as that of the above authors is a consequence of the limited effect of the

Table 3.11. Observed frequency,  $^{13}\text{C}$  frequency shift, Coriolis  $\zeta^a$  and distortion constant data for isotopic ketenes<sup>a</sup>; harmonized frequency data, uncertainties and error vector produced by force constants of table 3.13.

	$\text{H}_2\text{CCO}$				$\text{HDCCO}$				$\text{D}_2\text{CCO}$			
	$\nu$	$\omega$	$\sigma_\omega$	$e$	$\nu$	$\omega$	$\sigma_\omega$	$e$	$\nu$	$\omega$	$\sigma_\omega$	$e$
$\nu_1$	3070.4	3215.0	32	2.3	2318.9	2400.5	24	-1.6	2267.2	2345.2	23	-0.8
$\nu_2$	2152.6	2185.3	22	4.9	2142.4	2174.7	22	2.2	2120.5	2152.3	22	-8.1
$\nu_3$	1387.5	1415.8	14	-8.8	1292	1316.5	13	-3.6	1225	1247.0	12	9.0
$\nu_4$	(1116.0)	(1133.0)	23	-3.9	(1084.9)	(1101.0)	22	-0.7	(924.7)	(936.4)	19	10.0
$\nu_5$	587.3	593.2	5.9	1.9	555.3	560.6	5.6	-0.8	541.2	546.1	5.5	-8.3
$\nu_6$	528.4	539.2	5.4	2.8	496.8	506.3	5.1	2.3	434.7	442.0	4.4	1.9
$\nu_7$	3158.7	3307.5	33	4.0	3117.3	3261.8	32	0.1	2383.3	2467.1	25	-2.4
$\nu_8$	977.8	997.8	10	0.4	867.1	882.7	8.8	-0.6	851.7	866.8	8.7	-0.3
$\nu_9$	439.0	443.4	4.4	1.4	397.6	401.6	4.0	0.9	370.6	373.8	3.7	-1.2
	$\Delta$	$\sigma_\Delta$	$e$		$\Delta$	$\sigma_\Delta$	$e$		$\Delta$	$\sigma_\Delta$	$e$	
$\Delta_{\text{J}}^\circ$	3.39	0.17	0.006		3.21	0.16	0.006		2.72	0.14	0.040	
$\Delta_{\text{JK}}^\circ$	476.0	24	-13		327.0	16.5	-8.8		321.7	16	-5.9	
$\Delta_{\text{K}}^\circ$	23535	4700	3170		(15000)	$\infty$	[14370] <sup>b</sup>		5391	1100	635	
$\delta_{\text{J}}^\circ$	0.145	0.014	0.012		0.225	0.022	0.016		0.218	0.022	0.015	
$\delta_{\text{K}}^\circ$	329.6	66	58		239.0	24	14.5		212.7	21	23.0	

Table 3.11. (continued)

	H <sub>2</sub> CCO			HDCCO			D <sub>2</sub> CCO		
	$\zeta$	$\sigma_{\zeta}$	e	$\zeta$	$\sigma_{\zeta}$	e	$\zeta$	$\sigma_{\zeta}$	e
$\zeta_{58}$	0.33	0.3	0.21	-	-	[0.60]	-	-	[0.76]
$\zeta_{68}$	0.71	0.1	-0.005	-	-	[0.42]	-	-	[0.26]
$\zeta_{59}$	0.77	0.1	0.05	-	-	[0.75]	-	-	[0.64]
$\zeta_{69}$	0.30	0.1	-0.12	-	-	[0.11]	-	-	[0.35]
	H <sub>2</sub> <sup>13</sup> CCO				H <sub>2</sub> C <sup>13</sup> CCO				
	$\Delta\nu$	$\Delta\omega$	$\sigma_{\Delta\omega}$	e	$\Delta\nu$	$\Delta\omega$	$\sigma_{\Delta\omega}$	e	
$\Delta\nu_1$	5.6	6.1	1.0	0.57	0.1	0.1	0.2	0.06	
$\Delta\nu_2$	5.36	5.52	0.3	-0.02	56.6	58.3	1.4	-0.98	
$\Delta\nu_3$	12.4	12.9	1.0	-0.18	-	-	-	[0.04]	
$\Delta\nu_4$	(5.2)	(5.4)		[16.8]	(7.9)	(8.1)		[0.84]	
$\Delta\nu_5$	0.37	0.38	0.1	0.03	5.40	5.51	0.1	0.06	
$\Delta\nu_6$	5.52	5.79	0.2	0.20	9.68	10.09	0.1	0.04	
$\Delta\nu_7$	13.6	14.82	1.0	0.68	0.0	0.00	0.2	0.00	
$\Delta\nu_8$	7.80	8.14	0.1	0.11	10.44	10.97	0.1	0.05	
$\Delta\nu_9$	-	-	-	[0.05]	-	-	-	[7.55]	

<sup>a</sup> Frequency data in cm<sup>-1</sup>, distortion constants in kHz,  $\zeta$  constants dimensionless.

<sup>b</sup> Entries in square brackets are calculated values.

Table 3.12. Sensitivity of  $A_1$  species force constants<sup>a</sup> for ketene to the data sets used.

	Fit to $\Delta_J^\circ,$ $\Delta_{JK}^\circ, \delta_J^\circ, \delta_K^\circ$	Fit to $\Delta_{JK}^\circ,$ $\Delta_K^\circ$	Fit to $\Delta_J^\circ,$ $\Delta_{JK}^\circ$
$F_{11}$	6.11	5.86	5.89
$F_{12}$	0.93	0.46	0.15
$F_{13}$	[0.0]	[0.0]	[0.0]
$F_{14}$	0.17	-0.23	0.05
$F_{22}$	9.01	9.20	9.28
$F_{23}$	0.59	0.69	0.60
$F_{24}$	-0.27	-0.27	-0.29
$F_{33}$	15.3	15.4	15.3
$F_{34}$	[0.0]	[0.0]	[0.0]
$F_{44}$	0.614	0.622	0.608
	OBS	CALC	CALC
		$H_2CCO$	
$\Delta_J$	0.00339	0.00343	0.00336
$\Delta_{JK}$	0.476	0.486	0.480
$\Delta_K$	23.5	18.1	22.6
$\delta_J$	0.000145	0.000143	0.000137
$\delta_K$	0.329	0.284	0.273

Table 3.12 (continued)

	OBS	CALC	CALC	CALC
HDCCO				
$\Delta_J$	0.00316	0.00319	0.00312	0.00316
$\Delta_{JK}$	0.327	0.337	0.330	0.336
$\Delta_K$	(15.0)	13.6	15.7	14.4
$\delta_J$	0.000225	0.000221	0.000218	0.000209
$\delta_K$	0.239	0.235	0.227	0.225
$D_2CCO$				
$\Delta_J$	0.00272	0.00269	0.00263	0.00268
$\Delta_{JK}$	0.322	0.333	0.324	0.328
$\Delta_K$	5.39	4.33	4.76	5.46
$\delta_J$	0.000218	0.000213	0.000207	0.000202
$\delta_K$	0.213	0.198	0.192	0.189
Comments:	Very poor fit	Poor fit	Good overall	
	to $\omega_1, \omega_2$	to $\omega_2$ data.	fit to $\omega, \Delta\omega$	
	$\Delta\omega_1$ data.	Negative $F_{14}$	data.	
	$F_{12}$ unreason-	physically	Physically	
	ably large.	unreasonable.	acceptable	
			force constants.	

<sup>a</sup> For units, see footnote <sup>a</sup> of table 3.4.

<sup>b</sup> Distortion constants in kHz.

additional  $^{13}\text{C}$  frequency shift data.)

Alternatively, the experimentally determined  $\Delta_{\text{K}}^{\circ}$  values can be fitted in association with  $\Delta_{\text{J}}^{\circ}$  and  $\Delta_{\text{JK}}^{\circ}$ , with moderate fits ( $\sim 10\%$ ) to  $\delta_{\text{J}}^{\circ}$  and  $\delta_{\text{K}}^{\circ}$ . This is at the expense of a poor reproduction of  $\omega_2$  frequencies and a significant negative  $F_{14}$  interaction constant, which is sensitive to both  $\Delta_{\text{JK}}^{\circ}$  and  $\Delta_{\text{K}}^{\circ}$  (table 3.12 column 2).  $F_{14}$  is the  $\text{CH}_2$  str/ $\text{CH}_2$  def interaction constant and is both expected and determined to be small and positive in a large number of  $\text{CH}_2$  (and  $\text{CH}_3$ ) molecules for the corresponding coordinate definitions used. A significant negative value for  $F_{14}$  is considered to be quite unacceptable physically. It may be noticed in table 3.12 that the experimental  $\Delta_{\text{K}}^{\circ}$  value of  $\text{H}_2\text{CCO}$  is not achieved; this would require an even more negative  $F_{14}$  constant.

A good fit to  $\Delta_{\text{J}}^{\circ}$ ,  $\Delta_{\text{JK}}^{\circ}$ , with a moderate fit ( $\sim 10\%$ ) to  $\delta_{\text{J}}^{\circ}$  and  $\delta_{\text{K}}^{\circ}$  and a poor fit ( $\sim 15\%$ ) to  $\Delta_{\text{K}}^{\circ}$  is achieved by a set of more physically acceptable constants and a good overall frequency fit (table 3.12 column 3).

Although the last set of force constants appears to be the best estimate of their true values, in the analysis it became clear that further progress would be possible only with the assistance of the ab initio calculations (see section 3.3.4). The sign of the ab initio interaction constants were found to be in complete agreement with those of the previous experimentally determined force field of

Mallinson and Nemes (59). In addition, most were also found to be in quantitative agreement.

#### 3.4.5 JOINT EMPIRICAL AND AB INITIO CALCULATIONS

Comparison of  $A_1$  species force constant sets between tables 3.4 and 3.12 shows the greatest degree of correspondence between the ab initio constants and those of column 3 in table 3.12. The ab initio calculations are remarkably consistent in their predictions of  $F_{12}$  and  $F_{14}$ , the two most variable constants in the empirical estimates, and were found to be similar to the corresponding ethylene constants (see table 3.7). As discussed previously, the  $F_{23}$  is predicted to be too large by a factor of  $\sim 2$ .

Since reproduction of the  $\Delta_{JK}^{\circ}$  and  $\Delta_K^{\circ}$  distortion constants necessitates a negative  $F_{14}$  constant which is neither predicted nor acceptable on physical grounds, the ab initio value for this constant has been accepted. The two  $A_1$  constants  $F_{13}$  and  $F_{34}$  which were considered to be small, and were set to zero in the empirical calculations are predicted to be ca.  $-0.08 \text{mdynA}^{\circ-1}$  and  $0.00 \text{mdyn}$  respectively. The appreciable non-zero value of the  $F_{13}$  constant could perhaps result from the erroneously large ab initio  $F_{23}$  CC/CO constant. However, empirical predictions for the  $F_{23}$  constant are still large and infer strong coupling which must be associated between the CC and CO stretch modes in ketene. (A more realistic definition of coordinates might

be obtained using symmetric and antisymmetric CCO stretching combinations.) In the absence of experimental data sensitive to  $F_{13}$  and  $F_{34}$ , the ab initio predictions were accepted.

In the  $B_2$  species,  $F_{79}$  ( $\text{CH}_2$  asym str/in-plane CCO bend) is empirically undetermined and was constrained to zero. Here, the ab initio calculations are consistent in predicting an essentially zero value, and thus the constraint was maintained. Otherwise, the  $B_1$  and  $B_2$  species predictions are in line with the comparatively well defined empirical constants. The largest ab initio discrepancy with the Mallinson and Nemes empirical force field (59) for these species was found to lie in the  $F_{78}$  ( $\text{CH}_2$  asym str/rock) constant. However, introduction of  $^{13}\text{C}$  shifts to  $\nu_7$  and  $\nu_8$ , to which this constant is sensitive, has resulted in a substantially larger empirical estimate of  $F_{78}$ , and bringing it closer to the ab initio value.

Given in column 1 of table 3.13 is the GHFF for ketene in terms of the symmetry coordinates of table 3.1 determined from joint empirical/ab initio studies. The GHFF force constants are considered to be the most physically realistic set yet determined and are compared with other estimates made over the last 25 years, transformed to the present coordinate system where necessary. The reproduction of the 58 input data achieved from these force constants is given as the error vector,  $e = \text{observed} - \text{calculated}$ , in table 3.11.

Table 3.13. Combined empirical/ab initio GHFF<sup>a</sup> of ketene.

$F_{ij}$	GHFF	M&N(59)	F&T(60) <sup>f</sup>	M&P(52) <sup>f</sup>
$F_{11}$	5.880(55) <sup>b</sup>	6.080(105)	5.378(90)	5.345(26)
$F_{12}$	0.131(101)	1.590(296)	[0.00] <sup>d</sup>	[0.00] <sup>d</sup>
$F_{13}$	[-0.080] <sup>c</sup>	[0.000] <sup>d</sup>	[0.00] <sup>d</sup>	[0.00] <sup>d</sup>
$F_{14}$	[0.045] <sup>c</sup>	[0.176] <sup>e</sup>	[0.17] <sup>d</sup>	[0.00] <sup>d</sup>
$F_{22}$	9.244(113)	9.219(955)	8.926(900)	8.62(28)
$F_{23}$	0.551(72)	0.515(478)	0.602(600)	0.96(26)
$F_{24}$	-0.278(19)	-0.288(34)	-0.340(37)	-0.294(22)
$F_{33}$	15.440(124)	15.28(155)	15.38(152)	16.11(53)
$F_{34}$	[0.000] <sup>c</sup>	[0.000] <sup>d</sup>	[0.00] <sup>d</sup>	[0.00] <sup>d</sup>
$F_{44}$	0.6029(58)	0.613(13)	0.585(15)	0.585(9)
$F_{55}$	0.6685(32)	0.681(8)	0.582(10)	0.572(4)
$F_{56}$	0.0923(16)	0.101(4)	0.052(5)	0.053(1)
$F_{66}$	0.0879(6)	0.093(2)	0.083(5)	0.0861(6)
$F_{77}$	5.784(47)	5.754(25)	5.432(70)	5.266(21)
$F_{78}$	-0.227(65)	-0.098(262)	[-0.56] <sup>d</sup>	[0.00] <sup>d</sup>
$F_{79}$	[0.000] <sup>c</sup>	[0.000] <sup>d</sup>	[0.00] <sup>d</sup>	[0.00] <sup>d</sup>
$F_{88}$	0.7502(74)	0.708(24)	0.764(40)	0.707(42)
$F_{89}$	-0.1888(40)	-0.204(8)	-0.172(14)	-0.189(15)
$F_{99}$	0.6479(75)	0.696(24)	0.627(40)	0.652(46)

<sup>a</sup> For units see footnote <sup>a</sup> of table 3.4.

<sup>b</sup> Values in parenthesis are one standard deviation in units of the last figures.

<sup>c</sup> Constrained to ab initio predicted values.

See table 3.4

<sup>d</sup> Constrained to value quoted.

<sup>e</sup> Constrained to hybrid orbital model prediction -  $F_{14} = 0.029F_{11}$  (61).

<sup>f</sup> Fit to observed frequencies.

Force constant refinement calculations are performed around a chosen fixed molecular geometry, which ideally should be that of the equilibrium structure. In the absence of such a structure, the ground state structure is often used, as here. The calculation of the distortion constants depends upon the fourth power of the isotopic moments of inertia, so the values must be dependent to some extent on the molecular geometry chosen. Since one of the moments of inertia is very small and highly dependent on the configuration of the CH<sub>2</sub> group, it was considered that some of the distortion constant misfits (particularly to  $\Delta_K^{\circ}$ ) could perhaps arise from this source.

In an analogous fashion to that in the ab initio studies, calculations were repeated in terms of varying molecular structures including an approximate equilibrium structure estimate (94) of

$$\begin{aligned} r_e(\text{CH}) &= 1.073\text{\AA}^{\circ}, \\ r_e(\text{CC}) &= 1.316\text{\AA}^{\circ}, \\ r_e(\text{CO}) &= 1.161\text{\AA}^{\circ} \\ \text{and } \alpha_e(\text{HCH}) &= 122.0\text{\AA}^{\circ}. \end{aligned}$$

This structure yielded an increase in  $\Delta_K^{\circ}$  of  $\sim 4\%$  compared with the misfits of  $\sim 15\%$ . The fit of  $\Delta_J^{\circ}$ ,  $\Delta_{JK}^{\circ}$  and  $\delta_J^{\circ}$  was impaired somewhat, and that of  $\delta_K^{\circ}$  improved

marginally. All structure variations considered produced minimal changes in the refined constants, well within the standard deviations in table 3.13. The problem of fitting the ground state quartic distortion constants is thus not associated significantly with the choice of molecular geometry. Since Duncan et al. (92) found that the centrifugal distortion constants were apparently rather precisely determined by the ground state rotational data, then the large harmonic force field misfits associated with these could perhaps result from appreciable anharmonicity factors. For the phosphine molecule, equilibrium centrifugal distortion constants may be calculated from experimental data and appear to require anharmonicity corrections of the order of 10% (93). Similar corrections seem to be necessary here for ketene.

### 3.5 SCALED AB INITIO FORCE CONSTANTS

The absolute accuracy of ab initio force constants calculated at the SCF level is somewhat limited, but as indicated previously, the errors are largely systematic. In a recent ab initio force field review paper by Fogarasi and Pulay (12), the following conclusions were made. Firstly, the diagonal stretching constants are overestimated by  $\sim 10-15\%$ . Secondly, overestimation of the bending modes are usually higher, about 20-30%. Thirdly, for off-diagonals, the results are less systematic, but large values are obtained within a comparable accuracy of  $\sim 20\%$ , while smaller

values generally have absolute errors of within 0.05-0.10 in the units concerned.

For molecules where accurate vibrational frequencies have been measured, the ab initio force constants may be scaled down in terms of the Scaled Quantum Method (SQM) of Pulay et al. (67). In this method force constants  $F_{ii}$  and  $F_{jj}$  are scaled by  $C_i$  and  $C_j$ , and  $F_{ij}$  by  $(C_i C_j)^{1/2}$ , where  $C_i$  and  $C_j$  are scale factors. These are defined as

$$C_i = [\omega_i(\text{OBS})/\omega_i(\text{Ab initio})]^2$$

and

$$C_j = [\omega_j(\text{OBS})/\omega_j(\text{Ab initio})]^2$$

These are mutually averaged over several isotopic species. Note that harmonic frequencies are more commonly used.

In the present studies, only the 6-31G\*\*/6-31G\*\* and 6-31G\*\*/Expt force constants were scaled because it was considered that these represent the most accurate ab initio predictions. Scaling was effected in terms of empirical force field predicted frequencies instead of observed harmonic values since the latter are subject to appreciable vibrational resonances, particularly for  $\nu_3$  and  $\nu_4$ . The scale factors were averaged over the  $\text{H}_2\text{CCO}$ ,  $\text{HDCCO}$  and  $\text{D}_2\text{CCO}$  species.

Serious overestimate of the  $F_{66}$  wag force constant discussed previously, as well as the sensitivity of the  $B_1$

vibrations to the  $F_{56}$  (wag/CCO bend), resulted in considerable variation in the scale factors for the  $B_1$  force constants. Thus, for the  $S_5$  coordinate (out-of-plane CCO bend), adoption of the consistent scale factors for the  $S_9$  coordinate (in-plane CCO bend) was considered to be a reasonable compromise. However, the  $S_6$  coordinate ( $CH_2$  wag) had to be scaled uniquely by an averaged, but largely variant scale factor. A similar but less pronounced overestimation of the wag coordinate was found by Fogarasi and Pulay for ethylene and is reflected in their small wag scale factor (68).

Scale factors for all vibrations were grouped together as far as possible according to their numerical values rather than to their vibrational types. The reasons for this were twofold. Firstly, classification in terms of vibrational type for ketene leads to 7 groups and hence 7 scale factors. These are  $CH_2$  stretch,  $CH_2$  symmetric deformation, CC stretch, CO stretch, CCO bend,  $CH_2$  wag, and  $CH_2$  rock. This was considered to be too large a number of factors in proportion to the 19 force constants of ketene. Secondly, the main objective of scaling, in any case, is to reduce the magnitude of the diagonal force constants, whilst having a much smaller effect on off-diagonal constants, which are generally small anyway. Thus to preserve the theoretical information as far as possible, a minimum number of scale factors was and is desirable.

Three and five scale factors were found to be necessary

to scale down the 6-31G\*\*/6-31G\*\* and 6-31G\*\*/Expt force constants respectively according to the SQM method. These are given, together with their groupings in tables 3.14 and 3.15. As may be seen by comparing these tables, the numerical similarity of the  $S_2$ ,  $S_3$ ,  $S_4$ ,  $S_8$  and  $S_9$  scale factors is largely lost by adoption of the experimental  $r_0$  geometry as a reference. This necessitated the larger number of scale factors in table 3.15.

The ab initio SQM 6-31G\*\*/6-31G\*\* and 6-31G\*\*/Expt force constants are compared with the GHFF constants in table 3.16. As may be seen, the agreement is generally very good. The largest discrepancy in the  $A_1$  species, not unexpectedly, lies in the  $F_{23}$  constant. The reason for this has been discussed in section 3.3.4. The  $F_{12}$  SQM and GHFF estimates differ by  $\sim 12\%$ . Here, however, the empirical constant is barely determined and is the most variant. For the rest of the  $A_1$  constant, agreement to within 6% is achieved. For the  $B_1$  species, similar numerical accord is found, though the overestimation of  $F_{66}$  in relation to  $F_{56}$  is not fully removed by scaling. As discussed previously, the  $B_1$  vibrations are very sensitive to small changes in the three associated force constants, thus vibrational predictions are likely to be significantly in error. Closest numerical agreement ( $\ll 0.05$ ) is evident between the  $B_2$  SQM and GHFF estimates.

Table 3.14. Scale factors for the  
6-31G\*\*/6-31G\*\* force field.

Vibrational Mode	Coordinate	Scale Factor
CH <sub>2</sub> stretch	S <sub>1</sub> , S <sub>7</sub>	0.90355
CC stretch	S <sub>2</sub>	0.82494
CO stretch	S <sub>3</sub>	
CH <sub>2</sub> sym def	S <sub>4</sub>	
CCO bend	S <sub>5</sub> , S <sub>9</sub>	
CH <sub>2</sub> rock	S <sub>8</sub>	
CH <sub>2</sub> wag	S <sub>6</sub>	0.54070

Table 3.15. Scale factors for the  
6-31G\*\*/Expt force field.

Vibrational Mode	Coordinate	Scale Factor
CH <sub>2</sub> stretch	S <sub>1</sub> , S <sub>7</sub>	0.95020
CC stretch	S <sub>2</sub>	0.85794
CH <sub>2</sub> sym def	S <sub>4</sub>	
CO stretch	S <sub>3</sub>	0.92139
CCO bend	S <sub>5</sub> , S <sub>9</sub>	0.83231
CH <sub>2</sub> rock	S <sub>8</sub>	
CH <sub>2</sub> wag	S <sub>6</sub>	0.54391

Table 3.16. Comparison of the GHFF, SQM(1)  
(6-31G\*\*/6-31G\*\*) and SQM(2)  
(6-31G\*\*/Expt) force fields<sup>a</sup>.

$F_{ij}$	GHFF	SQM(1)	SQM(2)
$F_{11}$	5.880	5.845	5.858
$F_{12}$	0.131	0.115	0.129
$F_{13}$	$[-0.080]^b$	-0.074	-0.078
$F_{14}$	$[0.045]^b$	0.039	0.039
$F_{22}$	9.244	9.058	9.004
$F_{23}$	0.551	1.051	1.090
$F_{24}$	-0.278	-0.289	-0.300
$F_{33}$	15.440	16.328	16.158
$F_{34}$	$[0.000]^b$	-0.001	-0.002
$F_{44}$	0.6029	0.5850	0.6032
$F_{55}$	0.6685	0.6685	0.6483
$F_{56}$	0.0923	0.0655	0.0713
$F_{66}$	0.0879	0.0742	0.0872
$F_{77}$	5.784	5.790	5.801
$F_{78}$	-0.227	-0.245	-0.252
$F_{79}$	$[0.000]^b$	0.011	0.010
$F_{88}$	0.7502	0.7637	0.7716
$F_{89}$	-0.1888	-0.1860	-0.1855
$F_{99}$	0.6479	0.6408	0.6308

<sup>a</sup> For units, see footnote <sup>a</sup> to table 3.4

<sup>b</sup> Constrained to ab initio values.

### 3.6 SPECTROSCOPIC DATA FOR ISOTOPIC KETENES

Spectroscopic parameters for isotopic ketenes were obtained from both the GHFF and SQM constants and are discussed below. For the latter, only the 6-31G\*\*/6-31G\*\* constants were considered.

#### (a) Frequency data

For clarity of reference, the observed (harmonic), GHFF and SQM frequencies are listed at the top of table 3.17 where it may be seen that the GHFF frequencies agree rather well with those observed. Other than  $\nu_4$ , the unperturbed position of which is quite uncertain in all isotopic species, the main discrepancies involve the  $\nu_3$  and  $\nu_5$  fundamentals. The misfit in  $\nu_3$  (calculated too high in  $\text{H}_2\text{CCO}$ , too low in  $\text{D}_2\text{CCO}$ ) is almost certainly indicative of the effects of Fermi resonance complications. However, the perturbation analyses of  $\nu_3$  in both species were only approximate and possibly may not represent the full extent of perturbations, which decrease the apparent position of  $\nu_3$  in  $\text{H}_2\text{CCO}$  and increase it in  $\text{D}_2\text{CCO}$ . Larger corrections than those allowed would remove the apparent discrepancy in table 3.17.

The situation in the  $B_1$  species is different, and arises from the complexity of the analysis of the Coriolis interacting  $\nu_5, \nu_6, \nu_9$  system, such that the vibrational frequencies may be uncertain by  $1\text{-}2\text{cm}^{-1}$ . As indicated

Table 3.17. Comparison of the observed (harmonic) frequencies with those predicted by GHFF and SQM 6-31G\*\*/6-31G\*\*,  $\text{cm}^{-1}$ .

	$\text{H}_2\text{CCO}$			$\text{HDCCO}$			$\text{D}_2\text{CCO}$		
	OBS	GHFF	SQM	OBS	GHFF	SQM	OBS	GHFF	SQM
$\omega_1$	3215.0	3211.0	3202.0	2400.5	2401.4	2395.8	2345.2	2347.5	2337.5
$\omega_2$	2185.3	2181.2	2175.7	2174.9	2172.7	2169.2	2152.3	2159.5	2159.0
$\omega_3$	1415.8	1422.5	1406.0	1316.5	1319.7	1313.8	1247.0	1238.2	1246.1
$\omega_4$	1133.0	1132.7	1147.7	1101.0	1096.9	1105.3	936.4	921.0	915.8
$\omega_5$	593.2	591.8	569.1	560.6	561.5	568.8	546.1	554.2	568.7
$\omega_6$	539.2	535.9	530.8	506.3	504.0	473.8	442.0	440.3	408.6
$\omega_7$	3307.5	3306.5	3306.7	3261.8	3262.3	3258.5	2467.1	2467.3	2466.4
$\omega_8$	997.8	996.0	999.4	882.7	882.9	883.1	866.8	868.4	869.7
$\omega_9$	443.4	442.0	442.6	401.6	402.3	403.3	373.8	374.7	376.1

	$\text{H}_2\text{C}^{13}\text{CO}$			$\text{H}_2^{13}\text{CCO}$		
	OBS	GHFF	SQM	OBS	GHFF	SQM
$\Delta\omega_1$	0.1	0.05	0.04	6.1	5.65	5.65
$\Delta\omega_2$	58.3	59.26	58.46	5.52	5.54	4.13
$\Delta\omega_3$	-	0.05	0.00	12.9	13.43	15.20
$\Delta\omega_4$	[8.4]	0.86	1.26	[5.4]	16.37	15.75
$\Delta\omega_5$	5.51	5.45	15.87	0.38	0.41	2.38
$\Delta\omega_6$	10.09	10.13	0.03	5.79	5.99	4.09
$\Delta\omega_7$	0.0	0.00	0.00	14.82	14.14	14.02
$\Delta\omega_8$	10.97	11.02	10.83	8.14	8.03	8.08
$\Delta\omega_9$	-	7.55	7.66	-	0.05	0.06

previously, it is suspected that either of the frequencies of  $\nu_5$  or  $\nu_6$  in the  $\text{H}_2\text{CCO}$  are the most likely contenders, as the analysis here is in terms of medium resolution Q branch features, whereas those of  $\text{D}_2\text{CCO}$  are calculated in terms of a large number of rovibrational transitions in all three bands. The fact that  $\nu_5$  ( $\text{D}_2\text{CCO}$ ) is misfit is almost certainly spurious, and caused by the calculation attempting to fit also the associated interaction constants for  $\text{H}_2\text{CCO}$ .

The SQM frequency predictions of table 3.17, with the exception of the out-of-plane vibrations are generally very close to observed and GHFF predicted frequencies. The SQM  $\text{B}_2$  frequencies in particular are of comparable accuracy to those of the GHFF. The largest discrepancy lies in the  $\nu_4$  prediction for the  $\text{D}_2\text{CCO}$  species, where the SQM frequency is some  $20\text{cm}^{-1}$  lower than that observed. However, given that this vibration is subject to major Fermi resonance displacement, a misfit of this magnitude does not seem too unreasonable.

Collected in the lower half of table 3.17 are the observed, and calculated  $^{13}\text{C}$  frequency shifts. Not surprisingly, the SQM out-of-plane shifts are in very poor agreement with those observed and calculated from the GHFF. Apart from these, the  $\text{H}_2^{13}\text{CCO}$  shift to  $\nu_7$  represents the largest discrepancy between observed and calculated, with the GHFF and SQM predictions being considerably smaller. The observed shift was obtained from perturbation analysis, which made the assumption that  $\nu_7$  suffered perturbation by

only  $\nu_2 + \nu_8$  in both  $\text{H}_2\text{CCO}$  and  $\text{H}_2^{13}\text{CCO}$ . Given the large number of states possible around  $3100\text{cm}^{-1}$  owing to the lower lying  $\nu_5$ ,  $\nu_6$  and  $\nu_9$  vibrations, it is possible that other vibrational levels could significantly affect  $\nu_7$ . These could not be taken into account in the perturbation analysis and may thus cause the discrepancy.

(b) Quartic Distortion Constants.

Collected in table 3.18 are the observed ground state and calculated distortion constants. The misfits between the observed and GHFF predicted constants (also given as the error vector in table 3.11) is  $\sim 1\%$  in  $\Delta_J^0$ ,  $\sim 3\%$  in  $\Delta_{JK}^0$ , 12-15% in  $\Delta_K^0$ ,  $\sim 8\%$  in  $\delta_J^0$  and  $\sim 8\%$  in  $\delta_K^0$ . The SQM predictions are of comparable order of magnitude, but deviations from GHFF predictions and observed ground state constants are considerable.

(c) Coriolis Constants

The reproduction of the two largest Coriolis constants determined for  $\text{H}_2\text{CCO}$  is good, and it is believed that the two smaller ones are ill-determined. SQM values are not quoted on account of the small but significant differences between the SQM and well determined GHFF force constants, since this will lead to considerable errors in the Coriolis constants associated with the out-of-plane vibrations. Use of the GHFF calculated constants for  $\text{D}_2\text{CCO}$  of table 3.11 has been made in the recent high resolution analysis of the

Table 3.18. Comparison of the observed centrifugal distortion constants with those predicted by GHFF and SQM 6-31G\*\*/6-31G\*\*, kHz.

	H <sub>2</sub> CCO			HDCCO			D <sub>2</sub> CCO		
	OBS	GHFF	SQM	OBS	GHFF	SQM	OBS	GHFF	SQM
$\Delta_J$	3.39	3.40	3.27	3.16	3.17	3.06	2.71	2.70	2.61
$\Delta_{JK}$	476.0	486.1	477.3	327.0	332.5	325.5	321.4	325.2	318.1
$\Delta_K$	23535	19948	20482	15000	14542	14750	4800	4789	4928
$\delta_J$	0.145	0.134	0.129	0.225	0.211	0.205	0.220	0.204	0.200
$\delta_K$	329.6	270.9	311.5	239.2	224.0	181.6	203.0	189.0	206.5

region below  $1000\text{cm}^{-1}$  and they seem totally compatible with the extensive observations made and the large perturbations present. It is therefore felt that the predictive capacity of the GHFF of table 3.13 is high, and the calculated Coriolis interaction constants between fundamental vibrations for  $\text{H}_2\text{CCO}$ ,  $\text{HDCO}$  and  $\text{D}_2\text{CCO}$  are listed in table 3.19. These should be of considerable assistance to future studies of the vibration-rotation spectra of these species, which are required in order to give increased understanding of this fundamentally important molecule.

	$\nu_1$	$\nu_2$	$\nu_3$	$\nu_4$	$\nu_5$	$\nu_6$	$\nu_7$	$\nu_8$	$\nu_9$	$\nu_{10}$
$\nu_1$	2889	2115	1776	1324	979					
$\nu_2$		1424	1174	912	604					
$\nu_3$			1016	777	518					
$\nu_4$				670	430					
$\nu_5$					325					
$\nu_6$						287				
$\nu_7$							237			
$\nu_8$								192		
$\nu_9$									150	
$\nu_{10}$										110

Table 3.19. GHFF calculated Coriolis coupling constants  $\zeta_{ij}$  for  $H_2CCO$ ,  $D_2CCO$  and  $HDCCO$ .

	$\nu_1$	$\nu_2$	$\nu_3$	$\nu_4$	$\nu_5$	$\nu_6$	$\nu_7$	$\nu_8$	$\nu_9$
	3070	2153	1387	1116	587	528	3159	978	439
$\nu_5$	<sup>b</sup> 0.385 0.598 0.671 0.211								
$\nu_6$	0.346 0.788 0.509 0.013				H <sub>2</sub> CCO				
$\nu_7$	<sup>c</sup> 0.069 0.079 0.954 0.280				<sup>a</sup> 0.686 0.560				
$\nu_8$	0.774 0.581 0.031 0.249				0.116 0.715				
$\nu_9$	0.598 0.801 0.027 0.013				0.719 0.419				
	$\nu_1$	$\nu_2$	$\nu_3$	$\nu_4$	$\nu_5$	$\nu_6$	$\nu_7$	$\nu_8$	$\nu_9$
	2267	2120	1225	925	541	435	2383	852	371
$\nu_5$	<sup>b</sup> 0.308 0.939 0.031 0.151								
$\nu_6$	0.562 0.115 0.605 0.552				D <sub>2</sub> CCO				
$\nu_7$	<sup>c</sup> 0.194 0.067 0.647 0.734				<sup>a</sup> 0.030 0.899				
$\nu_8$	0.813 0.497 0.043 0.300				0.765 0.260				
$\nu_9$	0.495 0.864 0.035 0.083				0.719 0.419				
	$\nu_1$	$\nu_2$	$\nu_3$	$\nu_4$	$\nu_5$	$\nu_6$	$\nu_7$	$\nu_8$	$\nu_9$
	2319	2142	1292	1085	555	497	3117	867	398
$\nu_1$	<sup>c</sup> 0.089 0.416 0.076			<sup>a</sup> 0.094 0.478					
$\nu_2$	0.123 0.174			0.022 0.088		HDCCO			
$\nu_3$	0.026			0.019 0.098					
$\nu_4$	0.140 0.236			0.140 0.236					
$\nu_5$	<sup>b</sup> 0.070 0.936 0.225 0.207				0.100 0.121 0.014				
$\nu_6$	0.436 0.253 0.741 0.229				0.347 0.154 0.017				
$\nu_7$	<sup>c</sup> 0.124 0.038 0.751 0.522				<sup>a</sup> 0.228 0.713		<sup>c</sup> 0.130 0.339		
$\nu_8$	0.740 0.533 0.030 0.265				0.597 0.422		0.044		
$\nu_9$	0.466 0.809 0.012 0.077				0.750 0.108				

## CHAPTER 4

### EMPIRICAL AND AB INITIO STUDIES OF METHYLENE CHLORIDE

#### 4.1 INTRODUCTION

Several attempts have been made to derive a harmonic force field for methylene chloride (95-101). All have suffered from a lack of sufficient experimental observations, leading to indeterminacies, which have necessitated either the use of approximative methods of estimation (96), or the imposition of constraints of some kind (95,97-101). These have included applying the Urey-Bradley model to decrease the number of independent force constants (95,98), constraining force constants to be equal to each other in different dihalogeno methanes (97), and simply constraining undetermined force constants to be fixed at either non-zero (100) or zero (101) values. In some cases, the undetermined force constants have been quoted (95,99,100), usually with their associated much larger uncertainties.

In a recent extended spectroscopic study of the

methylene chloride molecule, Duncan et al. accumulated in excess of 55 vibrational data on the fundamental vibrations of 7 isotopic species of methylene chloride (102). To these may be added the observed fundamental vibration frequencies of  $\text{CHDCl}_2$  (100,103) and the centrifugal distortion constants of  $\text{CH}_2\text{Cl}_2$  and  $\text{CD}_2\text{Cl}_2$  determined by microwave spectroscopy (101). By use of the combination of 27 fundamental vibration frequencies, 37 heavy isotopic ( $^{37}\text{Cl}$  and  $^{13}\text{C}$ ) fundamental frequency shifts, and 10 quartic centrifugal distortion constants it was anticipated that an unconstrained harmonic force field for methylene chloride would be determined for the first time.

No ab initio force constant calculations for methylene chloride have previously been reported. Therefore, since it was anticipated that the experimental force field would be well defined, this offered a further opportunity to assess the reliability of the ab initio predictions.

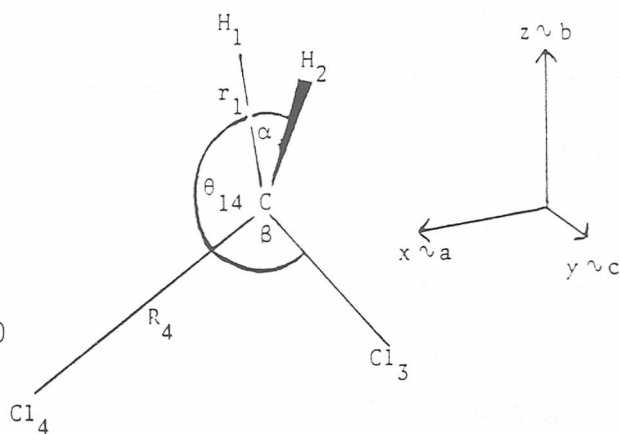
#### 4.2 SYMMETRY COORDINATES

The symmetry coordinates used by Davis et al. (101) are preferred in the present empirical and ab initio studies. These are listed in table 4.1 together with an averaged  $r_z$  geometry, determined by the above authors, which was adopted in the empirical studies. Ab initio calculations were performed around theoretical minima and will be discussed in section 4.4.2.

Table 4.1. Internal valence coordinates, symmetry coordinates, molecular geometry, and redundancy relations for methylene chloride.

Symmetry coordinates

$$\begin{aligned}
 S_1 &= (\delta r_1 + \delta r_2) / \sqrt{2} \\
 S_2 &= (\delta R_3 + \delta R_4) / \sqrt{2} \\
 A_1 \quad S_3 &= a\delta\alpha - b(\delta\theta_{13} + \delta\theta_{14} + \delta\theta_{23} + \delta\theta_{24}) \\
 S_4 &= c\delta\beta - d(\delta\theta_{13} + \delta\theta_{14} + \delta\theta_{23} + \delta\theta_{24}) \\
 S_R &= e\delta\alpha + f\delta\beta + g(\delta\theta_{13} + \delta\theta_{14} + \delta\theta_{23} + \delta\theta_{24}) \\
 A_2 \quad S_5 &= -(\delta\theta_{13} - \delta\theta_{14} - \delta\theta_{23} + \delta\theta_{24}) / 2 \\
 B_1 \quad S_6 &= (\delta r_1 - \delta r_2) / \sqrt{2} \\
 S_7 &= -(\delta\theta_{13} + \delta\theta_{14} - \delta\theta_{23} - \delta\theta_{24}) / 2 \\
 B_2 \quad S_8 &= (\delta R_3 - \delta R_4) / \sqrt{2} \\
 S_9 &= -(\delta\theta_{13} - \delta\theta_{14} + \delta\theta_{23} - \delta\theta_{24}) / 2
 \end{aligned}$$



Molecular geometry

$$\begin{aligned}
 r &= r(\text{CH}) = 1.0895\text{\AA}, & R &= r(\text{CCl}) = 1.7708\text{\AA}, \\
 \alpha &= \angle\text{HCH} = 111.60^\circ, & \beta &= \angle\text{ClCCl} = 112.03^\circ, \\
 \theta &= \angle\text{HCCl} = 108.31^\circ,
 \end{aligned}$$

$$e = 2 \sin(\alpha/2) \cos(\beta/2) / N = 0.40054$$

$$f = 2 \cos(\alpha/2) \sin(\beta/2) / N = 0.40379$$

$$g = \sin \theta / N = 0.41125$$

from which, through the condition of orthonormality,

$$a = 0.89906, \quad b = 0.21891,$$

$$c = 0.89766, \quad d = 0.22034.$$

[For the tetrahedral case,  $e = f = g = 1/\sqrt{6}$ ;  $a = c = 2/\sqrt{5}$ ;  $b = d = 1/2\sqrt{5}$ .]

### 4.3 EMPIRICAL FORCE FIELD STUDIES

#### 4.3.1 ASSIMILATED EXPERIMENTAL DATA

The data used have been obtained from infrared (102,103), Raman (100) and microwave (101) studies of isotopic methylene chlorides. In the most recent study (102), a large number of  $^{37}\text{Cl}$  isotopic vibrational shifts on fundamentals were observed in natural abundance. In addition, a complete set of  $^{13}\text{C}$  shifts were observed from a study of  $^{13}\text{CH}_2\text{Cl}_2$ , including some double  $^{13}\text{C}^{37}\text{Cl}$  isotopic shifts. Rather surprisingly, Duncan et al. (102) found no evidence whatsoever of Fermi resonance perturbations to the fundamentals of methylene chloride in any isotopic species, which is an unusual situation for a polyatomic molecule. Accordingly, this permitted the use of all the experimentally observed vibrational data in the evaluation of the vibrational potential function.

Centrifugal distortion constants of quality for  $\text{CH}_2^{35}\text{Cl}_2$  and  $\text{CD}_2^{35}\text{Cl}_2$  were available from the most recent microwave investigation (101). No Coriolis coupling constants had been determined experimentally for methylene chloride at the time of writing.

A large number of anharmonicity constants have been experimentally determined (102). However, their number is not sufficiently complete over different isotopic species to permit accurate vibrational anharmonicity correction through their use. Therefore, vibrational anharmonicity constants have been corrected approximately through application of Dennison's rule (equations 1.30 and 1.31) using the following anharmonicity factors,  $x$ , for  $\text{CH}_2\text{Cl}_2$ :

CH stretch	0.040
CH bend	0.020
CCl stretch	0.015
CCl bend	0.010

The observed, "harmonized" and calculated product rule ratios for  $\text{CH}_2^{35}\text{Cl}_2$ ,  $\text{CD}_2^{35}\text{Cl}_2$  and  $\text{CHD}^{35}\text{Cl}_2$  are given in table 4.2. In this table, it may be seen that the discrepancy between the observed and calculated ratios is removed satisfactorily, indicating the absence of significant vibrational resonances and the suitability of the chosen anharmonicity factors.

Uncertainties allowed in the data were 1% on fundamental vibrational frequencies, 2% on isotopic frequency shifts plus experimental error, and 3% on centrifugal distortion constants. The observed data, harmonized frequency data and

associated uncertainties are collected in table 4.3.

Table 4.2. Methylene chloride product rule ratios.

Species		OBS	HARM	THEORY
D <sub>2</sub> /H <sub>2</sub>	A <sub>1</sub>	0.519964	0.511289	0.506351
	A <sub>2</sub>	0.715525	0.711432	0.711181
	B <sub>1</sub>	0.598291	0.589746	0.589129
	B <sub>2</sub>	0.727938	0.723833	0.724229
HD/H <sub>2</sub>	A'	0.560691	0.551808	0.545184
	A''	0.725197	0.720996	0.717849

#### 4.3.3

#### FORCE CONSTANT CALCULATIONS

Refinement of the force constants, starting from the values quoted by Davis et al. (101) was straightforward. The vibrational data base forms a remarkably self-consistent set, with no single datum being markedly at variance, this deriving from the almost total lack of perturbation to any fundamental in the isotopic species concerned. The reproduction of the quartic distortion constants is also excellent, all constants being reproduced to better than 2%, with the exception of  $\Delta_K$  (CH<sub>2</sub>Cl<sub>2</sub>) which is reproduced to within 3%. This is in marked contrast to the situation in ketene, discussed in chapter 3. The error vector in the



final cycle of refinement is included in table 4.3. The largest frequency misfit is some  $6\text{cm}^{-1}$  in the antisymmetric  $\text{CD}_2$  stretch,  $\nu_6$  of  $\text{CD}_2\text{Cl}_2$ . The largest isotopic shift misfit is  $0.28\text{cm}^{-1}$  in the  $^{13}\text{C}$  shift of  $17.9\text{cm}^{-1}$  on the symmetric  $\text{CCl}_2$  stretch,  $\nu_3$ , of  $\text{CH}_2\text{Cl}_2$ . However, most frequencies are reproduced within  $2\text{cm}^{-1}$  and most shifts within  $0.1\text{cm}^{-1}$ .

The force constants with their least squares standard deviations are listed in table 4.4. All parameters are well defined with the sole exception of the  $F_{12}$   $\text{CH}_2$  str/ $\text{CCl}_2$  str for which the standard deviation is slightly larger than the constant determined. Comparison with methyl chloride predicts a value of between  $+0.1$  and  $+0.2\text{mdynA}^{\circ-1}$  for  $F_{12}$ , so it is felt that the refined value of  $+0.10\text{mdynA}^{\circ-1}$  is probably a realistic estimate for this interaction constant. Variation of  $F_{12}$  between values of  $0.0$  and  $+0.2\text{mdynA}^{\circ-1}$  results in only very small changes in the numerical values of all other force constants, typically  $\ll 0.04$ . Comparison of the force constants with the two most recent estimates of Escribano et al. (100) and Davis et al. (101) are also given in table 4.4, the former having been transformed to the present coordinate system in the  $A_1$  species. It will be seen that, in the absence of the isotopic frequency shift data, these both rather seriously under-estimate most of the determined  $A_1$  interaction force constants. Escribano et al. constrained the  $F_{67}$   $\text{CH}_2$  str/ $\text{CH}_2$  rock interaction constant to the value transferred from methyl chloride (100). This would appear to be a rather good transference, the

Table 4.4. The general harmonic force constants<sup>a</sup> for methylene chloride in terms of the symmetry coordinates of table 4.1, and comparison with the two most recent previous estimates.

$F_{ij}$	GHFF	EOMD(100) <sup>b</sup>	DRG(101) <sup>c</sup>
$F_{11}$	5.450(28) <sup>d</sup>	5.382(110)	5.088(54)
$F_{12}$	0.097(128)	[0.200] <sup>e</sup>	[0.00]
$F_{13}$	-0.125(60)	-0.244(120)	[0.00]
$F_{14}$	-0.152(66)	[0.022]	[0.00]
$F_{22}$	3.978(25)	3.832(150)	3.815(34)
$F_{23}$	-0.362(24)	-0.353(69)	-0.221(55)
$F_{24}$	0.323(16)	0.257(55)	0.246(13)
$F_{33}$	0.6623(85)	0.644(40)	0.583(11)
$F_{34}$	-0.326(18)	-0.246(45)	-0.229(28)
$F_{44}$	1.090(11)	1.095(49)	1.051(10)
$F_{55}$	0.6342(30)	0.627(10)	0.593(6)
$F_{66}$	5.428(26)	5.431(80)	5.039(53)
$F_{67}$	-0.127(16)	[-0.087]	[0.00]
$F_{77}$	0.8566(38)	0.835(11)	0.823(9)
$F_{88}$	3.036(10)	3.079(50)	2.930(34)
$F_{89}$	-0.5997(26)	-0.545(11)	-0.5553(35)
$F_{99}$	0.7113(33)	0.686(10)	0.660(11)

<sup>a</sup> For units see footnote <sup>a</sup> to table 3.4.

<sup>b</sup> Refined to harmonized frequency and Raman intensity data. The  $A_1$  species force constants have been transformed to the symmetry coordinates of table 4.1.

<sup>c</sup> Refined to observed frequency and centrifugal distortion data.

<sup>d</sup> Values in parenthesis are one standard deviation in units of the last significant figures.

<sup>e</sup> Values in square brackets were constrained in the fits shown.

constrained value of  $-0.087\text{mdyn}$  comparing with an empirical value of  $-0.127(16)\text{mdyn}$ . On the other hand, their  $F_{14}$   $\text{CH}_2$  str/ $\text{CCl}$  deformation interaction constant transferred from chloroform, is in poor agreement with the value required by the accumulated experimental data. One slightly unsatisfactory feature of this force field (and that of Escribano) is that the  $F_{13}$   $\text{CH}_2$  str/ $\text{CH}_2$  def assumes a negative value. As discussed with reference to ketene in chapter 3, a large number of  $\text{CH}_2$  and  $\text{CH}_3$  have been found to have a significant positive value for this constant. A negative value seems unacceptable on physical grounds and despite being well defined, GHFF  $F_{13}$  constant for methylene chloride seems to be in error. This could result from slightly incompatible data, possibly some of the distortion constants, or vibrational frequency shifts. Further discussions on the  $\text{CH}_2$  sym str interactions constants may be found in sections 4.4.3 and 4.6.

#### 4.4 AB INITIO STUDIES OF METHYLENE CHLORIDE

The ab initio studies of methylene chloride were carried out on the ab initio gradient program TEXAS (64). Evaluation of the SCF energies and gradients were more costly for methylene chloride than for ketene due to the larger number of electrons and also the inclusion of second row centres. Such centres are less well described than their first row analogues (104) and thus require larger numbers of basis functions to produce comparable accuracies.

From previous discussions (see section 3.3.2), split-valence basis sets were considered to be the best type of gaussian basis functions with which to carry out the present ab initio studies, since they represent a compromise between accuracy and economy.

From subsequent studies pertaining to ketene, such basis sets were found to give satisfactory descriptions of hydrogen and the first row elements carbon and oxygen. In the ab initio studies of methylene chloride the situation was altered somewhat due to the second row chlorine atoms. A number of split-valence basis sets have been developed for chlorine and other second row elements, namely, 3-21G, 4-31G, 6-21G and 6-31G. These second row split-valence basis sets differ from those of the first row by having alternative minimal type representation for the 2s and 2p shells. Second row split valence basis sets consist of single functions for each of the 1s, 2s and 2p (core) shells, in addition to inner and outer valence functions for the 3s and 3p shells and differ from each other only in the number of gaussian functions used to construct each orbital.

Three out of the four basis sets above, i.e. 3-21G, 4-31G and 6-21G were compared in a paper by Gordon et al. (39), where it was found that generally, all three gave molecular predictions of comparable accuracy. However, subsequent studies by Pietro et al. (104) tended to indicate

that molecular predictions for the second row by the 3-21G (and also presumably the 4-31G and 6-21G) were in poorer accord with experiment than those for the first row. This perhaps derives from the proportionally larger minimal type representation of second row basis sets.

Molecular predictions closer to the HF limit may be obtained by extending second row basis sets, in an identical fashion to those of the first row (see sections 1.3.3 and 3.3.2), to include d-orbital polarisation functions. From a number of small chlorine containing molecules, Francl et al. (40) determined an averaged value of 0.75 for chlorine polarisation exponent  $\alpha_d$  (of equation 3.1). Very recently, an identical value was advocated by Magusson and Schaefer (105).

Supplementing the second row 6-31G and 3-21G basis sets with polarisation functions was found to give molecular property predictions which were almost uniformly closer to experiment (104), though predictions of the former were slightly better. It is evident from the studies of Francl et al. (40) and Pietro et al. (104) that the largest basis sets produced the best results. Therefore, the 6-31G\*\*, which includes the largest split-valence basis set of the Pople group (35,40), was adopted in the present ab initio studies of methylene chloride. (In this case, the 6-31G\*\* basis set contains d-functions for both carbon and chlorine as well as p-functions for hydrogen.)

The ab initio equilibrium configurations for methylene chloride, determined from the selected basis sets were obtained in an identical way to those of ketene (see sections 1.3.5 and 3.3.3). In table 4.5 (below), the 6-31G and 6-31G\*\* geometries are compared with a recently determined experimental  $r_e$  structure of Duncan (106).

Table 4.5. Comparison of  $r_e$  structure with that predicted from 6-31G and 6-31G\*\*<sup>a</sup>.

	<u>r(CH)</u>	<u>r(CCl)</u>	<u><math>\alpha</math>(HCH)</u>	<u><math>\beta</math>(ClCCl)</u>	<u><math>\theta</math>(HCCl)</u>
6-31G	1.067	1.832	113.42	112.15	107.84
6-31G**	1.074	1.767	111.21	112.91	108.19
$r_e$	1.080	1.766	112.1	112.0	108.2

<sup>a</sup> For units see footnote to table 3.2.

Here, it may be seen that the 6-31G CCl bondlength is more than  $0.06\text{\AA}$  larger than both those of the 6-31G\*\* and the experimental  $r_e$  value, which perhaps reflects the importance of inclusion of polarisation functions in second row calculations. Apart from this discrepancy, agreement of the ab initio predictions with experiment is good, with bond angles deviating not more than  $1.3^\circ$  from those of the  $r_e$  structure. Notably, the inclusion of polarisation functions serves to bring the geometry predictions, on the whole,

closer to the experimental structure.

#### 4.4.3 AB INITIO FORCE FIELD STUDIES OF METHYLENE CHLORIDE

The ab initio force constants for methylene chloride were obtained by numerical followed by analytical differentiation of the total molecular energy in terms of a set of symmetry coordinates (see section 1.3.5). To facilitate direct comparison with those of the empirical studies of section 4.3, these were chosen to be the coordinates of table 4.1. As before, analytical differentiation was effected in terms of the two-sided distortion expression 1.43, with dominant cubic terms determined from expression 1.44. The magnitude of the distortions was chosen to be the same as those for ketene, i.e.  $\pm 0.05\text{A}^\circ$  for stretching coordinates and  $\pm 0.04\text{rad}$  for bending coordinates.

The 6-31G and 6-31G\*\* quadratic force constants are compared with those determined from empirical studies in table 4.6. The ab initio predictions may be seen to be fairly self-consistent, though 6-31G CCl stretching constants ( $F_{22}$  and  $F_{88}$ ) are considerably smaller. This is reflected to a lesser extent in the  $F_{44}$  CCl sym def. and also in the significantly smaller 6-31G  $F_{12}$  CH<sub>2</sub> str/CCl<sub>2</sub> str constant. These effects are almost certainly caused by the significant overestimation of the CCl bondlength by the unsupplemented 6-31G basis set (see section 4.4.2).

Table 4.6. Comparison of GHFF and ab initio force constants<sup>a</sup> for methylene chloride.

$F_{ij}$	GHFF	6-31G	6-31G**
$F_{11}$	5.450	6.483	6.235
$F_{12}$	0.097	0.045	0.154
$F_{13}$	-0.125	0.153	0.141
$F_{14}$	-0.152	-0.014	-0.013
$F_{22}$	3.978	3.646	4.484
$F_{23}$	-0.362	-0.397	-0.379
$F_{24}$	0.323	0.350	0.320
$F_{33}$	0.6623	0.714	0.731
$F_{34}$	-0.326	-0.263	-0.276
$F_{44}$	1.090	1.207	1.270
$F_{55}$	0.6342	0.735	0.764
$F_{66}$	5.428	6.476	6.175
$F_{67}$	-0.127	-0.035	-0.029
$F_{77}$	0.8566	0.937	1.029
$F_{88}$	3.036	2.929	3.556
$F_{89}$	-0.5997	-0.702	-0.662
$F_{99}$	0.7113	0.838	0.838

<sup>a</sup> For units see footnote <sup>a</sup> to table 3.4.

Despite the characteristic overestimation of SCF force constants, agreement between ab initio and empirical constants is fairly good, with general agreement in both sign and magnitude. Both sets of diagonal constants may be seen to be in semi-quantitative agreement. In addition, the ab initio symmetric/asymmetric stretch ratios,  $F_{11}/F_{66}$  and  $F_{22}/F_{88}$  for  $\text{CH}_2$  and  $\text{CCl}_2$  respectively qualitatively agree with empirical findings. Notably, however, agreement is less close than for ketene, perhaps indicating inferior description of second row elements by split-valence basis sets.

Of a number of discrepancies between the theoretical and experimental force fields, in table 4.6 it may be seen that the  $F_{13}$   $\text{CH}_2$  str/ $\text{CH}_2$  def predictions are in most marked disagreement. The ab initio value of 0.15mdyn, is in close accord with the corresponding coordinate in a large number of  $\text{CH}_2$  and  $\text{CH}_3$  molecules, but not with the well defined empirical value of -0.14mdyn. As indicated in the empirical studies of section 4.3, the latter constant may be driven to assume such a value by an erroneous shift or distortion constant. A similar situation was found for ketene, where the empirical  $\text{CH}_2$  str/ $\text{CH}_2$  def constant assumed a negative value for a better fit to the distortion constants, though it had a much larger associated uncertainty. The ab initio predictions for the same constant in ketene are consistently positive. It may also be seen from table 4.6, the empirical  $F_{14}$

$\text{CH}_2$  str/ $\text{CCl}_2$  def constant of methylene chloride is in marked disagreement with its ab initio counterpart, the former assuming a value some 10 times the latter.

A further small discrepancy may be found in the  $B_1$  species, where the ab initio  $F_{67}$   $\text{CH}_2$  asym str/rock is very much smaller than that obtained from empirical studies.

Dominant ab initio 6-31G\*\* cubic constants for methylene chloride are given in table 4.7. Here, it may be seen that the  $F_{111}$  and  $F_{666}$   $\text{CH}_2$  stretch diagonals are similar to that for other molecules, and are of comparable value to the corresponding ab initio constants of ethylene and ketene (quoted in section 3.3.4).

#### 4.4.4 SCALED AB INITIO FORCE FIELD

Only the 6-31G\*\* force constants were considered for scaling. It may be seen from table 4.6 that several of the 6-31G\*\* interaction constants are smaller than their empirical equivalents prior to scaling. Thus scaling by the SQM method would result in larger discrepancies between these GHFF and ab initio force constants. It has previously been suggested that scaling of ab initio force fields should not be extended to interaction constants (as indicated in reference 67). Certainly, in this instance, this would give somewhat closer force constant agreement. However, the reliability of the SQM method has been amply demonstrated by Pulay and co-workers and was thus maintained for the scaling

Table 4.7. Ab initio 6-31G\*\* diagonal and semi-diagonal cubic force constants<sup>a</sup> for methylene chloride.

F <sub>111</sub>	-24.9	F <sub>112</sub>	0.541	F <sub>113</sub>	-0.122	F <sub>114</sub>	-0.116
F <sub>221</sub>	-0.512	F <sub>222</sub>	-15.6	F <sub>223</sub>	0.441	F <sub>224</sub>	-1.04
F <sub>331</sub>	-0.305	F <sub>332</sub>	-0.326	F <sub>333</sub>	-0.429	F <sub>334</sub>	0.104
F <sub>441</sub>	-0.025	F <sub>442</sub>	-2.06	F <sub>443</sub>	0.729	F <sub>444</sub>	-2.38
F <sub>551</sub>	-0.037	F <sub>552</sub>	-0.531	F <sub>553</sub>	-0.015	F <sub>554</sub>	0.102
F <sub>661</sub>	-25.2	F <sub>662</sub>	0.642	F <sub>663</sub>	0.339	F <sub>664</sub>	-0.197
F <sub>771</sub>	0.016	F <sub>772</sub>	-0.833	F <sub>773</sub>	-0.318	F <sub>774</sub>	0.859
F <sub>881</sub>	-0.249	F <sub>882</sub>	-14.0	F <sub>883</sub>	0.095	F <sub>884</sub>	0.275
F <sub>991</sub>	0.059	F <sub>992</sub>	-0.866	F <sub>993</sub>	0.684	F <sub>994</sub>	-0.358

<sup>a</sup> For units see footnote <sup>a</sup> to table 3.4.

of the ab initio force constants for methylene chloride.

The 17 ab initio 6-31G\*\* force constants were scaled in terms of the GHFF H<sub>2</sub> HD and D<sub>2</sub> frequencies. As practised in chapter 3, scale factors with numerically similar values were grouped together and resulted in the four factors given in table 4.8 (below).

Table 4.8. Scale factors for the 6-31G\*\* force field.

Vibrational Mode	Coordinate	Scale Factor
CH <sub>2</sub> str	S <sub>1</sub> , S <sub>6</sub>	0.87988
CCl <sub>2</sub> str	S <sub>2</sub> , S <sub>8</sub>	0.85762
CH <sub>2</sub> def	S <sub>3</sub>	0.83567
CCl <sub>2</sub> def	S <sub>4</sub>	
torsion	S <sub>5</sub>	0.81359
rock	S <sub>7</sub>	
wag	S <sub>9</sub>	

In fact, the CH<sub>2</sub>/CCl<sub>2</sub> def and the torsion/wag/rock scale factors are still similar and may be further averaged and result in a less close frequency (but comparable frequency shift) reproduction. The same may also be done for the

stretching modes scale factors, leading to two scale factors and resulting in moderately good frequency predictions.

The SQM and GHFF force constants are given in table 4.9. As may be seen, reproduction of the diagonal constants is fairly good, though some off-diagonal constants, as anticipated, are significantly underestimated. The quality of the SQM force constants will be assessed in terms of prediction of spectroscopic constants in the following section.

#### 4.5 CALCULATED SPECTROSCOPIC PARAMETERS

The observed (harmonic) and GHFF frequencies and shifts of table 4.3 are reproduced in table 4.10 for ease of comparison with SQM predictions. As may be seen, in this table, the agreement is very impressive, with all SQM frequencies agreeing to within ca.  $10\text{cm}^{-1}$  of the observed and GHFF calculated values, whilst most shifts agree to better than  $0.3\text{cm}^{-1}$ . The major exceptions to the latter are the  $^{13}\text{C}$   $\nu_1$  and  $\nu_8$  shifts, which are under- and overestimated by  $0.9\text{cm}^{-1}$  and  $0.7\text{cm}^{-1}$  respectively by the SQM force field. The discrepancy in the  $\nu_1$  shifts almost certainly reflects the largely differing  $\text{CH}_2$  sym str interaction constants, particularly  $F_{13}$ , discussed in section 4.4.3. Differences in the  $^{13}\text{C}$   $\nu_8$  shifts probably result from the small difference between the SQM and GHFF  $F_{89}$   $\text{CCl}_2$  asym str/wag constant to which these shifts are sensitive.

Table 4.9. Comparison of GHFF and SQM force constants<sup>a</sup> for methylene chloride.

$F_{ij}$	GHFF	SQM
$F_{11}$	5.450	5.486
$F_{12}$	0.097	0.134
$F_{13}$	-0.125	0.121
$F_{14}$	-0.152	-0.011
$F_{22}$	3.978	3.845
$F_{23}$	-0.362	-0.321
$F_{24}$	0.323	0.271
$F_{33}$	0.6623	0.611
$F_{34}$	-0.326	-0.230
$F_{44}$	1.090	1.061
$F_{55}$	0.6342	0.621
$F_{66}$	5.428	5.433
$F_{67}$	-0.127	-0.025
$F_{77}$	0.8566	0.837
$F_{88}$	3.036	3.050
$F_{89}$	-0.5997	-0.553
$F_{99}$	0.7113	0.682

<sup>a</sup> For units see footnote <sup>a</sup> to table 3.4.

Table 4.10. Comparison of the observed (harmonic) frequencies and shifts for methylene chloride with those predicted by GHFF and SQM 6-31G\*\*/6-31G\*\*,  $\text{cm}^{-1}$ .

	$^{12}\text{CH}_2\ ^{35}\text{Cl}_2$			$^{12}\text{CHD}\ ^{35}\text{Cl}_2$			$^{12}\text{CD}_2\ ^{35}\text{Cl}_2$		
	OBS	GHFF	SQM	OBS	GHFF	SQM	OBS	GHFF	SQM
$\omega_1$	3122.6	3119.4	3116.4	2321.2	2321.7	2317.3	2272.5	2272.9	2317.3
$\omega_2$	1464.3	1466.0	1462.3	1309.5	1306.3	1306.1	1076.7	1078.0	1073.5
$\omega_3$	723.8	726.8	720.9	702.7	700.3	696.5	697.7	694.7	691.2
$\omega_4$	284.3	283.8	284.6	282.8	282.3	283.3	281.8	280.6	282.0
$\omega_5$	1176.5	1177.9	1184.0	904.4	902.2	909.9	837.0	837.7	841.8
$\omega_6$	3182.3	3187.2	3193.7	3149.5	3154.4	3157.5	2375.4	2369.3	2377.4
$\omega_7$	917.0	914.7	909.3	796.4	799.2	790.9	724.5	724.9	719.2
$\omega_8$	1294.8	1295.0	1293.2	1247.9	1246.7	1248.1	975.8	976.4	983.9
$\omega_9$	771.4	770.5	778.0	750.7	750.1	752.9	740.9	740.1	740.8

	$^{12}\text{CH}_2\ ^{35}\text{Cl}\ ^{37}\text{Cl}$			$^{13}\text{CH}_2\ ^{35}\text{Cl}_2$			$^{13}\text{CH}_2\ ^{35}\text{Cl}\ ^{37}\text{Cl}$			$^{12}\text{CD}_2\ ^{35}\text{Cl}\ ^{37}\text{Cl}$		
	OBS	GHFF	SQM	OBS	GHFF	SQM	OBS	GHFF	SQM	OBS	GHFF	SQM
$\Delta\omega_1$	0.00	0.00	0.00	6.94	6.94	6.00	6.94	6.94	6.00	0.00	0.00	0.00
$\Delta\omega_2$	0.0	0.02	0.02	4.06	4.02	3.79	4.06	4.05	3.81	0.00	0.01	0.00
$\Delta\omega_3$	2.95	3.12	2.98	17.93	17.65	17.90	20.71	20.88	20.99	3.17	3.37	3.22
$\Delta\omega_4$	3.43	3.36	3.40	1.33	1.32	1.29	4.69	4.63	4.65	3.14	3.25	3.30
$\Delta\omega_5$	0.20	0.17	0.16	0.00	0.00	0.00	0.17	0.17	0.16	-	0.24	0.23
$\Delta\omega_6$	0.00	0.00	0.00	12.69	12.59	13.00	12.69	12.59	13.00	0.00	0.00	0.00
$\Delta\omega_7$	0.30	0.30	0.29	9.27	9.23	9.02	9.56	9.53	9.31	0.40	0.38	0.36
$\Delta\omega_8$	0.16	0.17	0.14	4.37	4.38	5.07	4.53	4.57	5.22	-	0.06	0.07
$\Delta\omega_9$	2.24	2.24	2.32	21.80	21.91	21.72	24.11	24.17	24.07	2.49	2.53	2.54

Centrifugal distortion constants for  $\text{CH}_2^{35}\text{Cl}_2$  and  $\text{CD}_2^{35}\text{Cl}_2$  are similarly compared in table 4.11, where it may be seen that agreement between the ground state and GHFF and SQM predictions is very good. In addition to these, table 4.11 includes GHFF predictions for some  $^{13}\text{C}$  and  $^{37}\text{Cl}$  methylene chlorides. These were estimated in terms of the calculated isotopic change in each constant subtracted from the observed values for  $\text{CH}_2^{35}\text{Cl}_2$  and  $\text{CD}_2^{35}\text{Cl}_2$ . It is considered that this will give much more reliable and accurate estimates than do absolute values, since the anharmonicity effects on the isotopic differences will be extremely small. The values quoted for  $\text{CHDCl}_2$  in table 4.11 are all calculated ones, since no experimental results have been reported.

No Coriolis coupling constants have yet been determined experimentally for any isotope of methylene chloride. The effects of such an interaction may be visually observed, for example, in the changing subband Q branch degradation in the very intense  $\nu_9$   $\text{CCl}_2$  stretching fundamental of  $\text{CH}_2\text{Cl}_2$ , due to Coriolis interaction with the adjacent very weak  $\nu_3$   $\text{CCl}_2$  stretching fundamental (102). It is considered that the quality of the GHFF for methylene chloride is such that calculated Coriolis coupling constants should be reliable, and therefore of assistance towards the analyses of such interacting band systems. Collected in table 4.12 are the GHFF predicted  $\zeta_{ij}$  constants for  $\text{CH}_2^{35}\text{Cl}_2$ ,  $\text{CD}_2^{35}\text{Cl}_2$  and  $\text{CHD}^{35}\text{Cl}_2$ , together with those predicted from the SQM force field, in brackets. Here, it may be seen that the agreement

Table 4.11. Ground state, GHFF and SQM centrifugal distortion constants for a number of isotopic species of methylene chloride, kHz.

Species		$\Delta_J$	$\Delta_{JK}$	$\Delta_K$	$\delta_J$	$\delta_K$
$^{12}\text{CH}_2^{35}\text{Cl}_2$	OBS	1.392	-26.18	473.2	0.1770	5.36
	GHFF	1.371	-26.19	467.2	0.1774	5.23
	SQM	1.385	-25.92	465.7	0.1752	5.05
$^{12}\text{CD}_2^{35}\text{Cl}_2$	OBS	1.298	-15.88	204.0	0.1901	4.08
	GHFF	1.275	-15.76	201.8	0.1929	4.05
	SQM	1.287	-15.77	201.2	0.1884	3.81
$^{12}\text{CHD}^{35}\text{Cl}_2$	GHFF	1.3224	-19.987	297.25	0.1871	4.636
	SQM	1.3358	-19.743	296.26	0.1839	4.439
$^{12}\text{CH}_2^{35}\text{Cl}^{37}\text{Cl}^a$	GHFF	1.3255	-25.547	469.75	0.16493	5.137
$^{12}\text{CH}_2^{37}\text{Cl}_2^a$	GHFF	1.2610	-24.923	466.35	0.15348	4.913
$^{13}\text{CH}_2^{35}\text{Cl}_2^a$	GHFF	1.3792	-25.034	447.26	0.18345	5.337
$^{12}\text{CD}_2^{35}\text{Cl}^{37}\text{Cl}^a$	GHFF	1.2373	-15.526	202.66	0.17752	3.913

<sup>a</sup> Calculated values in terms of isotopic differences relative to experimental values.

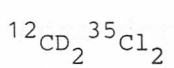
Table 4.12.

Coriolis interaction constants for methylene chloride  
and its deuterated isotopomers (SQM values in brackets).

	$\nu_1$	$\nu_2$	$\nu_3$	$\nu_4$	$\nu_5$	$\nu_6$	$\nu_7$	$\nu_8$	$\nu_9$
	2998	1435	713	281	1153	3055	899	1269	760
$\nu_1$					b 0.756 (0.818)	a 0.144 (0.055)	0.913 (0.925)	c 0.645 (0.565)	0.066 (0.054)
$\nu_2$					0.649 (0.567)	0.989 (0.997)	0.141 (0.073)	0.753 (0.818)	0.072 (0.024)
$\nu_3$					0.023 (0.004)	0.034 (0.063)	0.348 (0.342)	0.016 (0.019)	0.764 (0.772)
$\nu_4$					0.079 (0.099)	0.019 (0.005)	0.160 (0.147)	0.132 (0.102)	0.637 (0.634)
$\nu_5$		$^{12}\text{CH}_2\text{ }^{35}\text{Cl}_2$				c 0.531 (0.520)	0.778 (0.785)	a 0.010 (0.009)	0.029 (0.029)
$\nu_6$								b 0.839 (0.847)	0.094 (0.078)
$\nu_7$								0.456 (0.455)	0.417 (0.405)
	$\nu_1$	$\nu_2$	$\nu_3$	$\nu_4$	$\nu_5$	$\nu_6$	$\nu_7$	$\nu_8$	$\nu_9$
	2206	1061	688	279	825	2304	713	961	730
$\nu_1$					b 0.719 (0.784)	a 0.237 (0.149)	0.867 (0.888)	c 0.685 (0.606)	0.043 (0.066)
$\nu_2$					0.681 (0.603)	0.970 (0.989)	0.188 (0.131)	0.725 (0.785)	0.009 (0.091)
$\nu_3$					0.090 (0.059)	0.041 (0.010)	0.412 (0.399)	0.065 (0.128)	0.712 (0.717)
$\nu_4$					0.106 (0.135)	0.028 (0.004)	0.207 (0.186)	0.033 (0.029)	0.700 (0.688)
$\nu_5$		$^{12}\text{CD}_2\text{ }^{35}\text{Cl}_2$				c 0.491 (0.481)	0.767 (0.774)	a 0.008 (0.005)	0.047 (0.048)
$\nu_6$								b 0.863 (0.865)	0.050 (0.105)
$\nu_7$								0.478 (0.492)	0.399 (0.367)

Table 4.12. (continued)

	$\nu_1$	$\nu_2$	$\nu_3$	$\nu_4$	$\nu_5$	$\nu_6$	$\nu_7$	$\nu_8$	$\nu_9$
	2251	1286	692	280	890	3025	782	1224	740
$\nu_1$		<sup>a</sup> 0.431 (0.416)	0.233 (0.232)	0.012 (0.006)	<sup>b</sup> 0.707 (0.749)	<sup>a</sup> 0.202 (0.101)	0.777 (0.804)	<sup>b</sup> 0.147 (0.101)	0.098 (0.166)
$\nu_2$			0.113 (0.094)	0.028 (0.026)	0.459 (0.368)	0.877 (0.900)	0.160 (0.086)	0.396 (0.362)	0.169 (0.177)
$\nu_3$				0.055 (0.053)	0.186 (0.174)	0.125 (0.147)	0.373 (0.365)	0.047 (0.059)	0.070 (0.062)
$\nu_4$					0.081 (0.103)	0.018 (0.001)	0.174 (0.157)	0.048 (0.059)	0.007 (0.002)
$\nu_5$	<sup>c</sup> 0.624 (0.585)	0.165 (0.207)	0.050 (0.001)	0.057 (0.110)		<sup>b</sup> 0.045 (0.053)	0.495 (0.509)	<sup>a</sup> 0.008 (0.006)	0.020 (0.032)
$\nu_6$					<sup>c</sup> 0.057 (0.071)	<sup>a</sup>	0.346 (0.327)	<sup>b</sup> 0.852 (0.878)	0.080 (0.073)
$\nu_7$					0.688 (0.706)			0.214 (0.211)	0.329 (0.287)
$\nu_8$	<sup>c</sup> 0.247 (0.182)	0.752 (0.806)	0.066 (0.096)	0.105 (0.077)		<sup>c</sup> 0.503 (0.454)	0.262 (0.244)	<sup>a</sup>	0.020 (0.020)
$\nu_9$	0.081 (0.118)	0.042 (0.029)	0.733 (0.744)	0.667 (0.653)		0.048 (0.048)	0.082 (0.034)		



between the two is very good, and is a further indication of the quality of ab initio predictions.

#### 4.6 JOINT EMPIRICAL/AB INITIO GHFF FOR METHYLENE CHLORIDE

Three force constants in the GHFF are rather poorly defined,  $F_{12}$ ,  $F_{13}$  and  $F_{14}$  and the latter two are at variance to the ab initio predictions. Here, the predictions seem more reasonable. A positive value for a  $\text{CH}_2$  str/ $\text{CH}_2$  def interaction would be anticipated, for the definition of coordinates used. Also, a small interaction would be anticipated between  $\text{CH}_2$  and  $\text{CCl}_2$  def coordinates. All other empirically determined force constants appear to be well defined by a number of independently measured data, and are therefore considered to be reliable.

Accordingly, force constant calculations were repeated, in a similar fashion to those for ketene, in which the  $F_{12}$ ,  $F_{13}$  and  $F_{14}$  were constrained to their SQM predicted values. The effect of these constraints on other force constants is fairly small, causing small numerical adjustments most notably in  $F_{11}$ ,  $F_{23}$  and  $F_{33}$  (of +0.12, -0.05, and -0.006 respectively). Comparable data reproduction to that in table 4.3 was obtained for most species. Significantly, however, reproduction of the observed  $\nu_1$  frequency shifts is poor ( $e = 1.1\text{cm}^{-1}$ ) and reflects the large difference between the GHFF and SQM values for  $F_{13}$ . As indicated previously,

the most recent IR study of methylene chloride (102) found no evidence of appreciable resonance displacements to  $\nu_1$  (or any other vibration) in any of the large number of isotopic species examined. This perhaps indicates that the GHFF  $F_{12}$ ,  $F_{13}$  and  $F_{14}$  constants are closer to their true values than the corresponding SQM predictions, despite the fact that the latter, especially  $F_{13}$ , would appear to be more acceptable, physically. Finally, it is interesting to note that a similar ab initio/experimental sign ambiguity to that for  $F_{13}$ , was found in the analogous  $\text{CH}_3$  sym str/ $\text{CH}_3$  umbrella constant of methyl fluoride (107). For methyl fluoride, as was found here for methylene chloride, the sign ambiguity remains largely unresolved.

## REFERENCES

- (1) E. B. Wilson, J. C. Decius and P.C. Cross, Molecular Vibrations, McGraw-Hill, New York (1955).
- (2) H. C. Allen and P.C. Cross, Molecular Vib-Rotors, Wiley, N. Y. (1963).
- (3) G. Herzberg, Molecular Spectra and Molecular Structure, Vol. 2 : Infrared and Raman Spectra of Polyatomic Molecules, Van Nostrand (1945).
- (4) H. W. Kroto, Molecular Rotation Spectra, Wiley (1975).
- (5) L. A. Woodward, Theory of Molecular Vibrations and Vibrational Spectroscopy, Clarendon Press, Oxford (1972).
- (6) P. Gans, Vibrating Molecules: An Introduction to the Interpretation of Infrared and Raman Spectra, Chapman and Hall, London (1971).
- (7) J. L. Duncan, Molecular Spectroscopy, 3, 104 (1975).
- (8) H. F. Schaefer III, ed, Methods of Electronic Structure Theory, Plenum (1977).
- (9) H. F. Schaefer III, ed, Applications of Electronic Structure Theory, Plenum (1977).
- (10) J. A. Pople, Ber. Bunsenges. Phys. Chem., 86, 109 (1982).
- (11) P. Pulay, Molec. Phys., 17, 197 (1969).
- (12) G. Fogarasi and P. Pulay, Ann. Rev. Phys. Chem., 35, 191 (1984).

- (13) E. B. Wilson and J. B. Howard, *J. Chem. Phys.*, 4, 260 (1936).
- (14) B. T. Darling and D. M. Dennison, *Phys. Rev.*, 57, 128 (1940).
- (15) J. K. G. Watson, *Mol. Phys.*, 15, 479 (1968).
- (16) H. Eyring, J. Walter and G. F. Kamball, *Quantum Chemistry*, Wiley (1958).
- (17) L. D. Landau and E. M. Lifshitz, *Quantum Mechanics*, Pergamon (1956).
- (18) I. M. Mills, in *Molecular Spectroscopy - Modern Research*, Vol. 1, Chap. 3, edited by K. N. Rao and C. W. Mathews, Academic Press (1972).
- (19) G. W. King, R. M. Hainer and P. C. Cross, *J. Chem. Phys.*, 11, 27 (1943).
- (20) S. C. Wang, *Phys. Rev.*, 34, 243 (1929).
- (21) D. Kivelson and E. B. Wilson, *J. Chem. Phys.*, 20, 1575 (1952).
- (22) J. K. G. Watson, *J. Chem. Phys.*, 45, 1360 (1966).
- (23) J. K. G. Watson, *J. Chem. Phys.*, 48, 181 (1968).
- (24) H. A. Jahn, *Phys. Rev.*, 56, 680 (1939).
- (25) Ch. Lambeau, A. Fayt, J. L. Duncan and T. Nakagawa, *J. Mol. Spectrosc.*, 51, 524 (1974).
- (26) C. Eckart, *Phys. Rev.*, 47, 552 (1935).
- (27) A. A. Chalmers and D.C. McKean, *Spectrochim. Acta*, 22, 251 (1966).
- (28) D. C. McKean and J. L. Duncan, *Spectrochim. Acta*, 27A, 1879 (1971).
- (29) M. Born and R. Oppenheimer, *Ann. Physik.*, 84, 457 (1927).

- (30) C. C. J. Roothaan, *Rev. Mod. Phys.*, 22, 571 (1959).
- (31) J. C. Slater, *Phys. Rev.* 36, 79 (1930).
- (32) S. F. Boys, *Proc. Roy. Soc. (London)*, A200, 542 (1950).
- (33) W. J. Hehre, R. F. Stewart and J. A. Pople, *J. Chem. Phys.*, 51, 2657 (1969).
- (34) R. Ditchfield, W. J. Hehre and J. A. Pople, *J. Chem. Phys.*, 54, 724 (1971).
- (35) W. J. Hehre, R. Ditchfield and J. A. Pople, *J. Chem. Phys.*, 56, 2257 (1972).
- (36) P. Pulay, G. Fogarasi, F. Pang and J. E. Boggs, *J. Am. Chem. Soc.*, 101, 2550 (1979).
- (37) J. S. Binkley, J. A. Pople and W. J. Hehre, *J. Am. Chem. Soc.*, 102, 939 (1980).
- (38) W. J. Hehre and W. A. Lathan, *J. Chem. Phys.*, 56, 5255 (1972).
- (39) M. S. Gordon, J. S. Binkley, J. A. Pople, W. J. Pietro and W. J. Hehre, *J. Am. Chem. Soc.*, 104, 2797 (1982).
- (40) M. M. Francl, W. J. Pietro, W. J. Hehre, J. S. Binkley, M. S. Garden, D. J. DeFrees and J. A. Pople, *J. Chem. Phys.*, 77, 3654 (1982).
- (41) P. C. Hariharan and J. A. Pople, *Theoret. Chim. Acta*, 28, 213 (1973).
- (42) P. C. Hariharan and J. A. Pople, *Molec. Phys.*, 27, 209 (1974).
- (43) P. Pulay, chapter 4 of reference (9).

- (44) D. M. Bishop and M. Randic, *J. Chem Phys.*, 44, 2480 (1966).
- (45) P. Pulay, *Molec. Phys.*, 17, 197 (1969).
- (46) C. E. Blom, P. J. Slingerland and C. Altona, *Molec. Phys.*, 31, 1359 (1976).
- (47) H. Gershinowitz and E. B. Wilson, *J. Chem Phys.*, 5, 500 (1937).
- (48) B. Bak and F. A. Andersen, *J. Chem. Phys.*, 22, 1050 (1954).
- (49) W. A. Arendale and W. H. Fletcher, *J. Chem Phys.*, 24, 581 (1956).
- (50) W. A. Arendale and W. H. Fletcher, *J. Chem Phys.*, 26, 793 (1957).
- (51) P. E. Butler, D. R. Eaton and H. W. Thompson, *Spectrochim. Acta*, 13, 223 (1958)
- (52) C. B. Moore and G. C. Pimentel, *J. Chem Phys.*, 38, 2816 (1963).
- (53) A. P. Cox and A. S. Esbit, *J. Chem Phys.*, 38, 1636 (1963).
- (54) L. Nemes, *J. Mol. Spectrosc.*, 72, 102 (1978).
- (55) J. W. C. Johns, J. M. R. Stone and G. Winnewisser, *J. Mol. Spectrosc.*, 42, 523 (1972).
- (56) F. Winther, F. Hegelund and L. Nemes, *J. Mol. Spectrosc.*, 117, 388 (1986).
- (57) S. R. Polo, *Canad. J. Phys.*, 35, 880 (1957).
- (58) W. L. Lafferty, A. G. Maki and T. D. Coyle, *J. Mol. Spectrosc.*, 59, 470 (1976).
- (59) P. D. Mallinson and L. Nemes, *J. Mol. Spectrosc.*, 59, 470 (1976).

- (60) W. H. Fletcher and W. T. Thompson, *J. Mol. Spectrosc.*, 25, 240 (1968).
- (61) I. M. Mills, *Spectrochim. Acta*, 19, 1585 (1963).
- (62) C. Pouchan, A. Dargelos and M. Chaillet, *Spectrochim. Acta*, 33A, 253 (1977).
- (63) J. T. Gleghorn and F. W. McConkey, *J. Mol. Struct.*, 29, 133 (1975).
- (64) P. Pulay, *Theor. Chim. Acta*, 50, 299 (1979).
- (65) MINIT routine, devised by J. S. Crighton and S. Bell, Dundee University (1983).
- (66) H. B. Schlegel, S. Wolfe and F. Bernardi, *J. Chem Phys.*, 63, 3622 (1975).
- (67) P. Pulay, G. Fogarasi, G. Pongor, J. E. Boggs and A. Vargha, *J. Am Chem. Soc.*, 105, 7037 (1983).
- (68) G. Fogarasi and P. Pulay, *Acta Chim. Acad. Sci. Hung.*, 108, 55 (1981).
- (69) J. L. Duncan and E. Hamilton, *J. Mol. Struct*, 76, 65 (1981).
- (70) I. G. Csizmadia, M Harrison, J. W. Moskowitz and B. T. Sutcliffe, *Theor. Chim. Acta*, 6, 191 (1966).
- (71) B. Roos and P. Siegbahn, *Theor. Chim. Acta*, 17, 209 (1970).
- (72) T. H. Dunning, Jr and P. J. Hay, in reference 8.
- (73) S. Bell, *J. Chem Phys.*, 68, 3014 (1978).
- (74) C. W. Bock, P. George, G. J. Mains and M. Trachtman, *J. Mol. Struct*, 49, 215 (1978).
- (75) L. Schaefer, *J. Mol. Struct.*, 100, 51 (1983).
- (76) C. E. Dykstra and H. F. Schaefer III, *J. Am Chem. Soc.*, 98, 2689 (1976).

- (77) C. E. Dykstra, *J. Chem Phys.*, 68, 4244, (1978).
- (78) C. E. Blom and C. Altona, *Mol. Phys.*, 31, 1377 (1976).
- (79) C. E. Blom, L. P. Otto and C. Altona, *Mol. Phys.*, 32, 1137 (1976).
- (80) C. E. Blom and C. Altona, *Mol. Phys.*, 33, 875 (1977).
- (81) C. E. Blom and C. Altona, *Mol. Phys.*, 34, 177 (1977).
- (82) C. E. Blom, C Altona and A. Oskam, *Mol. Phys.*, 34, 557 (1976).
- (83) C. E. Blom and A. Muller, *J. Mol. Spectrosc.*, 70, 449 (1978).
- (84) P. Pulay, *TEXAS Manual*.
- (85) H. B. Schlegel, S. Wolfe and F. Bernardi, *J. Chem. Phys.*, 67, 4181 (1977).
- (86) M. Vucelic, Y. Ohrn and J. R. Sabin, *J. Chem Phys.*, 59, 3003 (1973).
- (87) J. Pacansky, U Wahlgren and P. S. Bagus, *Theor. Chim. Acta*, 41, 301 (1976).
- (88) T. K. Ha, C. E. Blom and H. H. Gunthard, *Chem. Phys. Lett.*, 70, 473, (1980).
- (89) J. L. Duncan, *Mol. Phys.*, 28, 1177 (1974).
- (90) W. Meyer and P. Pulay, *Theor. Chim. Acta*, 32, 253 (1974).
- (91) L. Nemes and M. Winnewisser, *Z. Naturforsch.*, 31A, 272 (1976).
- (92) J. L. Duncan, A. M. Ferguson, J. Harper and K. Tonge, *J. Mol. Spectrosc.*, to appear, (1987).

- (93) J. L. Duncan and D. C. McKean, *J. Mol. Spectrosc.*, 107, 301 (1984)
- (94) J. L. Duncan and B. Munro, *J. Mol. Struct.*, to appear, (1987).
- (95) T. Shimanouchi and I. Suzuki, *J. Mol. Spectrosc.*, 6, 277 (1961).
- (96) K. Ramaswamy and V. Ranganathan, *Ind. J. Pure Appl. Phys.*, 6, 651 (1968).
- (97) R. S. Dennen, *J. Mol. Spectrosc.*, 29, 163 (1969).
- (98) K. Ohno, M. Hayashi and H. Murata, *J. Sci. Hiroshima Univ. Ser. A.*, 37, 325 (1973).
- (99) T. A. Ford, M. R. Aroca and E. A. Robinson, *S. Afr. J. Chem.*, 30, 95 (1977).
- (100) R. Escribano, J. M. Orza, S. Montero and C. Domingo, *Mol. Phys.*, 37, 361 (1979).
- (101) J. W. Davis, A. G. Robiette and M. C. L. Gerry, *J. Mol. Spectrosc.*, 85, 399 (1981).
- (102) J. L. Duncan, G. D. Nivellini and F. Tullini, *J. Mol. Spectrosc.*, 118, 145 (1986).
- (103) I. M. Mills, private communication on IR spectrum of  $\text{CHDCl}_2$ .
- (104) W. J. Pietro, M. M. Francl, W. J. Hehre, D. J. DeFrees, J. A. Pople and J. S. Binkley, *J. Am. Chem. Soc.*, 104, 5039 (1982).
- (105) E. Magnusson and H. F. Schaefer III, *J. Chem. Phys.*, 83, 5721 (1985).
- (106) J. L. Duncan, *J. Mol. Struct.*, to appear, (1987).
- (107) C. E. Blom and P. Pulay, *Mol. Phys.*, 39, 1537 (1980).

Appendix A

Assignments to the  $A_1$  fundamental bands of ketene

Assignments to R branch rovibration transitions of  $\nu_1$ .

$K_a$	$0^+$	$1^-$	$1^+$	$2^+$	3	4	5	6	7
J									
0	3071.054								
1	71.71	3071.575	3071.575						
2	72.402	72.229	72.285	3071.81					
3	73.049	72.889	72.955	72.49	3071.772				
4	73.71	73.556	73.632	73.13	72.444	3071.27			
5	74.370	74.221	74.300	73.80	73.107	71.967	3070.638		
6	75.04	74.883	74.968	74.47	73.784	72.617	71.301	3069.670	
7	75.71	75.545	75.643	75.14	74.439	73.284	71.967	70.319	3068.534
8	76.41	76.211	76.325	75.806	75.100	73.955	72.635	70.984	69.200
9	77.08	76.85	76.992	76.472	75.766	74.622	73.30	71.648	69.865
10	77.74	77.519	77.659	77.14	76.433	75.283	73.955	72.285	70.535
11	78.40	78.188	78.340	77.81	77.099	75.946	74.622	72.955	71.197
12	79.06	78.829	79.019	78.47	77.761	76.607	75.283	73.632	71.862
13	79.73	79.491	79.685	79.14	78.426	77.268	75.946	74.300	72.50
14	80.39	80.144	80.360	79.80	79.096	77.929	76.607	74.968	73.164
15	81.05	80.802	81.029	80.46	79.756	78.588	77.268	75.62	
16	81.71	81.447	81.697	81.121	80.416	79.245	77.929	76.27	74.48
17	82.363	82.096	82.363	81.78	81.082	79.903	78.588	76.93	75.14
18	83.029	82.751	83.029	82.44	81.744	80.560	79.245		75.806
19		83.407	83.697	83.10	82.412	81.220	79.903		76.47
20		84.052	84.365	83.76	83.07		80.560		77.12
21	84.970	84.700	85.034	84.41	83.73	82.528	81.220		77.78
22	85.627	85.345	85.699	85.07	84.39	83.20	81.863		78.426
23	86.291	85.991	86.355	85.73	85.034	83.86	82.528		79.096
24	86.941	86.637	87.02	86.38	85.699	84.51	83.166		79.75
25	87.594	87.284	87.66	87.048	86.355	85.145	83.820		80.416
26	88.249	87.928	88.339	87.688	87.01	85.82	84.477		81.04
27	88.898	88.572	88.991	88.339	87.67	86.47	85.12		
28	89.533	89.206	89.642	88.991	88.339	87.117	85.771		
29	90.178	89.857	90.292	89.642	88.991	87.770	86.416		
30		90.492	90.941	90.292	89.642	88.417	87.048		
31				94.941	90.292	89.072	87.72		
32					90.941	89.726	88.339		
33						90.36	88.991		
34							89.642		
35									
36									

Assignments to P branch rovibration transitions of  $\nu_1$ .

$K_a$	$0^+$	$1^-$	$1^+$	$2^+$	3	4	5	6	7
J									
0									
1									
2	3069.03	3068.896	3068.896						
3	68.350		68.183	3067.79					
4	67.68	67.567	67.501	67.09					
5	66.98	66.885	66.821	66.419	3065.717	3064.537			
6		66.214	66.142	65.717	65.038	63.863	3062.563		
7	65.61	65.536	65.448	65.038	64.363	63.21	61.885		3057.115
8	64.950	64.872	64.772	64.363	63.685	62.501	61.212	3059.58	56.435
9		64.189	64.087	63.685	62.98	61.820	60.532	58.88	55.749
10	63.606	63.513	63.399	63.007	62.30	61.144	59.852	58.20	55.059
11	62.926		62.714	62.326	61.62	60.468	59.161	57.52	54.372
12	62.244	62.161	62.024	61.645	60.94	59.775	58.483	56.81	53.71
13	61.561	61.494	61.339	60.963	60.25	59.09	57.809	56.13	53.00
14	60.876	60.795	60.653	60.278	59.57	58.408	57.115	55.476	52.309
15	60.194	60.129	59.963	59.595	58.89	57.731	56.435	54.789	
16	59.510	59.450	59.272	58.910	58.225	57.048	55.749	54.103	50.95
17	58.825	58.770	58.582	58.225	57.540	56.363	55.059	53.416	50.26
18	58.139	58.091	57.890	57.540	56.854	55.679	54.372	52.723	49.58
19	57.452	57.416	57.204	56.854	56.166	54.993	53.686	52.034	48.91
20	56.779	56.738	56.508	56.166	55.476	54.307	52.988		48.216
21		56.042	55.816	55.476	54.789	53.622	52.309		47.528
22		55.368	55.116	54.789	54.103		51.62		46.831
23	54.70	54.684	54.423	54.103	53.416	52.239	50.938		46.154
24	54.01	53.992	53.730	53.416	52.723	51.552	50.243		45.464
25	53.34	53.310	53.040	52.723	52.034	50.858	49.551		44.775
26	52.65	52.622	52.352	52.034	51.341	50.171	48.851		44.072
27	51.96	51.936	51.638	51.341	50.652	49.47	48.155		
28	51.28	51.248	50.96	50.652	49.961	48.782	47.456		
29	50.59	50.560	50.243	49.961	49.268	48.084	46.760		
30		49.870	49.551	49.268	48.577	47.390	46.060		
31		49.175	48.851	48.577	47.882	46.692	45.351		
32		48.485	48.155	47.882	47.193	45.995	44.663		
33				47.193	46.493	45.31	43.976		
34					45.809	44.619	43.272		
35						43.908	42.569		
36							41.872		

Assignments to R branch rovibration transitions of  $\nu_2$ .

$K_a$	$0^+$	$1^-$	$1^+$	$2^\pm$	3	4	5
J							
0							
1		2153.796	2153.82				
2		54.454	54.50	2154.194			
3		55.12	55.15	54.829	2154.39		
4		55.763	55.81	55.493	55.031	2154.454	
5		56.408	56.463	56.138	55.682	55.120	2155.87
6		57.050	57.103	56.786	56.338	55.763	56.527
7		57.71	57.741	57.425	56.980	56.408	
8		58.377	58.377	58.055	57.624	57.050	57.80
9		59.020	59.020	58.689	58.244	57.67	58.425
10		59.648	59.648	59.316	58.898	58.313	59.063
11		60.277	60.277	59.941	59.538	58.952	59.697
12		60.901	60.901	60.565	60.164	59.58	60.29
13		61.48	61.522	61.164	60.780	60.19	60.901
14		62.09	62.11	61.787	61.400	60.81	61.522
15		62.69	62.715	62.405	62.010	61.400	62.153
16		63.302	63.302	63.008	62.621	62.010	62.751
17		63.900	63.900	63.600	63.235	62.621	63.361
18		64.493	64.493	64.196	63.831	63.235	63.962
19		65.076	65.076	64.801	64.431	63.831	64.563
20		65.632	65.65	65.362	65.024	64.431	65.14
21		66.210	66.210	65.942	65.62	65.024	65.729
22		66.787	66.787	66.512	66.210	65.62	66.318
23		67.352	67.352	67.083	66.787		66.893
24		67.925	67.910	67.677	67.352		67.451
25		68.483	68.483	68.249	67.925		68.032
26		69.038	69.038	68.82	68.483		68.597
27		69.608	69.567	69.405	69.038		69.156
28		70.164	70.105	69.946	69.611		69.721
29		70.709	70.664	70.547	70.164		70.268
30		71.247	71.166	71.166	70.709		70.827
31				71.789			71.36
32							71.909
33							72.46
34							72.990
35							
36							

Assignments to P branch rovibration transitions of  $\nu_2$ .

$K_a$	$0^+$	$1^-$	$1^+$	$2^+$	3	4	5
J							
0							
1							
2		2151.172	2151.111				
3		50.46	50.419				
4		49.797	49.733	2149.467			
5		49.109	49.031	48.770	2148.324		
6		48.427	48.324	48.076	47.624	2147.047	2147.810
7		47.743	47.624	47.378	46.918	46.363	47.121
8		47.047	46.90	46.674	46.215	45.66	46.417
9		46.363	46.19	45.950	45.518	44.950	
10		45.682	45.459	45.254	44.813	44.234	45.008
11		45.008	44.735	44.537	44.111	43.52	44.292
12		44.292	44.005	43.821	43.398	42.810	43.380
13		43.580	43.265	43.100	42.683	42.116	42.858
14		42.858	42.521	42.361	41.964	41.395	42.116
15		42.116	41.521	41.623	41.240	40.661	41.395
16		41.395	41.022	40.894	40.512	39.928	40.661
17		40.661	40.265	40.152	39.381	39.188	39.928
18		39.928	39.499	39.408	39.045	38.447	39.188
19		39.188	38.742	38.666	38.309	37.704	38.447
20		38.447	37.97	37.903	37.555	36.956	37.704
21		37.704	37.181	37.181	36.811	36.22	36.956
22		36.956	36.416	36.416	36.053	35.47	36.198
23		36.198	35.631	35.631	35.297	34.722	35.444
24		35.444	34.847	34.847	34.537	33.965	34.670
25		34.670	34.043	34.108	33.769		33.898
26		33.898	33.244	33.334	32.991		33.136
27		33.136	32.456	32.565	32.221		32.355
28		32.355	31.653	31.787	31.438		31.575
29		31.575	30.824	31.023	30.652		30.824
30		30.824	30.017	30.223	29.865		30.017
31		30.017	29.208	29.486	29.068		29.208
32		29.24	28.379	28.744	28.274		28.426
33				28.040			27.619
34							26.833
35							26.034
36							25.223

Assignments to R branch rovibration transitions of  $\nu_3$ .

$K_a$	$0^+$	$1^-$	$1^+$	$2^+$	3	4	5	6	7
J									
0									
1		1388.060	1388.060						
2		88.712	88.75	1389.028					
3		89.374	89.436	89.705	1390.128				
4		90.042	90.128	90.381	90.805				
5		90.708	90.805	91.056	91.483		1390.559		
6		91.372	91.483	91.722	92.15	1392.45	91.245		
7		92.038	92.158	92.405	92.83	93.13	91.927		
8		92.706	92.835	93.086	93.50	93.80	92.611		1400.773
9		93.358	93.516	93.766	94.18	94.48	93.296		01.446
10		94.04	94.196	94.43	94.85	95.15			02.111
11		94.70	94.872	95.104	95.52	95.82			02.773
12		95.360	95.57	95.787	96.206	96.501	95.360		03.444
13		96.025	96.253	96.453	96.876	97.176			04.120
14		96.683	96.938	97.121	97.554	97.853	96.751		04.782
15		97.345	97.618	97.800	98.229	98.531	97.442		05.446
16		98.006	98.301	98.476	98.903	99.203	98.134		06.113
17		98.659	98.985	99.148	99.581	99.883	98.836		06.774
18		99.314	99.669	99.810	1400.249	1400.549	99.528		07.443
19		99.968	1400.353	1400.488	00.929	01.223	1400.249		08.118
20	1400.614	01.033	01.156	01.614	01.614	01.914	00.929		08.783
21	01.285	01.710	01.829	02.278	02.278	02.584	01.614		09.411
22	01.934	02.393	02.496	02.957	02.957	03.278			10.112
23	02.584	03.089	03.161	03.634	03.634	03.95	03.036		10.785
24	03.251	03.759	03.837	04.309	04.309	04.63	03.74		11.434
25	03.917	04.448	04.509	04.989	04.989	05.289	04.448		12.103
26	04.572	05.138		05.663	05.663	05.973	05.16		12.778
27	05.216	05.807		06.332	06.332	06.662	05.867		
28	05.867	06.512		07.004	07.004	07.338	06.563		
29	06.512	07.179		07.683	07.683	08.033	07.27		
30	07.179	07.855		08.359	08.359	08.711	08.00		
31				09.037	09.037	09.37	08.711		
32				09.709	09.709	10.07	09.411		
33							10.112		
34							10.82		
35									
36									

Assignments to P branch rovibration transitions of  $\nu_3$ .

$K_a$	$0^+$	$1^-$	$1^+$	$2^{\pm}$	3	4	5	6	7
J									
0									
1									
2		1385.362	1385.362						
3		84.72	84.66						
4		84.04	83.991	1384.31	1384.735				
5		83.36	83.305	83.64	84.061				
6		82.70	82.629	82.97	83.390		1382.481		
7		82.03	81.949	82.30	82.715		81.805		
8		81.36	81.271	81.605	82.043	1382.343	81.144		1387.993
9		80.699	80.595	80.937	81.370	81.681	80.480		87.326
10		80.029	79.916	80.270	80.699	81.002	79.818		86.645
11		79.353	79.238	79.61	80.029	80.332	79.16		85.974
12		78.679	78.565	78.926	79.353	79.656			85.295
13		78.008	77.872	78.249	78.679	78.986			84.613
14		77.334	77.182	77.574	78.008	78.310	77.183		83.931
15		76.662	76.517	76.900	77.334	77.643			83.250
16		75.987	75.861	76.222	76.662	76.966	75.88		82.568
17		75.315	75.169	75.550	75.987	76.298	75.240		81.888
18		74.643	74.491	74.872	75.315	75.630	74.573		81.220
19		73.968	73.815	74.198	74.643	74.962	73.93		80.543
20		73.293	73.138	73.530	73.968	74.297	73.28		79.864
21		72.624	72.462	72.860	73.293	73.628	72.65		79.180
22		71.92	71.788	72.189	72.624	72.962	71.98		78.510
23		71.26	71.115	71.518	71.961	72.286	71.334		77.838
24		70.57	70.437	70.846	71.277	71.617			77.15
25		69.89	69.764	70.175	70.607	70.950	70.054		76.48
26		69.230	69.102	69.508	69.95	70.291	69.409		75.81
27		68.549	68.419	68.835	69.272	69.615	68.779		
28		67.869	67.739		68.606	68.950	68.145		
29		67.196	67.070		67.933	68.282	67.495		
30		66.517	66.393		67.261	67.618	66.855		
31		65.835	65.720		66.591	66.960	66.220		
32		65.162	65.055		65.916	66.296	65.603		
33					65.249	65.603	64.961		
34						64.961	64.33		
35							63.698		
36							63.044		

Assignments to R branch rovibration transitions of  $\nu_4$ .

$K_a$	$0^+$	$1^-$	$1^+$	$2^+$	3	4	5
J							
0							
1		1117.164	1117.164				
2		17.841	17.841	1120.023			
3		18.504	18.504	20.698	1123.166		
4		19.177	19.177	21.381	23.846		
5		19.859	19.859	22.055	24.522		1130.945
6		20.54	20.568	22.731	25.200		31.61
7		21.206	21.252	23.408	25.877		32.285
8		21.882	21.932	24.091	26.554	1129.546	32.95
9		22.609	22.609	24.771	27.238	30.22	
10		23.290	23.290	25.450	27.922	30.89	34.319
11		23.974	23.974	26.137	28.606	31.59	34.996
12		24.659	24.659	26.820	29.291	32.27	35.674
13		25.338	25.338	27.505	29.976	32.94	36.357
14		26.033	26.033	28.188	30.661	33.62	37.06
15		26.74	26.716	28.862	31.346	34.319	37.73
16		27.442	27.382	29.546	32.031	34.996	38.41
17		28.131	28.064	30.245	32.716	35.674	39.106
18		28.84	28.741	30.945	33.388	36.357	39.79
19		29.546	29.421	31.640	34.091	37.06	40.458
20		30.245	30.112	32.306	34.771	37.756	41.16
21		30.945	30.791	32.989	35.461	38.436	41.84
22		31.640	31.472	33.692	36.162	39.106	42.519
23		32.37	32.149	34.396	36.845	39.812	43.216
24		33.083	32.830	35.09	37.592	40.507	43.887
25		33.794	33.507	35.79	38.214	41.193	44.58
26		34.503	34.183	36.487	38.915	41.873	45.270
27		35.232	34.858	37.171	39.603	42.570	45.970
28		35.935	35.553	37.883	40.303	43.256	46.662
29		36.664	36.240	38.587	41.00	43.969	47.334
30		37.384	36.911	39.280	41.696	44.646	48.022
31				39.971	42.377	45.344	48.221
32					43.066	46.026	49.411
33						46.749	50.106
34							50.803
35							
36							

Assignments to P branch rovibration transitions of  $\nu_4$ .

$K_a$	$0^+$	$1^-$	$1^+$	$2^+$	3	4	5
J							
0							
1							
2		1114.484	1114.484				
3		13.82	13.764	1115.994			
4		13.162	13.096	15.309	1117.779		
5		12.495	12.38	14.631	17.103		
6		11.835	11.69	13.967	16.432		
7		11.175	11.02	13.302	15.756		1122.185
8		10.519	10.38	12.626	15.087		21.509
9		09.870	09.69	11.948	14.427		20.839
10		09.211	09.002	11.270	13.764	1116.757	20.160
11		08.570	08.329	10.608	13.096	16.077	19.490
12		07.929	07.661	09.943	12.421	15.400	18.83
13		07.282	06.97	09.280	11.753	14.748	18.169
14		06.634	06.298	08.619	11.093	14.080	17.509
15		05.978	05.626	07.943	10.433	13.407	16.841
16		05.344	04.945	07.282	09.769	12.739	16.175
17		04.710	04.258	06.634	09.108	12.09	15.509
18		04.067	03.579	05.978	08.448	11.437	14.847
19		03.430	02.945	05.344	07.792	10.772	14.193
20		02.811	02.224	04.653	07.123	10.108	13.54
21		02.172	01.553	04.02	06.461	09.445	12.872
22		01.553	00.88	03.363	05.805	08.784	12.210
23		00.912	00.186	02.704	05.145	08.121	11.550
24		00.290	1099.520	02.049	04.489	07.466	10.889
25		1099.679	98.827	01.389	03.833	06.810	10.228
26		99.054	98.156	00.746	03.178	06.155	09.566
27		98.443	97.475	00.098	02.525	05.520	08.908
28		97.827	96.815	1099.459	01.867	04.854	08.261
29		97.195	96.143	98.827	01.208	04.191	07.600
30		96.59	95.467	98.156	00.554	03.523	06.96
31		95.989	94.780	97.495	1099.904	02.893	06.298
32		95.37	94.117	96.86	99.249	02.224	05.626
33				96.222	98.597	01.553	04.98
34					97.942	00.912	04.33
35						00.290	03.664
36							03.03